Control of semiconductor quantum dots by tailored static and dynamic strain fields

Dissertation

zur Erlangung des akademischen Grades

Dr. rer. nat.

eingereicht an der

Mathematisch-Naturwissenschaftlich-Technischen Fakultät

der Universität Augsburg

von

Xueyong Yuan

March 2019

Erstgutachter: Prof. Dr. Hubert Krenner
Zweitgutachter: Prof. Dr. Manfred Albrecht
Tag der mündlichen Prüfung: 28.05.2019

Abstract

The discovery and application of the laws of quantum mechanics has led in the past century to the "first quantum revolution", characterized by the development of electronic devices and systems of increasing complexity that have profoundly affected our society. There is consensus that we are now approaching the threshold of a second quantum revolution, in which still unexploited resources of quantum mechanics, such as quantum entanglement, will be used to build up quantum computers and secure quantum communication systems. Photons, the quanta of light, shall play a major role in this context, as they are the only realistic quantum information carriers for connecting separate quantum systems and for transmitting quantum information. In addition, degrees of freedom of photons can be used for quantum simulation and computation tasks.

Among different systems, semiconductor quantum dots (also dubbed "artificial atoms") have emerged as one of the most promising quantum-light sources because of their capability of emitting single and entangled photons "on demand" and at high rates. Several issues with these sources have been solved, while other challenges are still open. Arguably, the major one is that the electronic structure and optical spectra of different quantum dots are affected by fluctuations stemming from stochastic processes occurring during quantum dot growth. This limited control leads to a spread in emission wavelength (hindering the use of multiple quantum dots in quantum networks and quantum photonic circuits), the poor coupling to optical modes in predefined photonic circuits, the poor performance as sources of entangled photons, and to inefficiencies due to noise sources in the solid-state environment of a quantum dot.

In this thesis, we focus on the use of strain fields induced in the quantum dot after fabrication, as a tool to control specific quantum dot properties, and, conversely, we use the high strain-sensitivity of the quantum dot optical properties to detect local strain fields in mechanical resonators.

Firstly, we develop novel micro-machined piezoelectric actuators featuring geometrical strain amplification to continuously tune the emission wavelength of single quantum dots in an unprecedented tuning range of about ~100 meV, corresponding to ~50.000 times the natural emission linewidth, and to reshape the optical selection rules in the studied quantum dots. Together with calculation results, our findings show a promising route to obtain quantum-light sources with ideally oriented dipoles and enhanced oscillator strength for integrated quantum photonics.

Then we use the developed actuators to drive mechanical oscillations in suspended membranes. Mechanical resonances are detected by monitoring the light emission from the embedded quantum dots and their frequency tuned by applying continuously variable tensile stress through the same platform. Lastly, the propagation of sound waves in the suspended beams is studied. With quantum dots acting as optical strain sensors, the propagation and attenuation properties of Lamb waves are studied.

Contents

1. Introduction

Since the end of last century, quantum technologies attract more and more interest all over the world. Motivated by the potential prospects of advanced quantum technologies (such as quantum communication[1]), significant progress has been achieved. Based on the present state-of-the-art, we can be quite optimistic to say that we are at the threshold of a second quantum revolution[2], which will be characterized by the full exploitation of the resources provided by quantum mechanics. However, there are still considerate long-standing issues in front of us, one of the main ones being the implementation of suitable physical systems. Up to now, several kinds of physical systems (such as nuclear spins, electrons, superconducting qubits, photons *etc.*) have been explored.

Photons, the basic particles of light, are considered to be promising candidates in quantum photonics. To maximumly realize the potential of quantum photonics, efficient photon counters, quantum circuits and ideal single photon sources are necessary[3]. Among them, an ideal single photon source is in urgent need.

What is a single-photon source? As the name implies, the single-photon source should emit one and only one photon at a time. Moreover, for an ideal single-photon source, photons should be indistinguishable in all degrees of freedom and it should be possible to have emission at high-repetition rates (>GHz). There are already several established systems, which can be used as single photon emitters[4]. The easiest approach is to attenuate a pulsed laser[5], however the production of single photons is probabilistic with this method, since the number of photons in a given time bin follows the Poissonian statistics. A single quantum object behaving as a two-level system would be an ideal single photon source.

There are many possible candidates for two-level quantum system, like atoms[6], molecules[7], vacancy centers,[8] semiconductor quantum dots (QDs), *etc*. Based on recent progress, QDs are arguably the most attractive systems for emitting single and entangled photons for the compatibility with mature semiconductor technology, high brightness and near unity entanglement fidelity [9–13].

QDs are nanometer-sized semiconductor structures usually surrounded by another semiconductor material having a larger energy band gap. Due to the three-dimensional (3D) confinement of the charge carriers, QDs show discrete electronic states. Consequently, when a QD is excited, an electron and a hole recombine and emit a photon with well-defined energy. This is why sometimes QDs are called "artificial atoms". There are several methods to prepare QDs. Colloidal QDs are obtained via chemical synthesis from solution. This approach allows the fabrication of large amounts of QDs at relatively low cost. The resulting QDs are already commercially available and used, e.g., in high-contrast displays. The proximity of the confined charge carriers to the free surfaces of the nanostructures render however colloidal QDs not ideal for envisioned applications in quantum technologies. Self-assembled quantum QDs

prepared by epitaxial growth methods (with molecular beam epitaxy (MBE) or metalorganic vapor phase epitaxy (MOVPE)) are in this respect preferable, as the nanostructures can be placed far (typically >100 nm) from surfaces and associated defects. This kind of QDs, which are the focus of this thesis, generally have high material and optical quality and can be easily integrated into optoelectronic devices by making use of established processes in the semiconductor industry. However, epitaxial growth comes with additional complexity and high costs.

The study of semiconductor QDs can be traced back to the 1980s, partly motivated by the perspective of realizing lasers with ultralow threshold. The discovery that both colloidal QDs and epitaxial QDs can generate photons with sub-poissonian statisics[14] (a prerequisite for single-photon emission) opened the way to the exploration of these systems for quantum optical studies and applications. The steady progress in QD growth, fundamental understanding, device integration, and excitation schemes has brought QDs to the level of being considered as near optimal single photon sources.[12].

Although the epitaxial growth of semiconductor QDs has made substantial progress, as-grown semiconductor QDs are still not ready for most envisioned applications. As an example, we consider the Hong-Ou-Mandel (HOM) two-photon interference (TPI)[15], which is the core of Bell-state measurements (BSM) and the basis of photonic-based quantum information processing. The experimental configurations of a HOM measurement is shown in Fig 1.1, where two photons are impinging on a 50/50 beamsplitter[16]. When the involved photons are indistinguishable (same wavelength, same wavepacket, same polarization), TPI results in the two photons exiting the same port of the beam-splitter and thus provides an effective interaction between the two photons. Up to now the TPI has been successfully realized with various quantum emitters, like single trapped atoms[17], ions[18], molecules[19] and also QDs[20,21]. The large time gap between the first demonstration of single photon emission (2000)[14] and HOM interference among photons emitted by independent QDs (2010)[20,21] and still modest performance (interference visibilities barely reaching 50%[22]) is related to two issues of QDs. First, photon emission from an ensemble of QDs is inhomogeneously broadened because of the fluctuations of QD structure and hence emission wavelength and photon wavepacket. Second, interaction between confined charge carriers and QD environment (charges, lattice vibrations, nuclear spins) further reduce the indistinguishability of photons. Tackling these issues is still a formidable challenge.
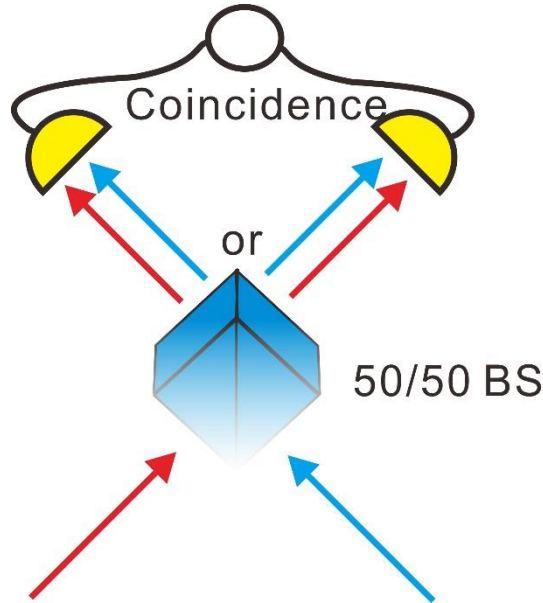
Figure 1.1: Sketch of a commonly used Hong-Ou-Mandel measurement for two photon interference. Two indistinguishable photons entering a 50/50 beam-splitter (BS) "coalesce" and exit the same port of the BS. Therefore there are no coincidence counts between events registered by detectors placed at the two exit ports.

If we think further to make use of the biexciton-exciton decay cascade of QDs to act as a source of polarization-entangled photon pairs[23–25], additional requirements need to be fulfilled by the QDs. In particular, the absence of in-plane structural symmetry in QDs will generate a coherent coupling of the two bright excitons, which lead an energy difference between emitted photons, the so-called fine structure splitting (FSS). If the FSS is larger than the radiative linewidth of the transitions (of the order of 1-3 µeV), the degree of entanglement of the emitted photon pairs is strongly decreased[23,26]. To obtain entangled photons without discarding most of the photons, it is desirable to get most QDs to have negligible FSS. Although creating an ensemble of QDs with sufficiently small FSS though novel growth methods made great progress in recent years[27–29], it is still very difficult to find QDs with zero FSS from the as-grown sample. From theoretical estimates[30], a very low portion of QDs from an as-grown sample is free of asymmetries (1 over 1000 for Stranski-Krastanow (SK) QDs). Furthermore, the possibility to find two identical as-grown QDs to perform the quantum entanglement swapping (the entanglement between two particles initially belonging to two independent entangled pairs)[31] would be even much lower ($<10^{-9}$).

Many post-growth tuning methods have been elaborated, such as thermal annealing[32–34], magnetic field[25,35], lateral[36,37] and vertical[38–40] electric fields as well as strain fields[41]. The latter, especially when provided by piezoelectric actuators, have proven particularly flexible. In 2006, a pioneering work by S. Seidl[42] *et al.* presented for the first time piezoelectric-based strain tuning of QDs using a lead zirconic titanate (PZT) ceramic stack bonded to the semiconductor structure. Although the limited strain provided by the PZT ceramic did not provide too exciting results, it opened a new door to use strain fields to manipulate QDs. Thereafter, the strain tuning of QDs with

piezoelectric actuators has seen rapid developments: $Pb(Mg_{1/3}Nb_{2/3})O_3$-$PbTiO_3$ (PMN-PT) piezoelectric actuators replaced PZT because of their larger piezoelectric coefficients. For efficient wavelength tuning via biaxial strain, (001)-cut PMP-PT were used [41,43]. Anisotropic strain fields were proposed to be a more effective way to modify the FSS[44], which could be eliminated via the combination of two independent uniaxial stresses[45]. This prediction was experimentally confirmed later[46,47]. The theoretical design and experimental realization of wavelength tunable entangled photon sources[48–51] finally removed a major obstacle towards the use of QDs as scalable solid-state sources of entangled photons.

There is no doubt that various milestone-level works have been done on the strain tuning of QDs, but most of the work focused on the recovery of the symmetry of QDs and/or on wavelength tuning. In both cases, strain provided by piezoelectric actuators was used as a perturbation and in a quasi-static fashion to fine-tune the emission properties of QDs. In this thesis we move beyond this perturbative and static regime and explore further possibilities offered by the interaction of QDs with externally driven strain fields.
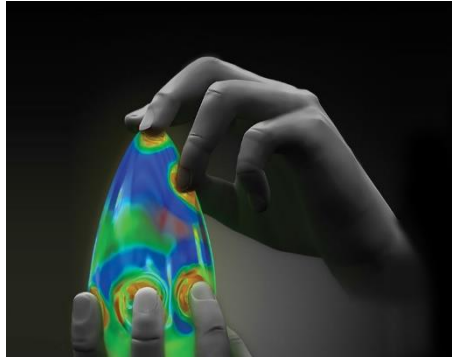
Figure 1.2: Prospect picture on the use of strain fields to reshape material properties at will. Adapted from Ref[52].

1.1 Thesis outline

The aim of the work presented here is to study and make use of the interaction between elastic fields and QDs in view of potential applications in quantum technologies. Following this introduction, the thesis is organized as follows:

Chapter 2: This chapter gives a general introduction on the theoretical background of the thesis, beginning with the epitaxial growth of quantum confined semiconductor QDs, strain effects on the band structure of semiconductors. Then a detailed description of surface acoustic waves is presented.

Chapter 3: This chapter presents the main tuning methods on QDs in this thesis: strain fields arising from a piezoelectric actuator and surface acoustic waves, and the related experimental methods are also described. Then an overview of the experimental setup is presented, followed by the introduction of the simulation via COMSOL Multiphysics.

Chapter 4: In this chapter, we show that the natural quantization axis of a GaAs quantum dot can be turned to lie in the growth plane via uniaxial elastic stress. This 90°

rotation, which is accomplished through a complex evolution of the confined hole wave function, is possible whenever confinement can be viewed as a perturbation compared to the strain-induced effects. The experimental and computational results suggest that uniaxial stress – which is already employed for enhancing the performance of integrated electronic circuits – may be the right strategy to obtain quantum-light sources with ideally oriented transition dipoles and enhanced oscillator strengths for integrated quantum photonic circuits.

Chapter 5: In this chapter, a novel hybrid system is developed: QDs are coupled to the vibrations of the nanomembrane in which they are embedded. Using the actuator presented in Chapter 4, we are able to continuously tune the resonance frequency of the membrane resonators. This hybrid system shows promising prospects on ultrafast mechanical motion coupling.

Chapter 6: In this chapter, we investigate sound propagation properties in suspended beams containing GaAs QDs. Based on simulations and phase-locked sweep measurements, the existence of antisymmetric Lamb waves in the suspended beams is proven. Our findings may lay the foundation for the future realization of hybrid in-chip optomechanical systems.

Chapter 7: In the last chapter, we make a summary and conclusion of this thesis. More importantly, some new issues arise based on the progress we made, which give an outlook to perform further studies to explore the potential of QDs for future quantum systems.

2. Theoretical background

In this chapter, we will give a general introduction to the electronic and optical properties of semiconductor QDs and their growth by epitaxial methods. We will then discuss the effects produced by strain; for simplicity we will limit ourselves to discuss the problem in the case of bulk semiconductors. Finally we discuss the generation of strain fields by surface acoustic waves.

2.1 Introduction to semiconductor QDs

2.1.1 Quantum Confinement

According to quantum mechanics, quantum confinement effects become apparent in semiconductors as soon as at least one of the spatial dimensions is reduced below a certain value (of the order of ~10 nm for typical semiconductors). For the specific case of optically active structures capable of confining the motion of both electrons and holes in the same material, quantum confinement manifests itself with a blue-shift of the emission wavelength as the size is reduced. Since we will be dealing with semiconductors at cryogenic temperatures, light stems mostly from recombination of electron and hole complexes (excitons) held together by the Coulomb interaction. In this case, the size required to achieve quantum confinement can be argued from the free exciton Bohr radius a_B, related to the Bohr radius of the hydrogen atom a_o by [53]:

$$a_B = \varepsilon \frac{m}{m^*} a_o,$$
(2.1)

where ε is the dielectric constant of the material, m^* is the electron-hole reduced effective mass, and m the rest mass of the electron.

Based on the number of confinement dimensions, the confined structure can be classified as quantum well (confinement only in one dimension and free motion in the remaining two dimensions), quantum wire (confinement in two dimensions and free motion in one dimension) or a quantum dot (three-dimensional confinement), as shown in Fig 2.1. Compared to a bulk semiconductor, due to the quantum confinement of charge carriers in these low-dimensional heterostructures, the density of states (DOS) changes significantly. In bulk semiconductor materials (without quantum confinement) and assuming simple parabolic bands, the DOS is continuous and increases with $(E-E_g)^{1/2}$, with E_g the energy band gap. For quantum wells, the DOS takes the form of a staircase, with each step corresponding to the energy of a confined state. For quantum wires, the DOS diverges at the positions of each confined state. Finally, for QDs the DOS is ideally composed of delta functions and takes the form:

$$\rho(E) = \sum_v \delta(E - E_v),$$
(2.2)

with E_ν being the energy of a confined state.

The occurrence of discrete states can be illustrated via a simple effective mass approximation model[54]. In this model, one solves a Schrödinger equation for a particle with effective mass m^* confined in a potential provided by the semiconductor QD region surrounded by barriers. Assuming that the QD has the shape of a box surrounded by infinitely high barriers, the particle energy is given by:

$$E_{n1,n2,n3} = \frac{\hbar^2 \pi^2}{2m^*} \left(\frac{n_1^2}{l_x^2} + \frac{n_2^2}{l_y^2} + \frac{n_3^2}{l_z^2} \right). \tag{2.3}$$

Here the n_1, n_2, n_3 are integers, lx, ly, lz are the box dimensions in the x-, y-, and z-directions. The above reasoning can be applied to both electrons confined in the conduction band of the semiconductor and to holes confined in the valence band. Optical transitions between the resulting discrete states will lead to atomic-like spectra, this is also why sometimes QDs are called "artificial atoms".
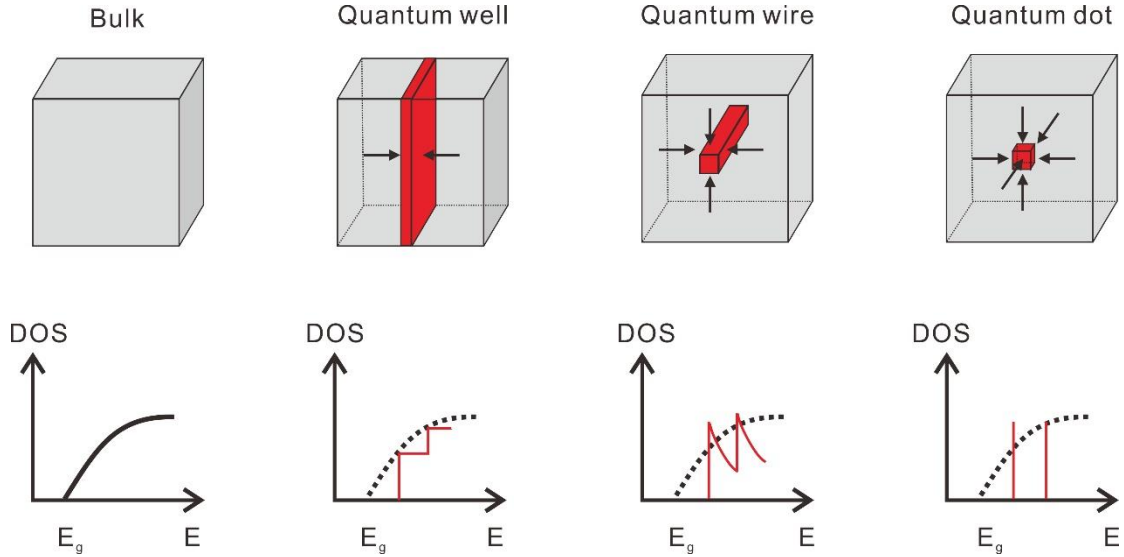
Figure 2.1: Schematic picture of confinement potential and related density of states (DOS) of carriers in semiconductors with different dimensionalities.

2.1.2 Properties of excitons confined in QDs

As discussed earlier, the three-dimensional confinement of carriers in QDs leads to localized states in both conduction band (CB) and valence band (VB). The CB and VB edges along a spatial direction for QD material and surrounding barrier are schematically shown in Fig.2.2. The lowest lying confined electron states are labelled as s- and p- in analogy to the notation used in atomic physics. Various parameters (size, shape and composition)[55] play important roles to the energetic level structure of QDs, which means that one can adjust to some extent the energy level structure through growth.

To investigate the optical properties of QDs, the simplest method relies on optical excitation. There are three main excitation schemes: non-resonant excitation, quasi-

resonant excitation and resonant excitation. In the case of non-resonant excitation (as shown in Fig. 2.2), QDs are excited with a light source (typically a laser) with photon energy higher than the barrier band gap. This leads to electron-hole pairs mainly generated in the barrier. Excited electrons and holes then relax to the respective ground states in the CB and VB, respectively. Actually the number of captured carriers in QDs during the non-resonant excitation is affected by fluctuations. This makes it almost impossible to achieve a quantum efficiency close to unity for a certain transition. In addition, carrier relaxation induces an undesired time jitter in the emission process. Another main drawback of the non-resonant excitation is the inevitable generation of additional charge carriers, which could be captured by traps or defects in the vicinity of QDs. These charges interact with the confined excitons, lead to emission fluctuations, which degrade the indistinguishability of photons emitted by the same QD.

A potentially cleaner excitation method is the so-called "p-shell excitation" (often referred to as quasi-resonant excitation). In this case, the excitation laser is tuned to the energy separation between excited states in the QD. This leads, at least in principle, to improved quantum efficiency by suppressing random carrier capture events. Besides that, no carriers are generated in the barriers, thus reducing undesired interactions. However, time-jitter due to relaxation remains.

Lastly, the most desirable scheme is the resonant excitation, which consists in exciting the QDs directly at the s-shell. This method combines the suppressed generation of carriers in the QD surrounding with the elimination of relaxation processes before the photon emission. The resonant emission of coherently driven QDs can be traced back to 2007[56,57], Rabi oscillations and Mollow triplets were observed, respectively. Remarkably, through resonant excitation of QDs embedded in pillar microcavities, QDs have shown nearly-optimal properties (extremely bright, near-unity indistinguishability and high single-photon purity)[12,58]. In recent years, a two-photon excitation (TPE) scheme has also been employed to resonantly create "biexcitons" in QDs[59], which are particularly relevant for the generation of entangled photon pairs[60] (see below).
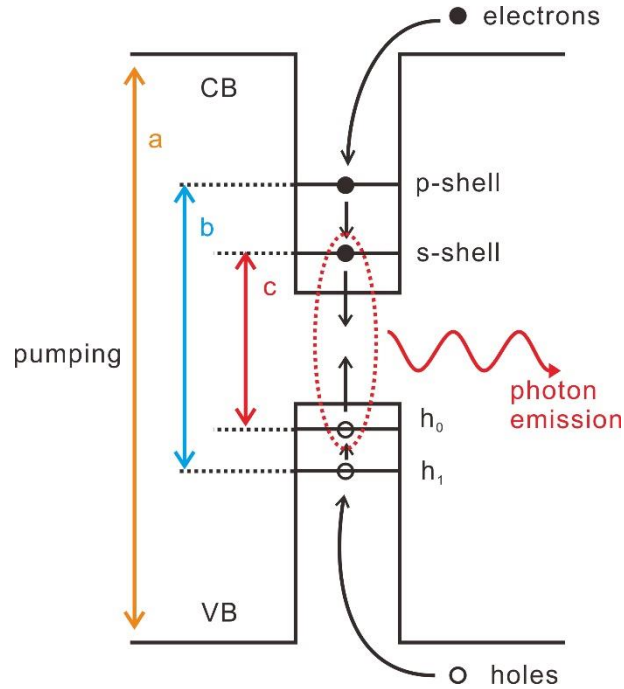
Fig 2.2: Schematic energy landscape of QDs. The CB and VB edges are displayed along a line passing through a QD. Three main excitation schemes are indicated as (a) Non-resonant, (b) p-shell (quasi-resonant), and (c) resonant excitation.

Let us shift our attention back to the lowest energy level (s-shell) in conduction and valence band. Based on the Pauli exclusion principle, there are at most 2 electrons (holes) occupying the conduction (valence) band with different spin configurations. Due to the optical selections, if an electron and a hole have the same spin orientation, the resulting exciton is optically inactive and called dark exciton. Optically we can just observe the biexciton (XX), formed by two electrons and two holes, charged excitons (positive exciton X^+ (one electron and two holes) and negative exciton X^- (two electrons and one hole)), neutral exciton (X (one electron and one hole)). In Fig. 2.3 (a) we display the three typical states in the s-shell level.

If we consider the biexciton state, a direct transition from the biexciton state to the crystal ground state (all valence band states occupied by electrons, i.e. no electrons in CB and no holes in VB)[I] is not possible because of angular momentum conservation: the biexciton and the crystal ground state have both zero total angular momentum, while a photon carries a spin of 1. The XX recombination follows instead a cascade process. First a photon is emitted from the biexciton state leaving the quantum dot in a bright neutral exciton state. Then the remaining exciton recombines and emits another single photon. The process is called biexciton-exciton cascade[61], which is a quite well-known scheme to generate entangled photon pairs from QDs[23]. In QDs, an electron can only recombine with a hole with different spin configuration and emit left (σ^+) or right (σ^-) circularly polarized photons[II]. That means, starting from the biexciton state, an electron recombines with a hole emitting a σ^+ or σ^- photon, then the second electron with the opposite spin recombines with the remaining hole emitting another photon, which is oppositely polarized with respect to the previous one. Before measuring the polarization state, the XX-X photon pairs remain maximally entangled and the polarization entangled state can be written as:

$$|\psi\rangle = \frac{1}{\sqrt{2}}(|\sigma^-\rangle_{XX}|\sigma^+\rangle_X + |\sigma^+\rangle_{XX}|\sigma^-\rangle_X) = \frac{1}{\sqrt{2}}(|H\rangle_{XX}|H\rangle_X + |V\rangle_{XX}|V\rangle_X) \quad (2.4)$$

This state has the same form in any basis, here we use the H (horizontal) and V (vertical) linear polarization directions to rewrite it in a rectilinear basis.
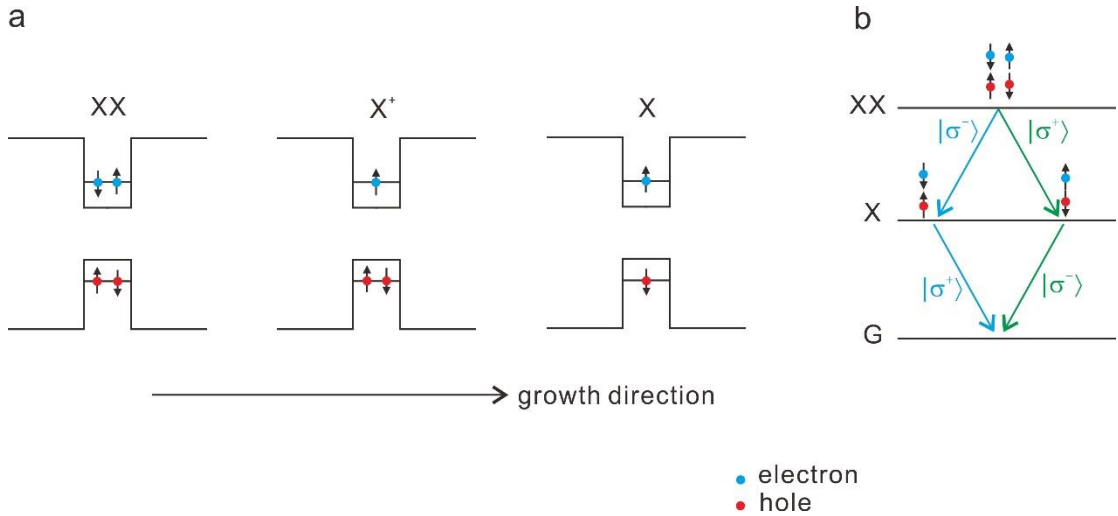
Fig 2.3: (a) Schematic picture of the typical s-shell carrier configurations in QDs. Here only optically active biexciton (XX), positively charged exciton (X^+) and neutral exciton (X) are shown. (b) Sketch of biexciton-exciton cascade decay in an ideal QD.

Although the theoretical proposal based on the above considerations was presented by Benson *et al*. in 2000[23], the first experimental proof with QDs was reported only in 2006[24]. The biggest obstacle hindering the QDs to act as polarization-entangled photon sources comes from the so-called exciton fine structure splitting (FSS), i.e. a broken

---

[I] Here non-radiative processes, such as the Auger process, are neglected.

[II] In QDs made of common direct bandgap semiconductors such as GaAs, due to the confinement, electrons with total angular momentum projection $J_z = \pm 1/2$ recombine only with heavy holes with $J_z = \pm 3/2$, where z is the direction of the natural quantization axis, coinciding with the growth direction.

degeneracy of the X level. The FSS stems from the exchange interaction and is closely related to the spatial symmetry of QDs: only QDs with an in-plane symmetry of D_{2d} or higher will show zero FSS. There are many factors that cause deviations from this ideal situation in real QDs[62–64], so that it is a big challenge to obtain QDs with zero FSS from the as-grown samples. Therefore, a more realistic representation of the biexciton-exciton cascade is shown in Fig. 2.4 (a). The energy difference among the possible transitions will seriously deteriorate the entanglement, since it makes the two possible decay paths of XX (and X) distinguishable[24].

From the experimental point of view, the FSS can be easily observed via polarization-resolved measurements of the PL spectra. Fig 2.4 (b) is a typical polarization-resolved PL spectrum of exciton emission from a GaAs QD. The wavelike pattern followed by the energy as a function of polarization angle indicates the existence of FSS. To obtain entangled photon pairs from QDs, a vanishing FSS would be desirable (more precisely, the FSS should be below the values of the order of the radiative linewidth (several µeV))[65].
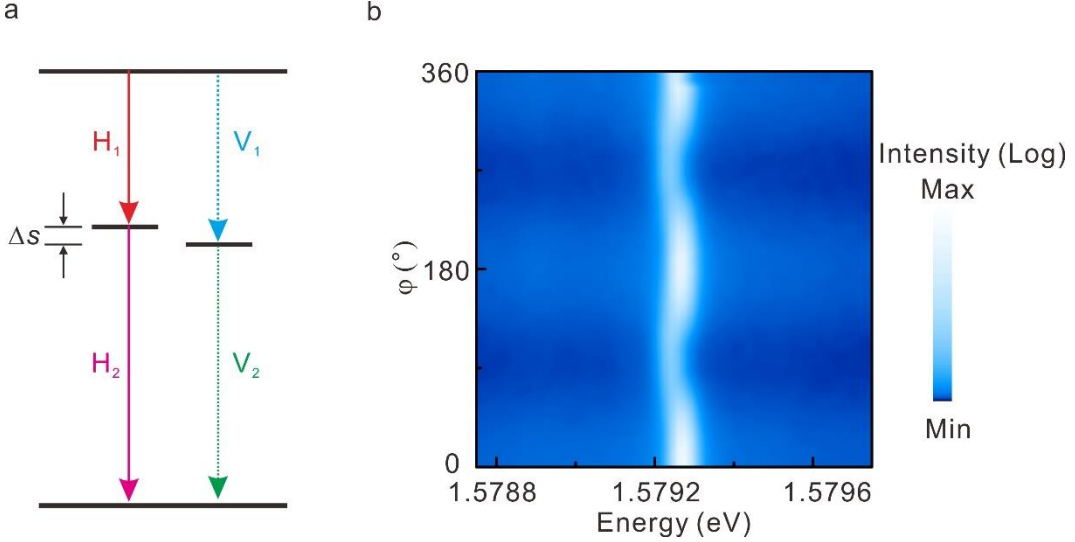
Fig. 2.4: (a) Illustration of the biexciton cascade in presence of FSS. H_i (V_i) with i = 1, 2 stand for the horizontally (vertically) polarized photons with respect to a specific axis. Because of the exchange interaction in QDs with in-plane anisotropy, the nominally degenerate X levels mix and the two new eigenstates are split by the FSS (with magnitude given by Δs). (b) Typical polarization-resolved PL spectra of the neutral exciton emission in a QD studied in this thesis. Because of the limited spectral resolution, a wavy pattern is observed, which stems from two linearly polarized emission lines.

As mentioned above, the FSS arises from the exchange interaction, which couples the electron and hole spins. Let's start from the Hamiltonian for the electron-hole exchange interaction, which can be written as[66]:

$$H_{\text{exchange}} = -\sum_{i=x,y,z}(a_i J_{h,i} S_{e,i} + b_i J_{h,i}^3 S_{e,i}) \tag{2.5}$$

Here the a_i, b_i are spin-spin coupling constants, which depend on the QD geometry. The z-direction is defined as along the growth direction, which is also the natural quantization axis for QDs because of their typical flat morphology. $J_{h,i}$, $S_{e,i}$ are the spin operators for hole and electron, respectively. As mentioned before, due to confinement

and strain, here we just consider the heavy hole and safely neglect the light hole band. Hence $J_h = 3/2$, $J_{h,z} = \pm 3/2$ and $S_e = 1/2$, $S_{e,z} = \pm 1/2$. Using the projection of total angular momentum on z-axis $M = J_{h,z} + S_{e,z}$, there are four exciton states formed:

$$
\begin{aligned}
|+1\rangle &= |+\tfrac{3}{2}; -\tfrac{1}{2}\rangle \\
|-1\rangle &= |-\tfrac{3}{2}; +\tfrac{1}{2}\rangle \\
|+2\rangle &= |+\tfrac{3}{2}; +\tfrac{1}{2}\rangle \\
|-2\rangle &= |-\tfrac{3}{2}; -\tfrac{1}{2}\rangle
\end{aligned}
\tag{2.6}
$$

Here states with $|M| = 2$ do not couple to the light field and they are therefore optically inactive (dark excitons, DX), while states with $|M| = 1$ are optically active (bright excitons, BX). Using these four exciton states as a basis, a matrix representation of the Hamiltonian in equation (2.5) can be constructed as[66]:

$$
H_{exchange} = \frac{1}{2}\begin{pmatrix}
+\delta_0 & +\delta_1 & 0 & 0 \\
+\delta_1 & +\delta_0 & 0 & 0 \\
0 & 0 & -\delta_0 & +\delta_2 \\
0 & 0 & +\delta_2 & -\delta_0
\end{pmatrix}
\tag{2.7}
$$

with $\delta_0 = 1.5(a_z + 2.25b_z)$, $\delta_1 = 0.75(b_x - b_y)$, $\delta_2 = 0.75(b_x + b_y)$. The matrix in 2.7 has a block form, therefore the bright exciton and dark exciton do not mix with each other and their energies differ by δ_0. While the bright states mix with each and split by an energy δ_1 (the FSS), dark states mix with each other and separate by an energy δ_2. Besides, the coefficient a_i is larger than b_i, which means the separation between bright states and dark states (δ_0) is the largest. For an ideal in-plane symmetric QD, the FSS vanishes ($\delta_1 = 0$) and $|+1\rangle, |-1\rangle$ are the degenerate states of $H_{exchange}$. However, in a more realistic case (QDs are asymmetric, $b_x \neq b_y$), the bright states will hybridize: the two eigenstates are the linear combination of $|\pm 1\rangle$ states, split by δ_1. However, the dark excitons always mix (split in δ_2), no matter whether the QD is in-plane symmetric or not. Based on the discussion above, the energy diagram of the refined fine structure of neutral exciton with electron-hole interaction is shown in Fig. 2.5, here a lower symmetry (anisotropic $E_{exchange}$) is also included.
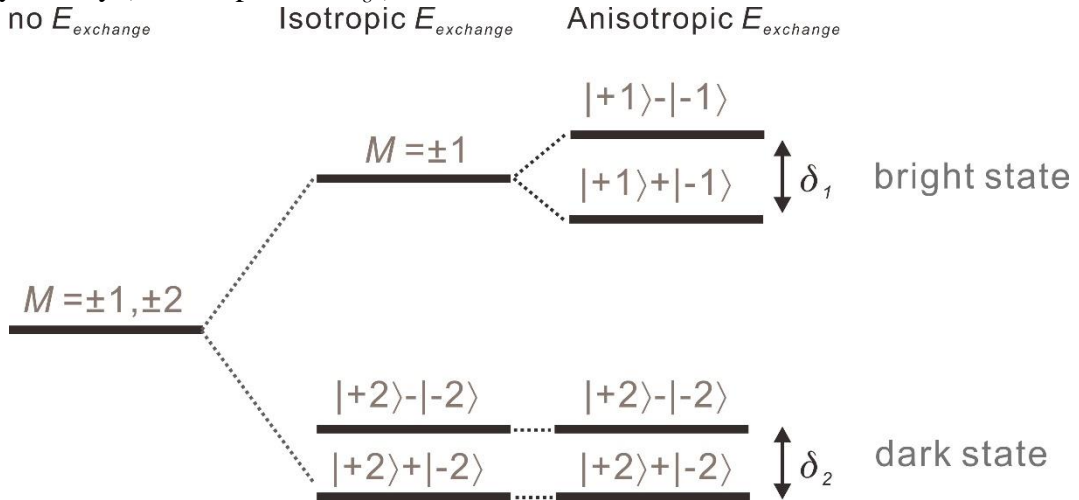

Fig. 2.5: Schematic energy diagram representing the fine structure of the neutral exciton stemming from electron-hole interaction.

There are mainly two approaches to erase the FSS, the first one is trying to grow highly symmetric QDs. Since QDs are nanostructures consisting of thousands of atoms, unavoidable fluctuations in atoms arrangement and intermixing between the dot and barrier material are serious obstacles to grow QDs with ideal symmetry. Although some progress was obtained during the past to grow QDs with intrinsically low FSS[27–29], it is a still a great challenge from the growth side. Another method is the introduction of external fields, i.e. post-growth tuning methods. As mentioned earlier, several methods are employed to tune the FSS of QDs. Due to the research topic and length constraints, we will concentrate on the strain tuning of QDs in the following sections.

2.1.3 Epitaxial growth of Ⅲ-Ⅴ QDs

Various methods are employed to generate high-quality semiconductor QDs, here we just present a general introduction on the Ⅲ-Ⅴ QDs used in our work: 1) self-assembled In(Ga)As QDs, which are the most common and well-studied QDs. 2) GaAs QDs via droplet etching, which have emerged recently as a superior source of entangled photon pairs.

The most studied self-assembled In(Ga)As QDs are grown via the Stranski-Krastanow (SK) method. In Fig. 2.6 we present the whole process of the growth of In(Ga)As QDs. Generally speaking, a lattice mismatch between grown material and substrate is a necessary element for SK growth. There is a 7% lattice parameter mismatch between InAs and GaAs ($a_{InAs} = 0.605$ nm, $a_{GaAs} = 0.56$ nm), a biaxial strain $\varepsilon = \frac{a_{InAs} - a_{GaAs}}{a_{GaAs}}$ will be induced when a thin InAs layer is deposited onto the GaAs substrate (as shown in Fig. 2.6 (b), this layer is called the wetting layer). However, the associated strain energy increases rapidly as the wetting layer thickens. In order to relieve the strain, island formation can occur in either dislocated or coherent fashion. The thickness of wetting layer at which island nucleation initiates is called critical thickness h_c. This critical thickness is closely related to the lattice mismatch between the deposited material and substrate, and can also depend on the deposition temperature (the h_c for InAs QDs/GaAs is about 1.7~1.8 monolayer). Although In(Ga)As QDs are the most studied QDs and significant achievements have been accomplished with them, there are still open challenges. First of all, as strain-driven In(Ga)As QDs are naturally formed, they have random spatial positions. In other words, the growth of this kind of QDs sample with suitable density for single-QD applications is quite tricky. Secondly, considering the intermixing between InAs and GaAs, strain effects and piezoelectricity, there is very complex physics behind this system.
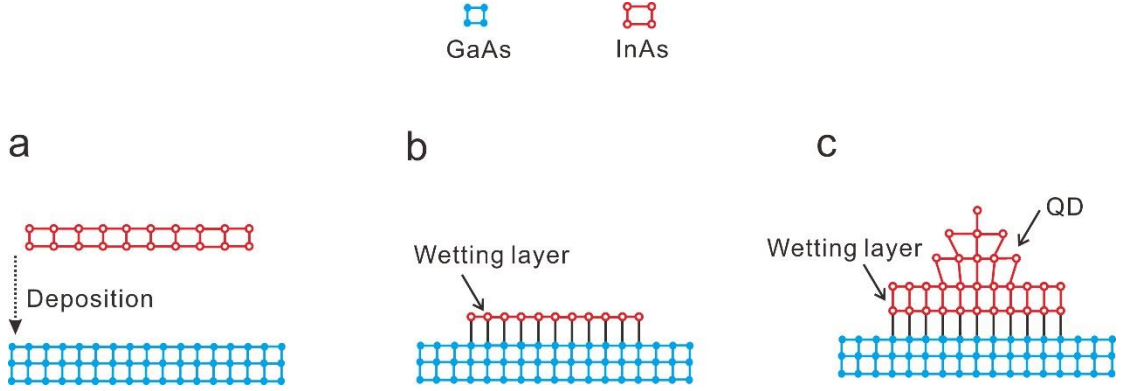
Fig. 2.6: Schematic illustration of the growth of self-assembled In(Ga)As QDs via the SK method. (a)-(c) show the whole process of the forming of QDs.

In recent years, GaAs QDs obtained by in-situ droplet etching have emerged as one of the most promising single and entangled photon sources. In 2007, gallium droplets were found to act as "electrochemical drills", etching the GaAs to obtain nanoholes[67]. After a short period, this droplet etching method was employed to grow QDs[68]. With this method, the density and emission wavelength of the resulting QDs can be well controlled via the manipulation of proper parameters, however, the FSS of QDs obtained by gallium etching is still quite large. Huo *et. al*[29] and Graf *et. al*[69] switched to using aluminum droplets as the "drills" to obtain nanoholes and, with parameters optimization, highly symmetric GaAs QDs were obtained, which showed the capability of generating highly entangled photons even without [70,71].

Fig. 2.7 (a) illustrates the process to grow the GaAs QDs used in this thesis. Firstly, a layer of $Al_xGa_{1-x}As$ layer is deposited on a GaAs substrate by molecular beam epitaxy (MBE). Then the As flux is interrupted followed by the deposition of Al, which gives rise to the formation of nanometer-sized droplets. During a subsequent annealing step in As atmosphere, droplets dig nanoholes in the underlying substrate. To infill the nanoholes, GaAs is deposited, followed by annealing. The GaAs QDs form in the nanoholes due to the diffusion of GaAs driven by capillarity effects. Lastly, another $Al_xGa_{1-x}As$ layer is deposited on top acting as the top barrier. Because of the negligible intermixing effect between GaAs and $Al_xGa_{1-x}As$, we can safely use the nanohole shape and size to deduce the structural properties of the derived GaAs QDs. This is also an advantage of the droplet etching method compared to the SK method: various parameters can be adjusted to effectively optimize the geometry of the nanoholes (QDs). Fig. 2.7 (b) shows an atomic force microscope (AFM) image of a nanohole with optimized parameters (sample grown by Saimon Filipe Covre da Silva at the institute of semiconductor and solid state physics, JKU, Linz). The in-plane circular symmetry is clearly seen, which is also confirmed by the polarization-resolved spectra of a neutral exciton in Fig. 2.7 (c). The FSS of the neutral exciton shown in Fig. 2.7 (c) is well below the resolution of the used spectrometer, a FSS value of 0.70 ± 0.18 μeV is obtained via fitting procedures explained in Sec 3.3
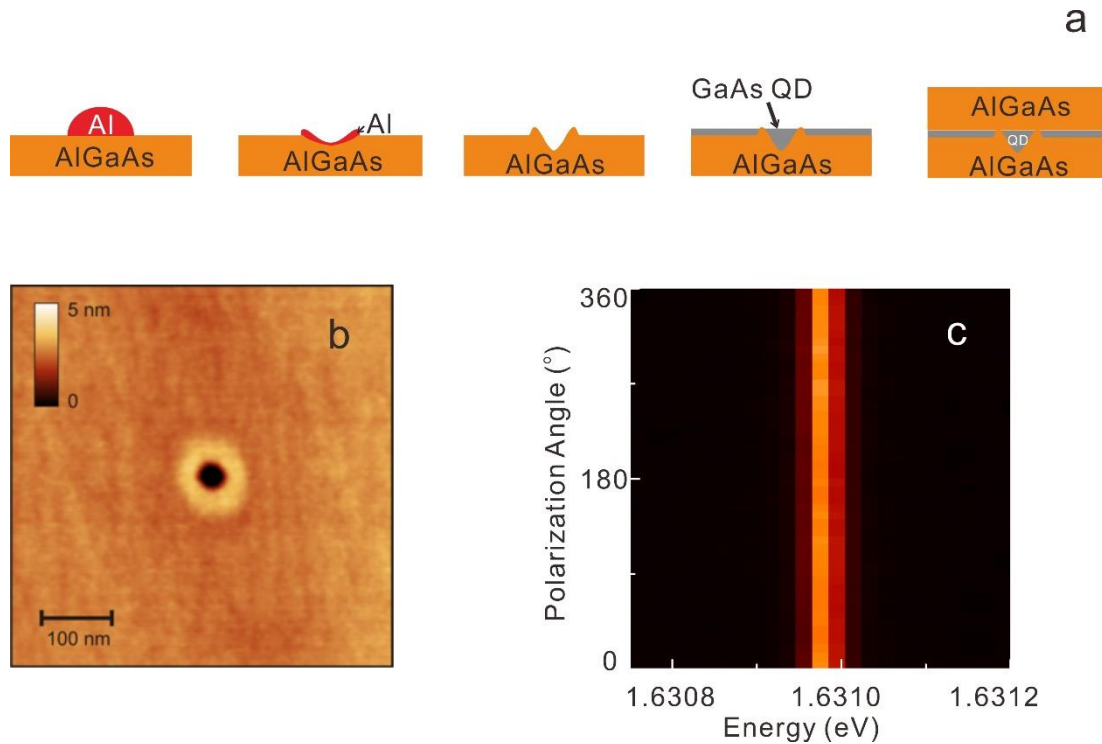
Fig. 2.7: (a) Sketch of the steps leading to GaAs QDs growth with the droplet etching method. (b) Typical AFM images of a nanohole obtained by Al droplet etching. Courtesy of Saimon Filipe Covre da Silva. (c) Polarization-resolved PL spectra of neutral exciton from GaAs QDs with droplet etching method. The excitonic FSS stemming from anisotropic exchange interaction is well below the resolution of the used setup because of the high in-plane symmetry of the QD.

2.2 Strain effects in bulk semiconductors

Strain is widely used to enhance the performance of semiconductor devices, such as in quantum well lasers based on lattice-mismatched heterostructures and in metal-oxide-semiconductor field-effect transistors (MOSFETs), where strain enhances carrier mobility[72]. In these applications, strain is built-in in the devices and cannot be varied after fabrication. For fundamental investigations and for fine tuning, it is instead desirable to be able to finely control the amplitude, configuration, and frequency of induced strain fields. This is conveniently achieved by using the piezoelectric effect, which transduces electrical signals into elastic deformations – the approach followed in this thesis. In this section, we will illustrate some of the effects produced by strain on semiconductors focusing on GaAs, the material used for our studies.

2.2.1 Band structure of GaAs

GaAs is a Ⅲ-Ⅴ direct bandgap (1.424 eV at room temperature) semiconductor with zincblende structure. As shown in Fig. 2.8 (a), the underlying Bravais lattice is the face-centered cubic (FCC) lattice, with basis consisting of two atoms (atoms of the group Ⅲ and Ⅴ are in purple and henna, respectively). One atom is at the origin of

the coordinates (0, 0, 0), another one is at $1/4(1, 1, 1)a$, where a is the length of the conventional cubic cell (lattice constant). Since GaAs is a direct bandgap semiconductor, a simplified band structure of bulk GaAs near Γ point ($\mathbf{k} = 0$) is shown in Fig. 2.8 (b). The behavior of electrons and holes are mostly determined by one conduction band (CB) and two valence bands (VB), since comparably large spin-orbit interaction energy Δ_{SO} (0.34 eV[73]) moves away to the split-off (SO) band from the top of the valence band. The upper valence bands, the heavy hole (HH) and light hole (LH) bands are energetically degenerate at the Γ point in absence of strain. In the Γ point, the bottom of the CB is energetically separate by the top of VBs by E_g, which is the energy bandgap.
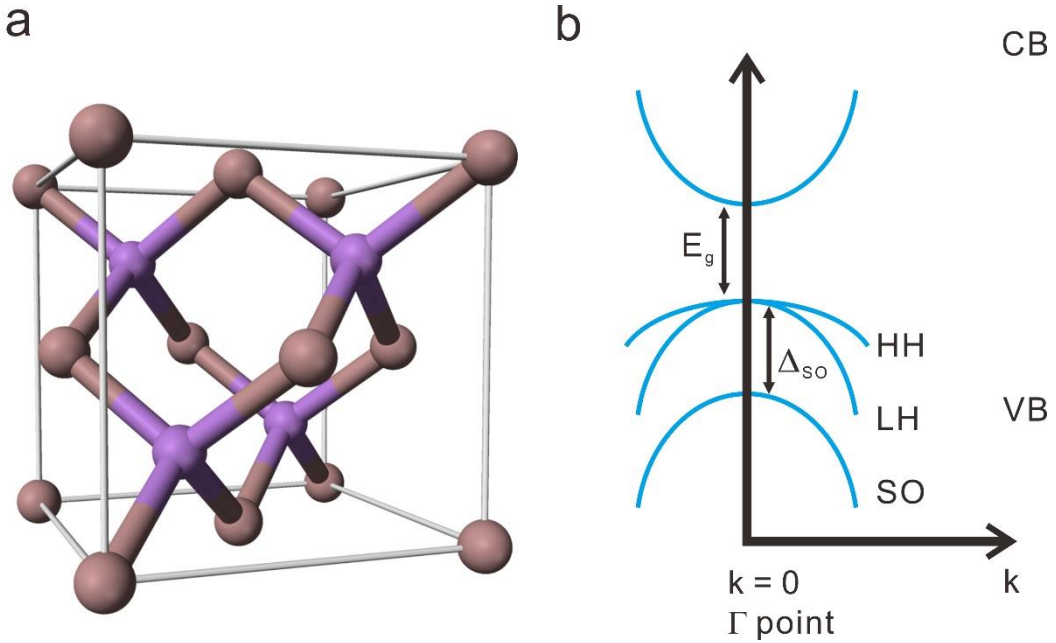
Fig. 2.8: (a) Crystal structure of GaAs, adapted from Wikipedia[74]. (b) Schematic picture of the band structure of bulk GaAs at Γ point.

2.2.2 Introduction of Bloch theorem and k·p theory

The $\boldsymbol{k \cdot p}$ theory is a powerful method to calculate the band structure and optical properties of semiconductors and their heterostructures based on a few empirical parameters describing the properties of the materials. In this section, we will give an introduction to the $\boldsymbol{k \cdot p}$ theory, mainly following the work by Chuang[73].

For an electron in a periodic potential:

$$V(\boldsymbol{r}) = V(\boldsymbol{r} + \boldsymbol{R}) \tag{2.8}$$

Where $\mathbf{R} = n_1\mathbf{a_1}+n_2\mathbf{a_2}+n_3\mathbf{a_3}$, $\mathbf{a_1}$, $\mathbf{a_2}$, $\mathbf{a_3}$ are the basic lattice vectors and n_1, n_2, n_3 are integers. The wave function of an electron must satisfy the Schrödinger equation:

$$H\psi(\mathbf{r}) = \left[\frac{-\hbar^2}{2m_0}\nabla^2 + V(\mathbf{r})\right]\psi(\boldsymbol{r}) = E\psi(\boldsymbol{r}), \tag{2.9}$$

Since the electron is in the periodic potential, $\psi(\boldsymbol{r} + \boldsymbol{R})$ will also be a solution of Eq. (2.9). In this case, $\psi(\boldsymbol{r} + \boldsymbol{R})$ will differ from $\psi(\boldsymbol{r})$ by just a phase. Hence, the general solution to the Schrödinger equation is given by:

$$\psi_{nk}(r) = e^{ikr}u_{nk}(r) \tag{2.10a}$$

where
$$u_{nk}(r + R) = u_{nk}(r) \tag{2.10b}$$

is a periodic function and k is the electron wavevector. This results is the well-known Bloch theorem and the wave function $\psi_{nk}(r)$ is called Bloch function. The corresponding energy is given by:

$$E = E_n(k), \tag{2.11}$$

with n an integer (band index). For each given n, there is a relation between the wave vector k and energy $E_n(k)$ (band dispersion), and one of the main applications of $k \cdot p$ theory is to calculate the band dispersion in the vicinity of a point k_0 in the first Brillouin zone. By inserting the solution (2.10a) into the Schrödinger equation:

$$\left[\frac{p^2}{2m_0} + V(r)\right]\psi_{nk}(r) = E_n(k)\psi_{nk}(r) \tag{2.12}$$

and expressing it in terms of $u_{nk}(r)$, we obtain:

$$\left[\frac{p^2}{2m_0} + \frac{\hbar}{m_0}k \cdot p + V(r)\right]u_{nk}(r) = \left[E_n(k) - \frac{\hbar^2 k^2}{2m_0}\right]u_{nk}(r) \tag{2.13}$$

The formula can be expanded near k_0.

$$(H_0 + H_1)u_{nk}(r) = \left[E_n(k) - \frac{\hbar^2 k^2}{2m_0}\right]u_{nk}(r) \tag{2.14}$$

With
$$H_0 = \frac{p^2}{2m_0} + V(r) \tag{2.15}$$

$$H_1 = \frac{\hbar}{m_0}k \cdot p \tag{2.16}$$

When k is sufficiently small, the $k \cdot p$ term in H_1 can be treated as a perturbation, and the H_0 is an "unperturbed Hamiltonian", this is the reason why this formalism is called "$k \cdot p$" theory. If the Hamiltonian H_0 has a set of orthonormal eigenfunctions at $k = 0$ (supposed to be known),

$$H_0 u_{n0}(r) = E_{n0}u_{n0}(r) \tag{2.17}$$

then any lattice periodic function can be written as a linear combination of $u_{n0}(r)$. In other words, we can express the periodic wavefuntions away from the Γ point as:

$$u_{nk} = \sum_m c_m^n(k)u_{m0} \tag{2.18}$$

To give a brief description of the calculation of the band structure with the $k \cdot p$ theory, we consider a single band model, i.e., we focus on a specific, non-degenerate, band (labelled n) and we label the other bands as n'. The energy can be expanded to second order time-independent perturbation:

$$E_n(k) = E_n(0) + \frac{\hbar^2 k^2}{2m_0} + \frac{\hbar}{m_0}k \cdot p_{nn} + \frac{\hbar^2}{m_0^2}\sum_{n' \neq n}\frac{|k \cdot p_{nn'}|^2}{E_n(0) - E_{n'}(0)} \tag{2.19}$$

and the wave function in first-order perturbation is:

$$u_{nk} = u_{n0}(r) + \sum_{n' \neq n}\left[\frac{\hbar}{m_0}\frac{k \cdot p_{n'n}}{E_n(0)E_{n'}(0)}\right] \tag{2.20}$$

with the momentum matrix element defined as:

$$p_{nn'} = \int_\Omega u_{n0}^*(r)pu_{n'0}(r)d^3r \tag{2.21}$$

Here Ω is the volume of the unit cell. In the case of GaAs, at the Γ point ($k_0 = 0$) is the extremum of $E_n(k)$, which means $E_n(k)$ must depend quadratically on k and $p_{nn} = 0$. The

formula (2.19) can be rewritten as:

$$E_n(\boldsymbol{k}) - E_n(0) = \sum_{\alpha,\beta} D^{\alpha\beta} k_\alpha k_\beta = \frac{\hbar^2}{2} \sum_{\alpha,\beta} \left(\frac{1}{m^*}\right)_{\alpha\beta} k_\alpha k_\beta \tag{2.22}$$

Where $\alpha, \beta = x, y \ and \ z$. The matrix $D^{\alpha\beta}$ is an element of the inverse effective mass tensor multiplied $\hbar^2/2$, which is an important parameter determined by the coupling with the other bands[75]. Here we just discussed how $\boldsymbol{k \cdot p}$ theory works in a single band case, the situation will become more complicated if more bands are considered, which is the case for the degenerate valence bands. More details on the multi-band $\boldsymbol{k \cdot p}$ theory can be found in Refs.[73,75].

2.2.3 Strain effects in semiconductors

Strain describes the deformation of a solid with with respect to its equilibrium configuration in response to applied forces (stresses). For simplicity, we start from a 2D model. As illustrated in Fig. 2.9, we imagine two unit vectors $\boldsymbol{x_0}$, $\boldsymbol{y_0}$ anchored to the unstrained lattice. If the lattice is strained, a deformation will occur and the vectors will be distorted. In case of small deformations, the new vectors $\boldsymbol{x_1}$, $\boldsymbol{y_1}$ can be written as:

$$\boldsymbol{x_1} = (1 + \varepsilon_{xx})\boldsymbol{x_0} + \varepsilon_{xy}\boldsymbol{y_0} + \varepsilon_{xz}\boldsymbol{z_0}$$
$$\boldsymbol{y_1} = \varepsilon_{yx}\boldsymbol{x_0} + \left(1 + \varepsilon_{yy}\right)\boldsymbol{y_0} + \varepsilon_{yz}\boldsymbol{z_0} \tag{2.23}$$

If we generalize to the 3D case, one more vector z_1 will be obtained:

$$\boldsymbol{z_1} = \varepsilon_{zx}\boldsymbol{x_0} + \varepsilon_{zy}\boldsymbol{y_0} + (1 + \varepsilon_{zz})\boldsymbol{z_0} \tag{2.24}$$
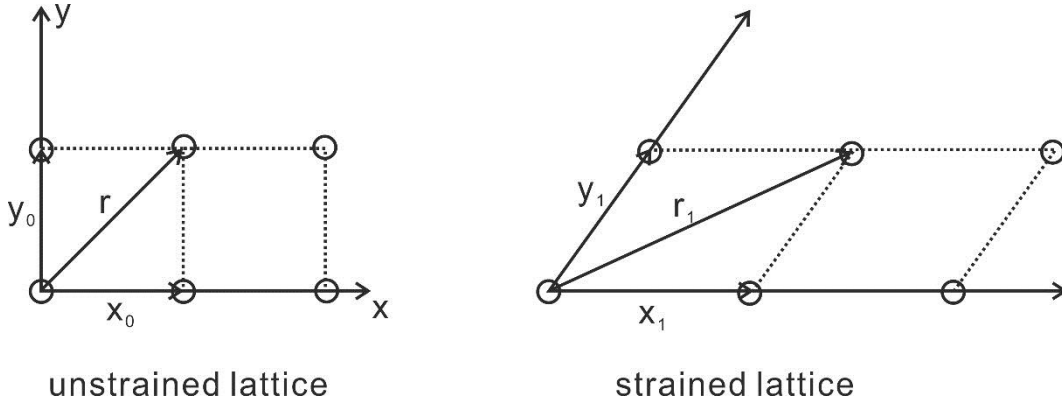
Fig. 2.9: Sketch of an unstrained crystal lattice and strained lattice.

Besides that, homogeneous strain is assumed here and the ε_{ij} in Eqs. (2.23) and (2.24) can be chosen so that they form the elements of a symmetric strain tensor of second order ($\varepsilon_{ij} = \varepsilon_{ji}$).

In the linear regime, the stress-strain relations can be written in matrix form using the generalized Hooke's law: $\sigma_{ij} = c_{ijkl}\varepsilon_{kl}$, where c_{ijkl} are elements of a 4-th rank stiffness tensor. Using the fact that both the stress and strain tensors are symmetric, the number of independent elements of such tensor can be substantially reduced and the Hooke's law can be written using the Voigt notation.

For a cubic crystal:

$$\begin{pmatrix} \sigma_{xx} \\ \sigma_{yy} \\ \sigma_{zz} \\ \sigma_{yz} \\ \sigma_{xz} \\ \sigma_{xy} \end{pmatrix} = \begin{pmatrix} C_{11} & C_{12} & C_{12} & 0 & 0 & 0 \\ C_{12} & C_{11} & C_{12} & 0 & 0 & 0 \\ C_{12} & C_{12} & C_{11} & 0 & 0 & 0 \\ 0 & 0 & 0 & C_{44} & 0 & 0 \\ 0 & 0 & 0 & 0 & C_{44} & 0 \\ 0 & 0 & 0 & 0 & 0 & C_{44} \end{pmatrix} \begin{pmatrix} \varepsilon_{xx} \\ \varepsilon_{yy} \\ \varepsilon_{zz} \\ 2\varepsilon_{yz} \\ 2\varepsilon_{xz} \\ 2\varepsilon_{xy} \end{pmatrix} \tag{2.25}$$

In the following, we only consider the Γ point at the Brillouin zone. Besides, since the CB is energetically well separated from the VBs, we neglect coupling and treated separately the CB and the VBs. The basis states for electrons in the CB and holes in the HH, LH, SO bands at the Γ point are written as[73]:

$|u_{CB}^1\rangle = iS \uparrow; \qquad |u_{CB}^2\rangle = iS \downarrow$

$|u_{HH}^1\rangle = -\frac{1}{\sqrt{2}}(X + iY) \uparrow;$

$|u_{LH}^1\rangle = -\frac{1}{\sqrt{6}}[(X + iY) \downarrow -2Z \uparrow]; \quad |u_{LH}^2\rangle = \frac{1}{\sqrt{6}}[(X - iY) \uparrow +2Z \downarrow] \tag{2.26}$

$|u_{HH}^2\rangle = \frac{1}{\sqrt{2}}(X - iY) \downarrow$

$|u_{SO}^1\rangle = \frac{1}{\sqrt{3}}[(X + iY) \downarrow +Z \uparrow]; \quad |u_{SO}^2\rangle = \frac{1}{\sqrt{3}}[(X - iY) \uparrow -Z \downarrow]$

Here X, Y, Z have the same angular dependence as $(\cos\varphi \sin\theta, \sin\varphi \sin\theta, \cos\theta)$ and the arrows stand for the different spin orientation along z direction. Based on this basis, the Luttinger-Kohn and Pikus-Bir Hamiltonian can be expressed as:

$$H = - \begin{pmatrix} -C & 0 & 0 & 0 & 0 & 0 & 0 & 0 \\ 0 & -C & 0 & 0 & 0 & 0 & 0 & 0 \\ 0 & 0 & P+Q & -S & R & 0 & -\frac{S}{\sqrt{2}} & \sqrt{2}R \\ 0 & 0 & -S^+ & P-Q & 0 & R & -\sqrt{2}Q & \sqrt{\frac{3}{2}}S \\ 0 & 0 & R^+ & 0 & P-Q & S & \sqrt{\frac{3}{2}}S^+ & \sqrt{2}Q \\ 0 & 0 & 0 & R^+ & S^+ & P+Q & -\sqrt{2}R^+ & -\frac{S^+}{\sqrt{2}} \\ 0 & 0 & -\frac{S^+}{\sqrt{2}} & -\sqrt{2}Q^+ & \sqrt{\frac{3}{2}}S & -\sqrt{2}R & P+\Delta & 0 \\ 0 & 0 & \sqrt{2}R^+ & \sqrt{\frac{3}{2}}S^+ & \sqrt{2}Q^+ & -\frac{S}{\sqrt{2}} & 0 & P+\Delta \end{pmatrix} \tag{2.27}$$

with

$C = E_v + E_g + C_k + C_\varepsilon, \quad C_k = \frac{\hbar^2 k^2}{2m^*}, \qquad C_\varepsilon = a_c(\varepsilon_{xx} + \varepsilon_{yy} + \varepsilon_{zz})$

$P = E_v + P_k + P_\varepsilon, \quad P_k = \frac{\hbar^2 k^2}{2m}\gamma_1, \qquad P_\varepsilon = -a_v(\varepsilon_{xx} + \varepsilon_{yy} + \varepsilon_{zz})$

$Q = Q_k + Q_\varepsilon, \quad Q_k = \frac{\hbar^2}{2m}\gamma_2(k^2 - 3k_z^2), \quad Q_\varepsilon = -\frac{b}{2}(\varepsilon_{xx} + \varepsilon_{yy} - 2\varepsilon_{zz})$

$$R = R_k + R_\varepsilon, \quad R_k = \frac{\hbar^2}{2m}\left(\gamma_2\left(k_x^2 - k_y^2\right) + 2i\sqrt{3}\gamma_3 k_y k_x\right), \quad R_\varepsilon$$

$$= \frac{\sqrt{3}b}{2}(\varepsilon_{xx} - \varepsilon_{yy}) - id\varepsilon_{zy}$$

$$S = S_k + S_\varepsilon, \quad S_k = \frac{\hbar^2}{2m}\gamma_3\sqrt{3}(k_x k_z - ik_y k_z), \quad S_\varepsilon = -d(\varepsilon_{xz} - i\varepsilon_{yz})$$

x, y, z correspond to the [100], [010] and [001] crystal direction. E_g is the energy bandgap, E_v is the energy of the HH and LH valence bands at the Γ point in absence of strain and Δ is the spin-orbit split off energy; the parameters γ are the Luttinger parameters, m^* is the electron effective mass and a_c, a_v, b, d are the deformation potentials.

As an example, we consider a biaxial isotropic strain in the (001) plane, characterized by $\varepsilon_{xx} = \varepsilon_{yy}$ and neglect the split-off bands because of their large energy separation from the HH and LH bands.

The total simplified Hamiltonian for the valence bands is given in matrix form:

$$H = H_k + H_\varepsilon = -\begin{pmatrix} P_k + Q_k & -S_k & R_k & 0 \\ -S_k^+ & P_k - Q_k & 0 & R_k \\ R_k^+ & 0 & P_k - Q_k & S_k \\ 0 & R_k^+ & S_k^+ & P_k + Q_k \end{pmatrix} - \begin{pmatrix} P_\varepsilon + Q_\varepsilon & 0 & R_\varepsilon & 0 \\ 0 & P_\varepsilon - Q_\varepsilon & 0 & R_\varepsilon \\ R_\varepsilon^+ & 0 & P_\varepsilon - Q_\varepsilon & 0 \\ 0 & R_\varepsilon^+ & 0 & P_\varepsilon + Q_\varepsilon \end{pmatrix} \quad (2.28)$$

The first term H_k contains the "kinetic energy" obtained from $\boldsymbol{k \cdot p}$ theory and the second term H_ε includes the contributions from the strain.

With the biaxial isotropic strain, the whole Hamiltonian will be reduced to:

$$H = \begin{pmatrix} P_\varepsilon + Q_\varepsilon & 0 & 0 & 0 \\ 0 & P_\varepsilon - Q_\varepsilon & 0 & 0 \\ 0 & 0 & P_\varepsilon - Q_\varepsilon & 0 \\ 0 & 0 & 0 & P_\varepsilon + Q_\varepsilon \end{pmatrix} \quad (2.29)$$

Since the matrix takes a diagonal form, the eigenvalues of the Hamiltonian will be the diagonal elements. We see that the effect of biaxial us to split the HH and LH bands by $2Q_\varepsilon$. In Figure 2.10, we plot a simplified band structure of GaAs under biaxial isotropic strain (both under compression and tension[III]).

For the anisotropic strain situation, the Pikus-Bir Hamiltonian will not be diagonal anymore, which will be more complicated and we will discuss in Chapter 4.

[III] For instance, under compressive strain $\varepsilon_{xx} = \varepsilon_{yy} < 0$, we obtain a positive Q_ε. The positive Q_ε results in a rise of HH above the LH. Under tensile strain, we have the opposite situation.

(a) (b) (c)
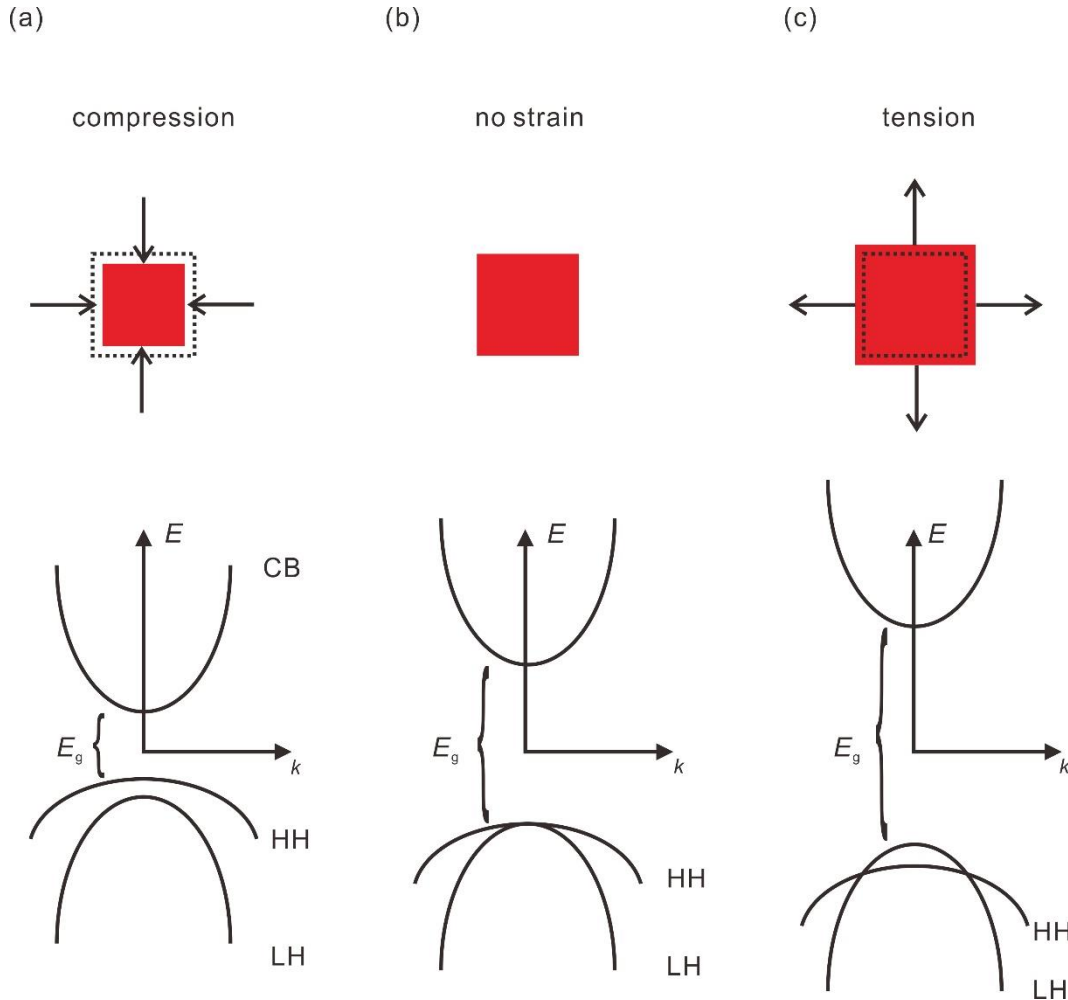
Fig. 2.10: Simplified energy band-gap of bulk GaAs with (a) isotropic biaxial compressive strain, (b) no strain, and (c) isotropic tensile strain. The top sketches show the corresponding in-plane deformations.

2.3 Surface acoustic waves

Surface acoustic waves (SAWs) are elastic waves, which propagate along the surface of elastic materials. The concept was first introduced in 1885 by Lord Rayleigh[76]. Nowadays SAWs are widely used in various fields, like electronic components, geophysics, microfluidics and so on. As we discussed before, QDs are considered as one the most promising quantum light source, their manipulation with SAWs could be a method with infinite possibilities in quantum computation[77,78] and quantum information transfer[79].

Elastic vibration and acoustic waves are not only widely used in engineering, but are also important and powerful tools to study fundamental properties of condensed matter systems. In this section, we will give an introduction of elastic vibrations and surface acoustic waves in GaAs, the general idea here follows Ref[80,81], where more detailed information can be found.

2.3.1 Elastic vibrations in solid matter

In homogeneous elastic medium, by using Newton's second law we can get:

$$\nabla \cdot \sigma = \rho \frac{\partial^2 \boldsymbol{u}(\boldsymbol{r})}{\partial t^2} \tag{2.30}$$

Here σ is stress tensor, ρ is the density of material and $\boldsymbol{u}(\boldsymbol{r})$ is the displacement field. If consider further more on the strain ε, which can be expressed as:

$$\varepsilon_{kl} = \frac{1}{2}\left(\frac{\partial u_k}{\partial x_l} + \frac{\partial u_l}{\partial x_k}\right) \tag{2.31}$$

Using the generalized Hooke's law, we obtain:

$$\rho \frac{\partial^2 u_i}{\partial^2 t^2} = \frac{\partial}{\partial x_j} c_{ijlk} \left(\frac{\partial u_k}{\partial x_l} + \frac{\partial u_l}{\partial x_k}\right) \tag{2.32 a}$$

This equation describes the wave propagation in bulk crystal (without considering other effects, like piezoelectric effect). Furthermore, if we consider the cubic crystal structure of GaAs and the x-direction plane wave of $u_i = u_{i,0} \cdot exp[i(kx_i - \omega t)]$, we obtain:

$$\rho \frac{\partial^2 u_1}{\partial^2 t^2} = c_{11} \frac{\partial^2 u_1}{\partial x_1^2}$$

$$\rho \frac{\partial^2 u_2}{\partial^2 t^2} = c_{44} \frac{\partial^2 u_2}{\partial x_1^2}$$

$$\rho \frac{\partial^2 u_3}{\partial^2 t^2} = c_{44} \frac{\partial^2 u_3}{\partial x_1^2} \tag{2.32 b}$$

In this case, we assume uncoupled vibrations, u_1 corresponds to a longitudinal wave, while u_2 and u_3 stand for the transverse ones, the dispersion relations and the phase velocities of the longitudinal and transverse waves are:

$$\omega_l = \sqrt{\frac{c_{11}}{\rho}} \cdot k \leftrightarrow v_l = \sqrt{\frac{c_{11}}{\rho}}$$

$$\omega_t = \sqrt{\frac{c_{44}}{\rho}} \cdot k \leftrightarrow v_t = \sqrt{\frac{c_{44}}{\rho}} \tag{2.33}$$

2.3.2 Rayleigh waves in GaAs

GaAs is a well-known piezoelectric material. Considering the piezoelectric effect, the stress tensor σ should be rewritten as:

$$\sigma_{ij} = c_{ijkl}S_{kl} - e_{kij}E_k, \tag{2.34}$$

where e_{kij} are the components of the piezoelectric tensor and E_k is the electric field. The electric displacement field D_i can be expressed as:

$$D_i = e_{ijk}S_{jk} + \epsilon_{ij}E_j \tag{2.35}$$

$E(\boldsymbol{r}) = -\nabla\phi$ is the resulting electric field. Compared to the speed of light, the velocity of sound waves is nearly 10^5 times lower, which justifies the use of a quasi-electrostatic equation, with ϕ is the electrostatic potential. When a time periodic displacement $\boldsymbol{u}(t) = \boldsymbol{u}_0 e^{-i\omega t}$ is given and no free charge is present ($\nabla \cdot D = 0$), the propagation of waves can be described as follows:

$$\rho \frac{\partial^2 u_i}{\partial t^2} = c_{ijkl} \frac{\partial^2 u_l}{\partial x_j \partial x_k} + e_{kij} \frac{\partial^2 \phi}{\partial x_j \partial x_k}$$

$$\epsilon_{ij} \frac{\partial^2 \Phi}{\partial x_i \partial x_j} = e_{ijk} \frac{\partial^2 u_i}{\partial x_j \partial x_k} \tag{2.36}$$

The elastic wave is accompanied by a wave of electric field, and the medium behaves more stiff because of the piezoelectric coupling. Compared to the elastic vibration in a non-piezoelectric material (equation (2.31)), the velocity is increased by a small factor, which is also referred to as *piezoelectric stiffening*[82]. There is a specific wave propagating along the solid surface, which is called Rayleigh wave (The existence of the waves is predicted by Lord Rayleigh in 1885)[76]. For unload surface, the Rayleigh wave exists and consists of a linear combination of longitudinal and transverse vibrations. Here we can get two boundary conditions for a Rayleigh wave: 1) There will be no stress along the vertical (z) direction perpendicular to the surface; 2) The z-component of the electric displacement field is continuous at the surface:

$$(T_{xz} = T_{yz} = T_{zz})|_{z=0} = 0$$
$$D_z|_{z=dz} = D_z|_{z=-dz} \tag{2.37}$$

As the components in z-direction of the stress tensor vanish at the surface, we expect the amplitude of the waves to decrease exponentially with increasing depth. This means that a Rayleigh wave only exists on the surface of a solid (within a depth less than one wavelength)[83]. With the obtained boundary conditions above, the time periodic displacement components derived from the equation (2.30) are given by[82]:

$$u_x = A_x \sin(kx - v_{SAW} t)$$
$$u_z = A_z \cos(kx - v_{SAW} t), \tag{2.38}$$

with A_x, A_z are the amplitudes of the u_x and u_z. v_{SAW} is the SAW phase velocity, which is determined by the elastic properties. From the formula (2.38), we can see the Rayleigh waves cause a surface point to move in ellipses in the plane normal to the surface and parallel to the propagation direction. On the (001) GaAs, the velocity of SAW along [110] $v_{SAW} = 2864$ m/s[84] at room temperature and will slightly increase at cryogenic temperatures. The phase velocity of the SAW is in linear relation with frequency:

$$v_{SAW} = \lambda_{SAW} \cdot f_{SAW} \tag{2.39}$$

Thanks to the increasing computing power of modern computers, we can now find numerical solutions for the wave equations. As described above, we use COMSOL Multiphysics. In Fig. 2.11, we plot the electric potential ϕ map of (001) GaAs when a SAW is propagating along the [110] direction. The arrows indicate the electric fields arise from the deformation.
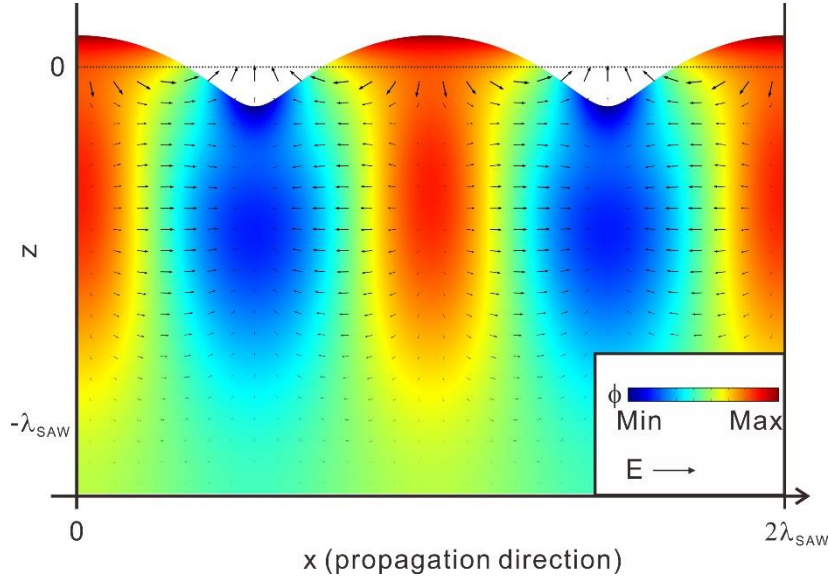
Fig. 2.11: Result of the simulation of SAW propagation in (001) GaAs. The propagation direction [110] is defined as x-direction and the vertical direction is the z-direction. The dashed line is the original surface without SAW. The color mapping encodes the electric potential ϕ caused by the SAW, and electric field E is marked with arrows, with length proportional to its magnitude.

2.3.3 Interdigital transducers (IDTs)

The primary function of IDTs is to convert electric signals to SAWs by generating periodically distributed mechanical forces via the piezoelectric effect. With (001) GaAs used in our experiment, the IDT should be aligned along the [110] direction, since that direction has the strongest piezoelectric coupling. Generally an IDT consists of a comb-like pattern of metallic electrodes, and was first proposed by White *et al*. in 1965[85]. One part of the IDT is grounded, and another is connected to the signal generator. As shown in Fig. 2.12, there are two typical types of IDT used in our experiment. Fig. 2.12 (a) shows the most basic one, which is called Split-1, p stands for the period of this IDT. If we use λ as the wavelength of sound waves, the relation between p and λ can be written as (2n+1) λ = p, where n is an integer. When n = 0, we can get a fundamental wavelength λ_0, the corresponding frequency is called fundamental frequency. When n > 0, higher order harmonic wavelengths and frequencies are obtained. With this IDT, the high harmonic frequency is always the odd times of the fundamental frequency. Another kind of IDT is shown in Fig. 2.12 (b), which is called Split-52. Due to the special geometry arrangement of the electrode pattern both even and odd harmonic wavelengths (or frequencies) can be generated. Denoting the fundamental wavelength as λ_1. High order harmonic wavelengths can be generated:

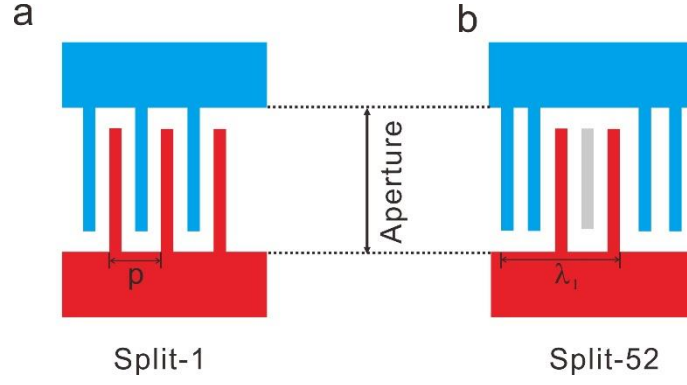$$\lambda_1, \lambda_1/2, \lambda_1/3, \lambda_1/4, \lambda_1/6 \cdots$$

Fig. 2.12: Sketch of the (a) Split-1 and (b) Split-52 IDT. The period of Spilt-1 is marked as p and the fundamental wavelength of Split-52 is λ_1.

2.3.4 Lamb waves

Lamb waves refer to elastic waves which can propagate in a system with two free surfaces (plate, layer or bar)[86,87], [88]

Due to the presence of two free surfaces, Lamb waves are the result of interference between waves propagating at the two surfaces. .

The analytical solution to Lamb wave can generally be thought as follows (for more detailed information can be found in Ref[89]). Here we take a simple geometry of a solid medium bounded by two parallel planes (with a distance of 2d)) and the coordinate system is illustrated in Fig. 2.13, the propagation direction is assumed as x. Basic Lamb waves can be classified as symmetric and antisymmetric modes, as sketched in Fig. 2.14 (a), which are described as follows[90]:

$$\frac{\partial^2 u}{\partial x^2} + \frac{\partial^2 u}{\partial z^2} = \frac{1}{c_L^2}\frac{\partial^2 u}{\partial t^2} \qquad \text{longitudinal wave}$$

$$\frac{\partial^2 w}{\partial x^2} + \frac{\partial^2 w}{\partial z^2} = \frac{1}{c_T^2}\frac{\partial^2 w}{\partial t^2} \qquad \text{transverse wave} \qquad (2.40)$$

with c_L and c_T are the velocity of longitudinal and transverse waves. Two types of solutions exist in the Lamb wave systems: symmetric, with the longitudinal displacement component $u(z) = u(-z)$; and antisymmetric, with displacement $u(-z) = -u(z)$. By denoting with w the transverse component of displacement, for symmetric modes:

$$u = (ikA\cos(pz) + qB\cos(qz))e^{ik(x-ct)}$$
$$w = (-pA\sin(pz) - ikB\sin(qz))e^{ik(x-ct)} \qquad (2.41)$$

and for antisymmetric modes:

$$u = (ikC\sin(pz) - qD\sin(qz))e^{ik(x-ct)}$$
$$w = (pC\cos(pz) - ikD\cos(qz))e^{ik(x-ct)} \qquad (2.42)$$

, $p = \frac{\omega}{\sqrt{c_L^2 - c^2}}$, $q = \frac{\omega}{\sqrt{c_T^2 - c^2}}$, $\omega = 2\pi f$ is the angular frequency. And A, B, C, and D are

constants. If the boundary conditions ($\sigma_{xz} = \sigma_{zz} = 0$ on $z = \pm d/2$) are imposed, two characteristic equations are satisfied[91]:

For symmetric modes, $\qquad \dfrac{tan(qd)}{tan(pd)} = -\dfrac{4k^2pq}{(q^2-k^2)^2}$ $\qquad\qquad (2.43)$

For antisymmetric modes,
$$\frac{tan(pq)}{tan(qd)} = -\frac{4k^2pq}{(q^2-k^2)^2} \tag{2.44}$$

With these two equations, two important conclusions can be obtained. Firstly, c is a function of ω, which means the waves are dispersive. The second fact is that the equations are transcendental, depending on the value of ωd, may have many number of real solutions, which are divided into the two kinds of modes: symmetric and antisymmetric (all these modes are schematically shown in Fig. 2.14 (b)). At low frequency, due to a certain threshold, only one symmetric and antisymmetric mode exist, which usually are called fundamental modes S_0 and A_0. The zero fundamental symmetric mode S_0 corresponds to the wave of expansion-compression and the zero fundamental antisymmetric mode A_0 refers to bending wave. Similar to the Rayleigh wave, although it is possible to solve numerically the dispersion relation of Lamb wave relations in given plate, here we still use the COMSOL Multiphysics to simulate the Lamb wave in our samples.
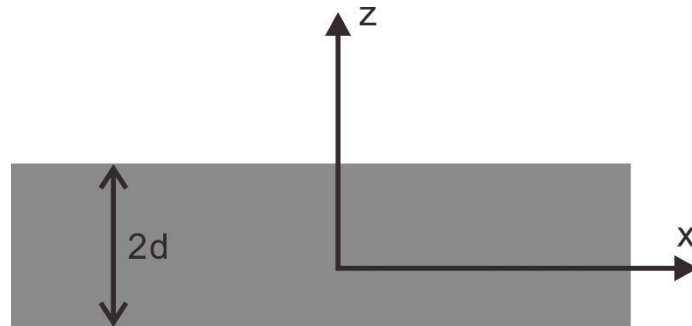

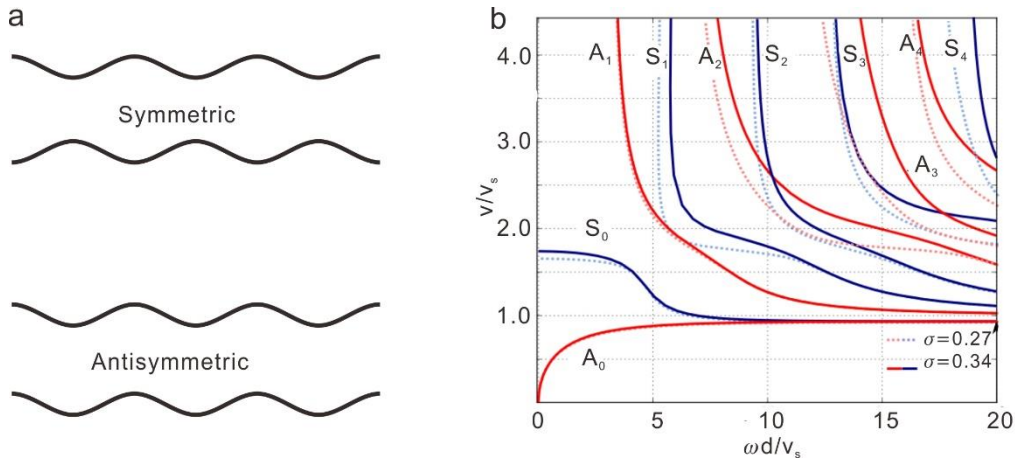**Fig. 2.13**: Coordinate system for Lamb wave in a plate.

Fig. 2.14: (a) Schematic representation of normal symmetric and antisymmetric modes. (b) Dispersion curves of Lamb waves in solid plates (with different Poisson ratios σ). A_i and S_i are the antisymmetric and symmetric modes, respectively. Adapted from[92].

3. Experimental methods, devices and FEM simulations

This chapter will present the necessary experimental details, which consist of concepts and fabrication methods of devices used in this thesis, experimental setups and related finite-element-method (FEM) simulations based on COMSOL Multiphysics.

3.1 Strain tuning of QDs

As the research enthusiasm on semiconductor QDs raised up over the last three decades, various post-growth tuning methods emerged to make QDs suitable for specific experiments and applications. As we discussed in the first two chapters, there is no doubt that strain fields[IV] represent a very versatile tool for controlling the properties of QDs. Approaches to induce strain include oxide coating[93,94], mechanical bending of the semiconductor hosting the QDs[95,96], and bonding to piezoelectric actuators[41–43]. The latter is particularly appealing for fundamental studies, as it allows the QD properties to be tuned in-situ, i.e. during optical measurements and is compatible with on-chip integration.

3.1.1 Integration of QDs on monolithic piezoelectric actuators

3.1.1.1 PMN-PT piezoelectric actuator

The first work using a piezoelectric actuator to control the emission properties of QDs can be tracked back to 2006, in which $Pb(Zr, Ti)O_3$ (PZT) stacks were employed to control in a limited range the emission energy and FSS of QDs. After that, due to its exceptional piezoelectric properties, $(1\text{-}x)[Pb(Mg_{1/3}Nb_{2/3})O_3]\text{-}x[PbTiO_3]$ (PMN-PT) replaced PZT and is now used by several groups to tune QD properties. In this thesis, we also used mostly (001)-cut PMN-PT substrates. We discuss here briefly their working principles.

According to literature[97], PMN-PT is a relaxor ferroelectric material, which shows excellent piezoelectric properties and little hysteresis. Although the (111) oriented PMN-PT possess some unique and interesting properties, its piezoelectric constants are much lower than the (001) oriented ones, this is the reason why we choose the (001) oriented ones. From the chemical formula, we see that the PMN-PT is a solid solution of $Pb(Mg_{1/3}Nb_{2/3})O_3$ (PMN) and $PbTiO_3$ (PT). The composition of this solution has a strong influence on the piezoelectric properties. Based on previous reports, a (1-

---

[IV] The strain here is defaulted as static strain.

x)PMN-xPT solid solution with $x = 0.3$ will ensure a large piezoelectric response and preserve a stable compositional stability of the crystal. In our work, the PMN-PT substrates are purchased from TRS Technologies and have $x = 0.28$. An important parameter for ferroelectric materials is the Curie temperature T_c, a critical temperature above which the ferroelectric material becomes paraelectric. PMN-PT can feature an intrinsic electric polarization below T_c (~130 °C). When we apply an electric field F_p to the PMN-PT along specific crystal directions, the dipole moments will align with the electric field F_p if the electric field is larger than the coercive field (F_c) and keep aligned even once F_p is removed. We call the process, which aligns the dipole moments as "poling", which is necessary before using the PMN-PT as piezoelectric actuator.

Fig. 3.1 (a) illustrates schematically the in-plane strain when an electric field is applied to a poled PMN-PT substrate. The top and bottom sides of the PMN-PT are coated with gold, which acts as electrode. The thickness of PMN-PT substrate used in this work is about 300 μm. Since the semiconductor structure with embedded QDs is bonded on the surface of PMN-PT substrate, in-plane strain can be transferred to the QDs. For (001)-cut PMP-PT, the induced strain can be considered as quasi-isotropic biaxial. The strain configuration on the sidewalls of the PMN-PT substrate is instead strongly anisotropic and was employed in a previous work[98]. The drawback of that approach is that the available surface for semiconductor bonding and the tuning range were both limited. In this thesis we have developed a much more reliable method to apply uniaxial stress to QDs, which we will discuss in Sec. 3.2.2.

Figure 3.1 (b) shows the room temperature in-plane strain dependence as a function of the applied electric field. In this thesis, the substrates are poled by application of a positive electric field. The corresponding strain relation is displayed by the red curve: compressive strain is obtained when $F_p > 0$, while for $F_p < 0$ we get tensile strain. However, the ferroelectric domains will undergo a reversal of the polarization if the electric field F_p keeps decreasing and reaches the coercive field -$|F_c|$. The situation is different at the cryogenic temperatures used in our experiments (5 K)[99]. Due to an exponential increase of the coercive field of PMN-PT with decreasing temperature[100], F_c can be as large as 100 kV/cm, which allows us to achieve broad-range tuning both in the compressive and tensile regime. On the other hand, the poling should always be performed at room temperature, since the coercive field F_c at low temperature is too large.
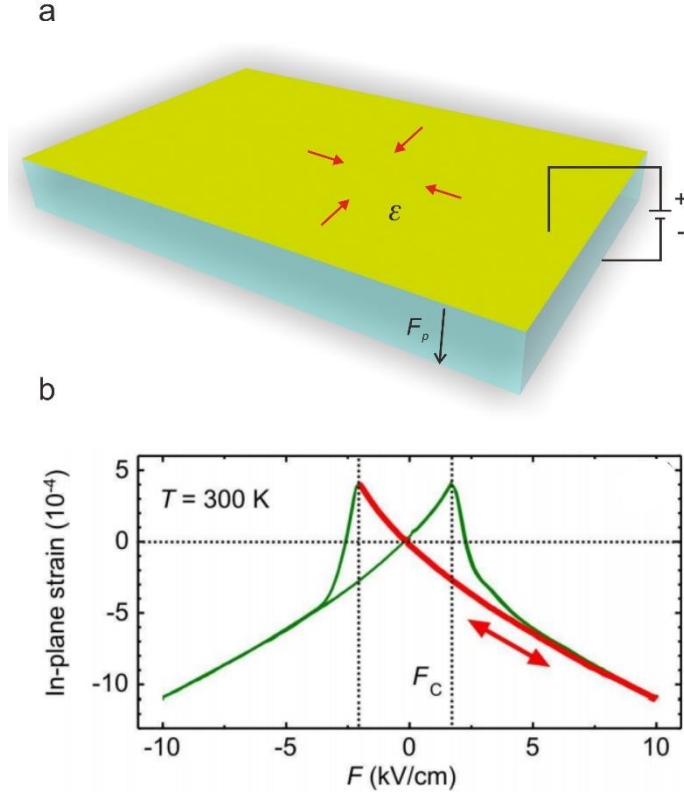
Fig. 3.1: (a) Sketch of a (001)-cut PMN-PT piezoelectric substrate when an electric field F_p is applied across it. In-plane biaxial strain ε is produced by the piezoelectric actuator when an electric field is applied. The top and bottom of the piezoelectric substrate are coated with gold electrodes. (b) In-plane strain dependence with electric field, the data is measured at 300 K. Figure adapted from[43].

3.1.1.2 Fabrication and state of art of QDs integrated on monolithic PMN-PT substrates

A strain-tunable QD-monolithic-PMN-PT device can be processed as follows (schematically shown in Fig. 3.2 (a)): First, a proper sample consists of a GaAs substrate, sacrificial layer, and QDs-containing layer. Usually, the sacrificial layer is $Al_xGa_{1-x}As$ layer (x > 0.6, in our work x = 0.75), which can be easily chemically etched to release the active layers in the form of membranes. Second, standard photolithography, metal deposition, and lift-off are sequentially performed. A 3 nm-thick chromium layer and a 100 nm-thick gold layer are deposited as a metal layer, the chromium layer acts as an adhesive layer between GaAs and gold. After lift-off, the remaining metal layer is used as a mask for a mixed solution of $H_2SO_4:H_2O_2:H_2O$ (volume ratio 1:8:200, with an etching rate of about 200 nm/min). The sample is immersed into the etching solution until the $Al_xGa_{1-x}As$ sacrificial layer is reached. After that, the etched sample is put into diluted Hydrofluoric (HF) Acid solution (usually the concertation of 10% is used in our work) to etch away the $Al_xGa_{1-x}As$ sacrificial layer. Then the membranes with embedded QDs are detached from the GaAs

31

substrate and loosely lie on it. Before transferring the membranes onto the PMN-PT, the raw PMN-PT substrate is lapped (from a thickness of ~500 µm down to a thickness of ~300 µm), followed by polishing to get a smooth surface, which is vital for the following bonding step. Another two Cr/Au (3/100 nm) layers are deposited on the top and bottom sides of the polished PMN-PT actuator.

The final step consists in the transfer the semiconductor membranes to the PMN-PT substrate, which is accomplished with a Finetech (FINEPLACER lambda) die-bonding machine. As for the bonding, different alternative approaches can be chosen, such as using polymers (e.g., PMMA and SU8) as a "glue" or the gold-to-gold thermocompression bonding. Although these two methods have different advantages, the bonding steps are quite similar. Illustrated in step 5 in Figure 3. 2(a), the flipped QD-sample is pressed on the PMN-PT substrate, a simultaneous heating is applied for better bonding between the membrane and the PMN-PT substrate. After some time (20~30 minutes) for bonding, we remove the GaAs substrate and leave the QD-membranes bonded on the surface of the PMN-PT substrate. Fig. 3.2 (b) is a typical microscope photograph of a membrane bonded on the PMN-PT substrate.
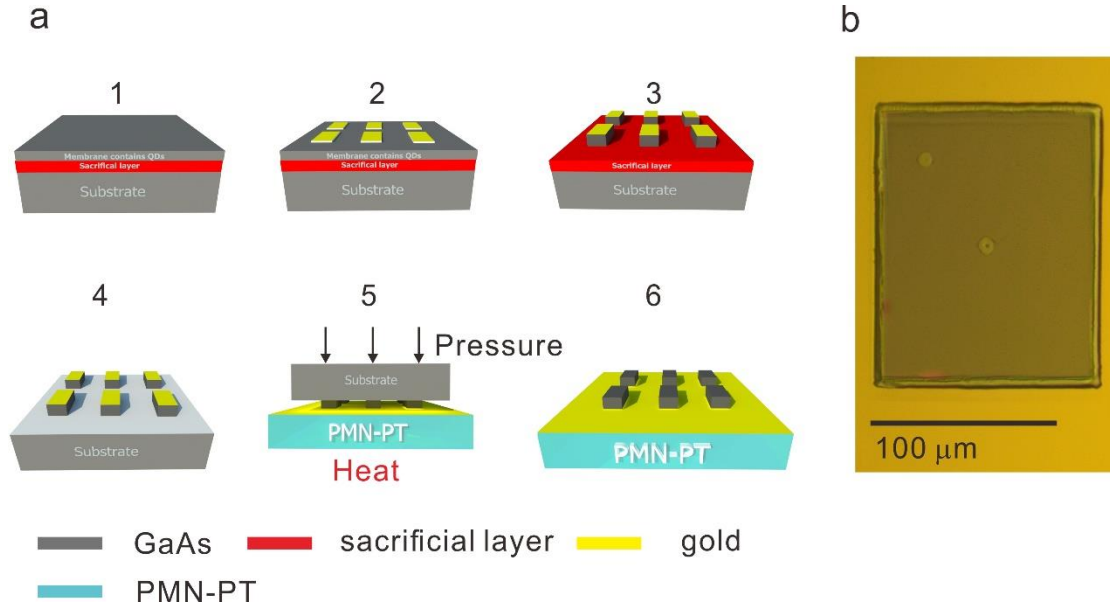
Fig. 3.2: (a) Schematic diagram of the whole fabrication process of a QDs-monolithic PMN-PT device. The process sequence is indicated by the number. (b) Microscope picture of a QD-membrane transferred to a gold-coated PMN-PT substrate.

Several impressive works have been accomplished on the strain tuning of QDs based on monolithic PMN-PT actuators, a brief overview will be given in this section with emphasis on two different bonding methods (polymer bonding and gold-to-gold bonding). The first work on QDs integrated on PMN-PT was performed with polymer bonding (PMMA)[43]. Polymer bonding has several advantages. First of all, relatively low operating temperature (150 ~ 200 °C) and low pressures (10 kPa) are needed, which is useful to prevent damage of the thin (~200 nm) membranes and also limit the occurrence of thermal stress during the cooling process. Secondly, Strain transfer efficiency via polymer bonding tends to be higher than for gold bonding[101]. The

remarkable strain transfer efficiency can be attributed to the wettability of the polymer when heated up during the bonding, which is also proved by the SEM cross selection images of GaAs bonded on a gold-coated PMN-PT actuator (Fig. 3.2 (a)): a thin and uniform bonding interface polymer (SU8 in this case) can be clearly observed. In contrast, air gaps can be clearly resolved in the gold-to-gold bonding interface (Fig. 3.3 (b)), which stem from residual roughness of the gold layers prior to bonding. Due to the uniform bonding interface obtained with polymer bonding, nearly isotropic biaxial strain can be transferred to the membranes.

The biaxial strain was found to be a powerful method not only to tune the emission energy of QDs, but also to adjust the energy separation between the photons emitted by InGaAs QDs during the biexciton cascade[41]. When the emission of exciton X goes into coincides with the biexciton XX, the QDs can act as entangled photon sources through a time reordering scheme[102].
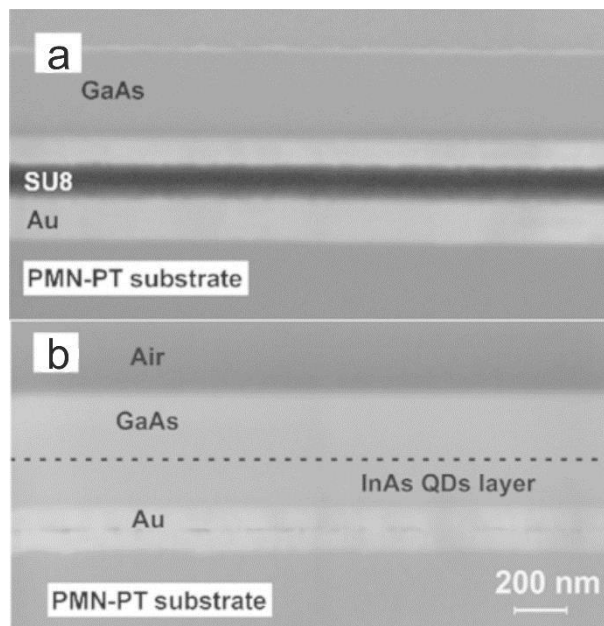
Fig 3.3: SEM picture of a cross-section of GaAs membrane bonded on gold-coated PMN-PT actuator with (a) polymer (SU8) bonding and (b) gold to gold bonding. Adapted from[103].

In spite of the fact that higher operating temperatures (250 ~ 300 °C) and higher pressures (~10 MPa) are needed for the gold thermocompression bonding[104], some irreplaceable advantages exist with this method. Firstly, the Cr/Au layer is a natural bottom electrode, which provides an additional tuning method for the optical properties of QDs. Secondly, the defective gold-to-gold bonding and associated strain anisotropies provides the possibility to eliminate the FSS in QDs. As discussed in Chapter 2, the FSS, which is attributed to the anisotropic electron-hole exchange interaction, is the main obstacle for QDs to being polarization-entangled-photon source, and isotropic biaxial strain cannot effectively modify the FSS[41]. However, FSS of QDs can be effectively adjusted via anisotropic strain field[44,105,106]. Trotta *et al.* showed that tunable anisotropic biaxial strain fields, combined with a tunable electric field obtained by embedding the QDs in the intrinsic region of a p-i-n diode, can be used as a tool to erase

the FSS in arbitrary QDs and that highly entangled photons can be generated in this way[47,107–109].

3.1.2 Novel micro-machined device and related processing

Although significant progress has been accomplished with strain-tunable devices consisting of QDs integrated with monolithic PMN-PT substrates, the limited strain provided by monolithic PMN-PT (~0.2%) and the poorly controllable strain configuration restrict the range of potential applications. One of the most desirable targets has been to restore the symmetry of a QD to act as polarization entangled photon source. Although this has been achieved by combining strain with electric fields, the energy of the resulting entangled photons is not tunable, which hinders the application of QDs in protocols involving several sources, such as entanglement swapping[31]. Inspired by the theoretical work that combined stresses can eliminate the FSS[45], Trotta el al. proposed a microstructured semiconductor-piezoelectric hybrid device (geometry shown in Fig. 3.4(a))[48]. Based on this concept, wavelength-tunable sources of entangled photons (with InAs QDs) were realized in 2016[50]. A schematic picture of the hybrid device and entanglement fidelity as a function of the time delay between the two emitted photons are shown in Fig. 3.4 (b), the center peak fidelity f exceeds the threshold for entanglement (0.5).

With the micro-machined PMN-PT actuator, arbitrary stress configuration can be produced by adjusting the electric fields applied to the fingers of the actuator[110].
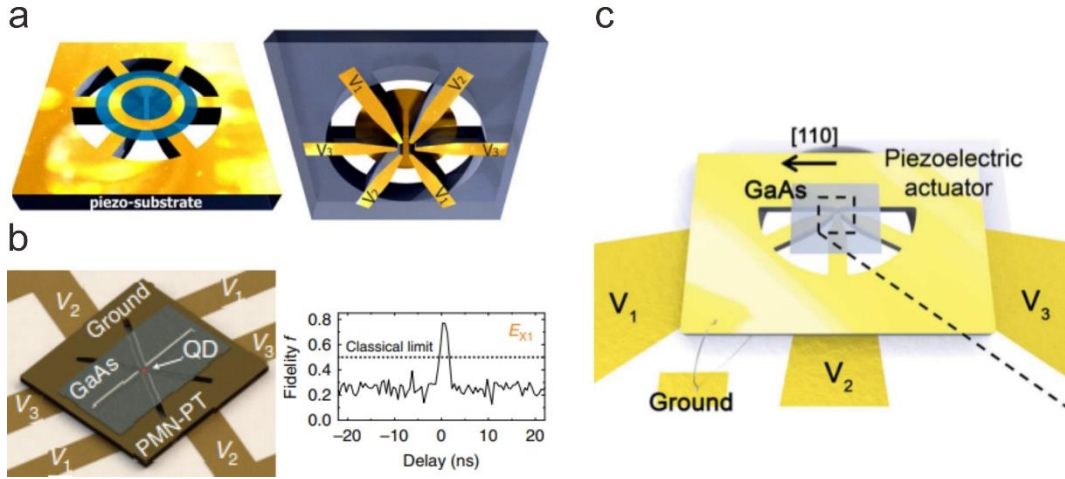
Fig. 3.4: (a) Sketch of a micro-machined PMN-PT actuator. With this novel PMN-PT actuator, three pairs of finger structures can provide three independent uniaxial stresses. The top and bottom sides of the PMN-PT actuator are coated with gold, as shown in the picture. Adapted from[48]. (b) The left panel is a sketch of the device which consists of a QD membrane bonded on a PMN-PT actuator. The right panel shows the entanglement fidelity as a function of time delay between photons when the FSS is canceled via stain engineering. Adapted from[50]. (c) Schematic representation of a three-fingers device with GaAs membrane bonded on top. Adapted from[110].

The PMN-PT actuator implemented and used in this work is also a micro-machined piezoelectric actuator. The micro-machined PMN-PT actuators are processed

as follows: 500 μm thick, (001) oriented PMN-PT substrates (TRS Technology) were first mechanically lapped and polished down to 300 μm, then the substrates were cut by a commercial 3D-Micromac laser system equipped with a femtosecond laser (by Dr. Giovanni Piredda, in Forschungszentrum Mikrotechnik, FH Vorarlberg, Dornbirn, Austria). The laser was focused down to a spot with 5 μm in diameter. After cleaning, the top side of the cut actuator was coated with Cr/Au (5/100 nm), which is electrically grounded. On the bottom side, the deposition area is limited only to the fingers' area, so that the electric-field-induced deformation is limited to the fingers. The geometry of the two-fingered PMN-PT actuator and metal deposition on the top and bottom side of the actuator are shown in Fig. 3.5. Furthermore, with this novel design, a "strain amplification" function is endowed: two fingers (l in length) are cut with a laser, a gap (d in length) exists between these two fingers, thus the strain in the gap can be amplified by the factor of $2l/d$. In this thesis we make the distance of the gap to be 50 μm (as shown in Fig. 3.5 (d)). Our simple actuator is thus capable of delivering strain values comparable to state-of-the-art microelectromechanical systems[111]. Moreover, Compared to the commonly used bending method[112,113], the actuator can be easily operated at cryogenic temperatures [here ~8 K for all measurements in this thesis] in a cold-finger cryostat.
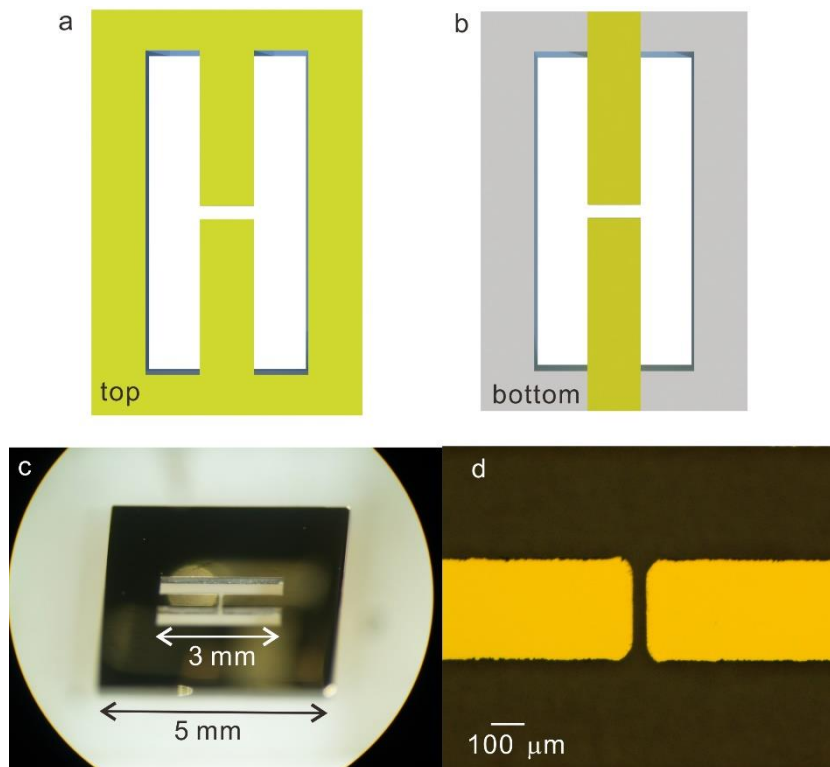

Fig. 3.5: Schematic picture of two-fingered PMN-PT actuator used in our work. Gold (marked in yellow) coated (a) top surface and (b) bottom surface of the micro-machined actuator. (c), Microscope image of the micro-machined "two fingers" PMN-PT actuator. (d), Enlarged microscope picture of the gap between the two fingers.

In this work, the GaAs sample is bonded to the PMN-PT actuator with SU8 bonding. After that, a "back etching" is used to remove the GaAs substrate and only leave the QD-membranes bonded on the piezoelectric actuators. The reason is that the stress exerted by the PMN-PT is limited and the maximum achievable strain in the semiconductor drops with the stiffness of the structure, i.e. with its thickness. The flow diagram of the process is shown in Fig. 3.6 and the process details are as follows: First, standard UV photolithography is performed on the sample, followed by Cr/Au (3/100 nm) deposition and lift-off. After that, using the metal layer as mask, the sample is immersed into piranha solution (H_2SO_4 : H_2O_2 : H_2O = 1: 8: 200 in volume) until the etching reaches the sacrificial layer. Before the bonding, SU8 photoresist (2000.5, MicroChem) is spin-coated (1000 rpm/s for 10s followed by 4000 rpm/s for 30s) on the surface of PMN-PT actuator, followed by a soft-bake (65 ° C for 5 minutes and 90 ° C for 5 minutes) to evaporate the solvents from the photoresist. Then, with a flip-chip method (pressure and heating can be simultaneously applied), the sample is bonded onto the PMN-PT actuator. During the bonding, the pressing force is kept at 15 N and the heating temperature is maintained at 250 ° C for 15 minutes to hard-bake the SU8 photoresist. After the bonding, a "back etching" method is employed to remove the GaAs substrate. A mixed solution of orthophosphoric acid (H_3PO_4, 85% in concentration) and hydrogen peroxide (H_2O_2, 30% in concentration) (3:7 in volume) is used to make a non-selective etching to remove most of the GaAs substrate[114]. Then a selective etching is performed with citric acid (30% in concentration) and hydrogen peroxide (H_2O_2, 30% in concentration) (4:1 in volume) to remove the remaining GaAs substrate. Lastly, we remove the sacrificial layer ($Al_{0.75}Ga_{0.25}As$) with diluted hydrofluoric acid (HF) (10% in concentration), leaving only the QD-membranes bonded on the piezoelectric actuator. The performance and mechanism of the QDs-micro-machined PMN-PT device will be discussed in detail in Chapter 4.
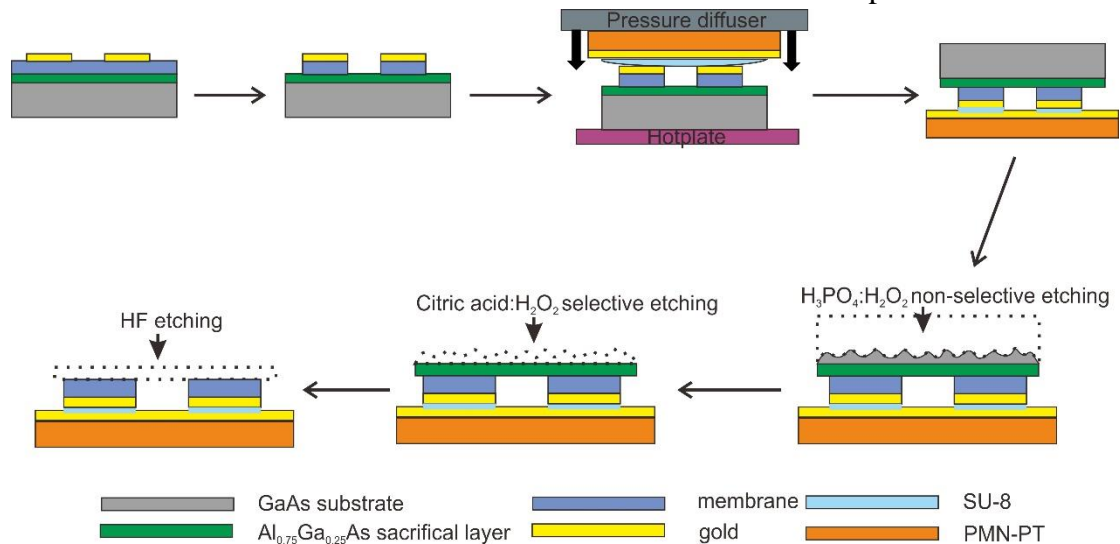

Fig. 3.6: Flow diagram of the whole fabrication process of bonding a QD-membrane on a two- fingered PMN-PT actuator.

3.2 Tuning QDs with SAWs

As discussed in the previous section, SAWs are phononic technologies widely used not only in consumer electronics but also in frontier research. Works on the interaction between SAWs and QDs include picking up an electron from one QD to another ("quantum ping-pong") to achieve quantum information transfer[115], resolved sideband emission[116], charge injection into QDs[117,118], and the use of QDs to probe engineered shaped strain pulses[119].

Based on the strong interaction between QDs (and other solid-state systems) and strain fields, it is tempting to draw analogies with electromagnetic fields and quantum optics and to think about phonons taking the place of photons in quantum phononic devices [120]. However, it is still a long way to reach this final target, and several efforts need to be paid to study the physics underlying the interaction of QDs and sound under different circumstances. Fig. 3.7 (a) schematically shows the device studied in the work. Interdigital transducers (IDTs) are fabricated with Electron-beam lithography (EBL), metal deposition (Cr/Au 5/50 nm) and lift off. Usually, the IDT1 is connected to a function generator, to generate SAWs. The sound waves will travel the surface and will be converted to electrical signals when they reach IDT2, the IDT2 is usually connected to an oscilloscope for detection. These two identical IDT pairs constitute a delay line, which allows an estimation of the transmitted acoustic power and speed. The sample we used contains three different layers: a GaAs substrate, the sacrificial layer, and an active layer with embedded QDs. With this structure, not only the properties of Rayleigh waves can be studied, but also propagation in more complex structures (waveguide, phononic crystal), see Chapter 6.

The optomechanical coupling between GaAs QDs and the deformation arising from SAWs is schematically shown in Fig. 3.7 (b). For QDs, the exciton transition energy can be treated as a two-level system. During the propagation of SAWs, the transition energy of QDs will be modified by the deformation potential caused by the pressure associated with SAWs. Thus, through the detection of the dynamic shift of the photoluminescence (PL) spectrum of each individual QD, the SAWs waveform can be determined. In other words, with the effective optomechanical coupling, we take the potential of QDs to sense the nanomechanical signals and convert them to the optical domain.
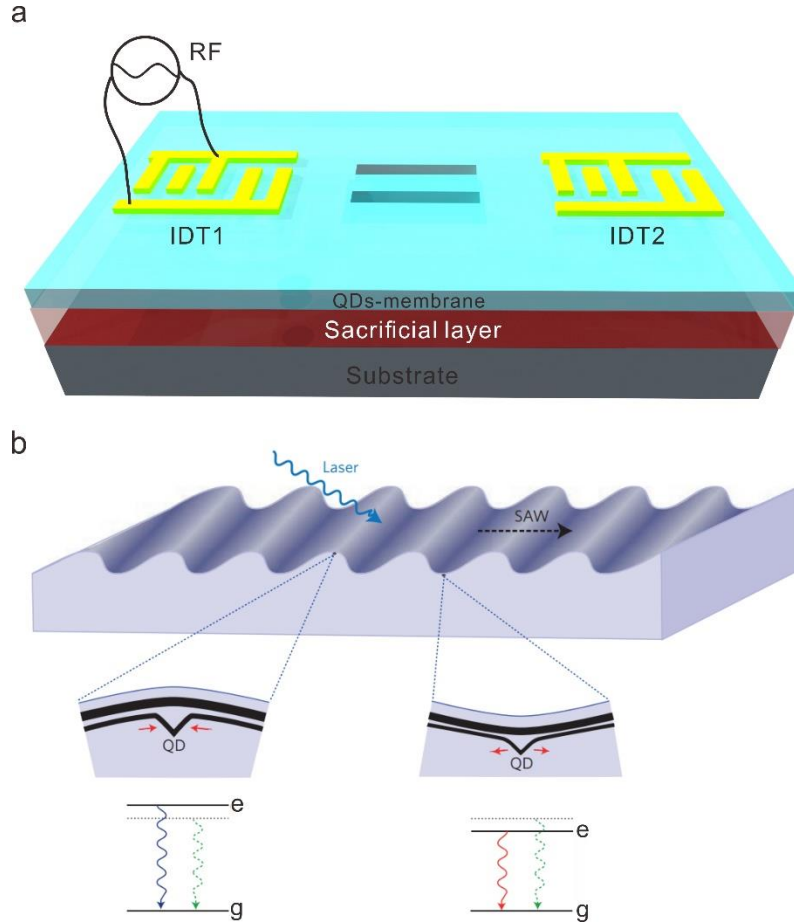
Fig. 3.7: (a) Schematic picture of the device used in our work. Comb-like IDTs are connected to a radiofrequency (RF) function generator, which allows SAWs to be generated. (b) Schematic diagram of the optomechanical interaction between the deformation caused by SAWs and single embedded quantum dots (QDs) in a semiconductor heterostructure. Adapted from [121].

3.3 Experimental setup

In our work, micro-photoluminescence (μ-PL) is the main characterization method to study the optical and electronic properties of QDs-based devices. In our work, the QDs are excited with lasers, which provide photons with higher energy than the bandgap of the barrier (non-resonant excitation, schematically shown in Fig. 2.2). Once the photons are absorbed, holes and electrons are formed in valence band and conduction band with finite momenta. Following relaxation, the electrons will recombine with holes and emit responding photons, which we detect with a spectrometer equipped with a CCD camera.

Base on the manipulation methods (strain from PMN-PT actuator and SAWs), the main work in this thesis can be divided into two sets of experiments, which were performed at the Johannes Kepler Universität (JKU), Linz and Universität Augsburg, respectively. The experimental setup is quite similar on the optical side. Fig. 3.8 shows schematically the experimental setup at JKU. The sample is mounted on the cold finger of a helium-flow cryostat, with which the temperature can vary between 4 K and 300

K. In all experiments, the temperature is kept below 10 K during the measurement to reduce phonon broadening of the emission lines of the QDs. The whole cryostat sits on a motorized x-y stage, which allows motion with minimum step sizes of about 50 nm. Sourcemeters (ISEG, high voltage power supply, and R&S HMF 2550, arbitrary function generator) are connected to the cryostat to modulate the PMN-PT actuators. A diode pumped solid state laser (Millenia from Spectra Physics), which emits photons at the wavelength of 532 nm, is employed as the non-resonant excitation source. Firstly, the laser impinges onto a 50:50 beam splitter: half of the laser power is detected with a power meter, the other half passes a second beam splitter and then is focused with a $50\times$ objective (numerical aperture: 0.42) to the sample. The objective is mounted on a single axis piezoelectric actuator, which allows the distance between objective and sample to be precisely adjusted. The excited signal from the sample is collected with the same objective, reflected by the beam splitter and then passes a half-wave plate ($\lambda/2$) and a linear polarizer. The half waveplate is mounted in a computer-controlled rotary stage with a precision of 0.1°. The combination of rotating half wave plate ($\lambda/2$) and linear polarizer allows us to collect linear polarization resolved spectra of the signal emitted from our QDs, which is a very important method to observe the exciton evolutions under strain (see Chapter 4). Then a long pass filter (transparent for wavelengths above 650 nm) is used to remove the laser, which is reflected by the sample. Lastly, the signal is focused on the entrance slit of a spectrometer with 750 mm focal length equipped with various gratings. The diffracted signal is then focused on a nitrogen-cooled Si CCD (for spectral analysis) or on an avalanche photodiode (APD) (for time-resolved measurements).
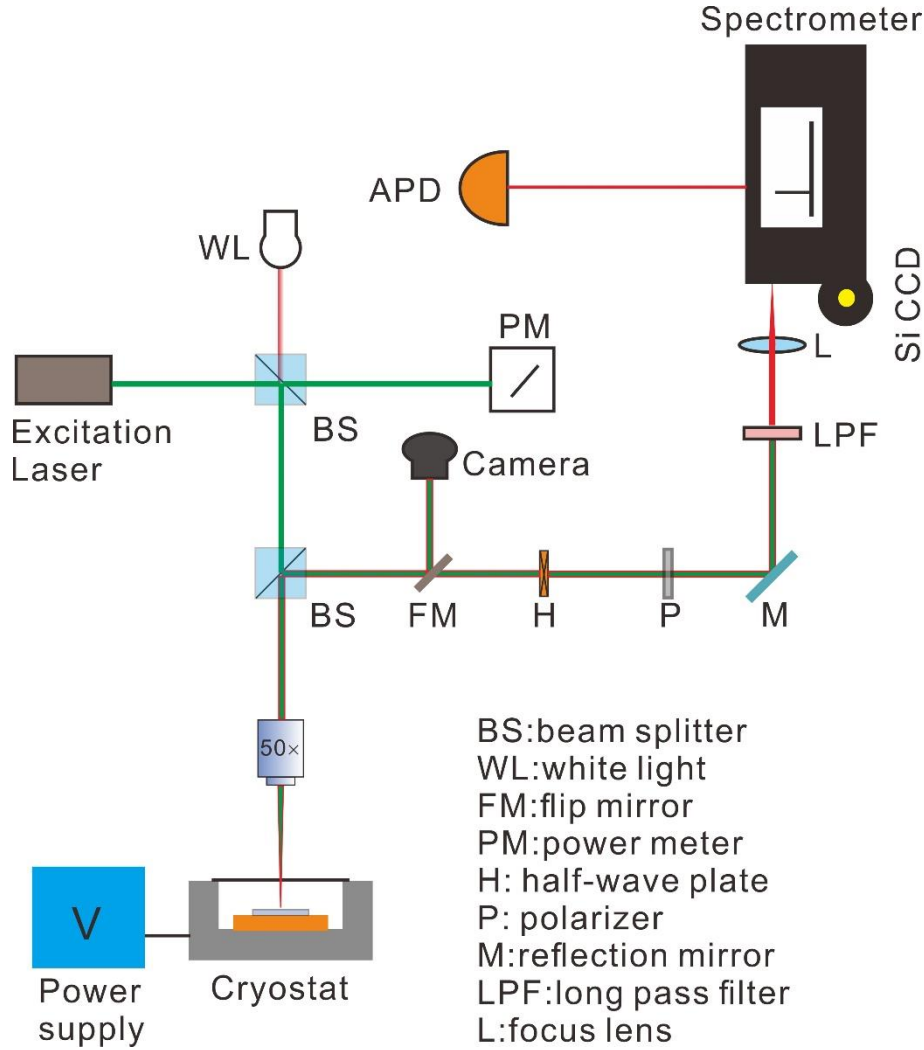
Fig. 3.8: Schematic picture of the micro-PL experimental setup at JKU, Linz.

One of the important measurements what we can perform with this setup is polarization-resolved PL spectroscopy. With polarization-resolved PL spectra, several useful characteristics (such as FSS, degree of linear polarization, polarization orientation) of QDs can be obtained. Here we just describe the fitting procedure for the FSS. Figure 3.9 (a) shows polarization resolved PL spectra of a neutral exciton confined in a QD. Since the photons emitted the QDs stem from a spontaneous emission, a Gaussian function can be employed to obtain the peak positions for each polarization angle, as illustrated in Figure 3.9 (b). Then we plot these peak positions with relevant polarization angles in Figure 3.9 (c). By applying a cosinusoidal fit, the FSS value can be estimated as twice the amplitude of the cosinusoidal function.
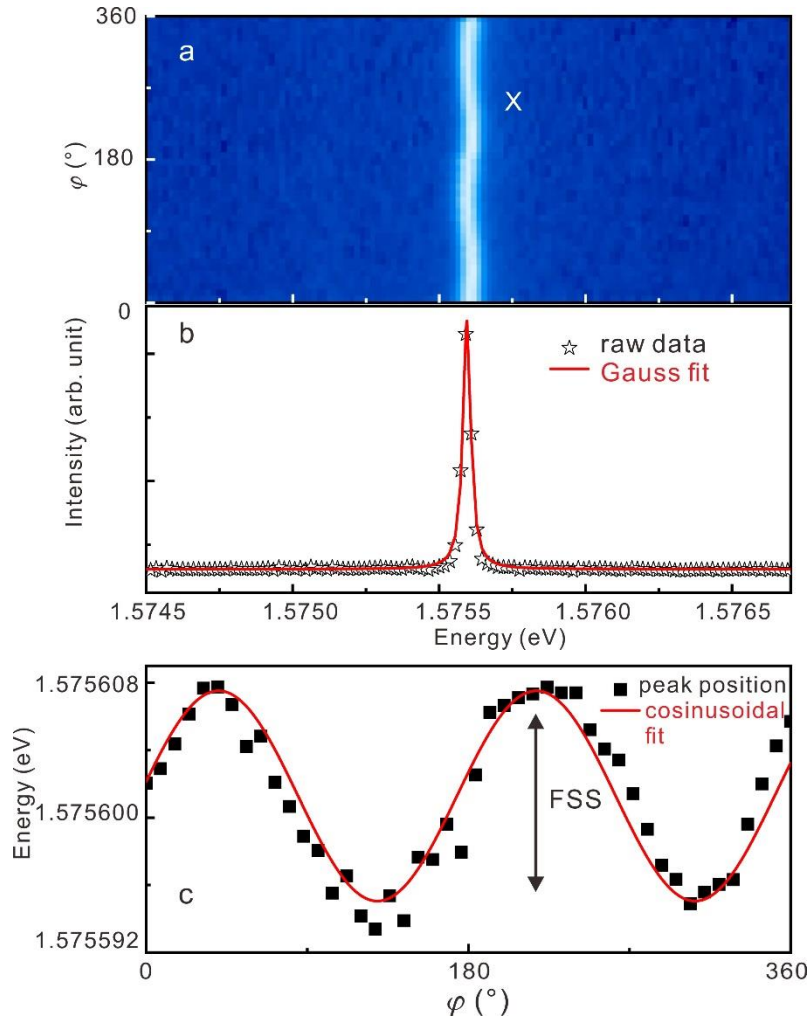
Fig. 3.9: (a) Polarization resolved PL spectra of the neutral exciton (labelled as X) from a GaAs QD. (b) A PL spectrum of the neutral exciton at a given polarization angle. The raw data from the spectrometer is plot with stars, with a Gaussian fitting as a red line. (c) The obtained emission energy (peak position) are plotted as a function of polarization angle, with cosinusoidal function fit (red line) to get the FSS value.

3.4 FEM simulation using COMSOL Multiphysics

The finite element method (FEM) is a common method for solving problems in physics and engineering. These problems (like structural analysis, heat transfer, electromagnetic problems) always follow space and/or time-independent laws, which are usually expressed through *partial differential equations* (PDEs). For the majority of problems (especially for objects with irregular geometries), it will not be possible to find analytic solutions. The basic concept of FEM can be summarized as follows: first, dividing the domains of problems into a collection of subdomains, with each subdomains represented by sets of equations to the origin problems; then recombine all sets of elements equations into the whole domain of equation for final solutions. Usually the global system of equations has known solution techniques, which can be

calculated by the initial value and relevant boundary conditions. With the FEM method one can define the mesh of the object according to the required precision and computing power.

In our work, COMSOL Multiphysics (5.3) is employed to simulate the stress (strain), displacement, and electric field distribution in our device due to its relatively user-friendly characteristics and capability of treating coupled physical phenomena. In the following part, we will give a brief introduction to the main idea of the simulation in COMSOL Multiphysics in our work.

To simulate the strain (stress) distribution in the QD membranes of the hybrid device, a simplified 3D model based on our device is constructed, as shown in Fig. 3.10 (a). For saving computational resources during the simulation, the whole structure is simplified as shown in the following. The elements 1 and 2 are the chip carrier; the bottom side of these elements is set as fixed constraints. Elements 3 and 4 are made of PMN-PT[v]; their top side is set as ground and certain electric potentials are set on the bottom side, as in the experiment. Element 5 is the GaAs membrane, with 100 nm SU8 photoresist (not visible in the drawing) sandwiched between 5 and 3, 4. Fig. 3.10 (b) shows the zoom-in view of the membrane located on the gap between the fingers of the PMN-PT actuator, w is the width of membrane and d is the distance between of the fingers, which we can set based on the real device. Here an "Adaptive Mesh Refinement" [122] is adopted, characterized by a finer mesh at the regions where strong gradients are expected (like the boundary between objects), and the area of interest (the membrane), as shown in Fig. 3.10 (c). We should mention that in the simulation we used the elastic and piezoelectric parameters of PMN-PT at room temperature. Since it is known that the piezoelectric constants of PMN-PT will decrease at cryogenic temperature[100], we adjusted the electric field applied to the PMN-PT to obtain strain magnitudes similar to our experiment. In the next chapter, results obtained with this device will be shown.

---

[v] Piezoelectric parameters at RT are obtained from TRS Technology, which can be found in Appendix A.1.
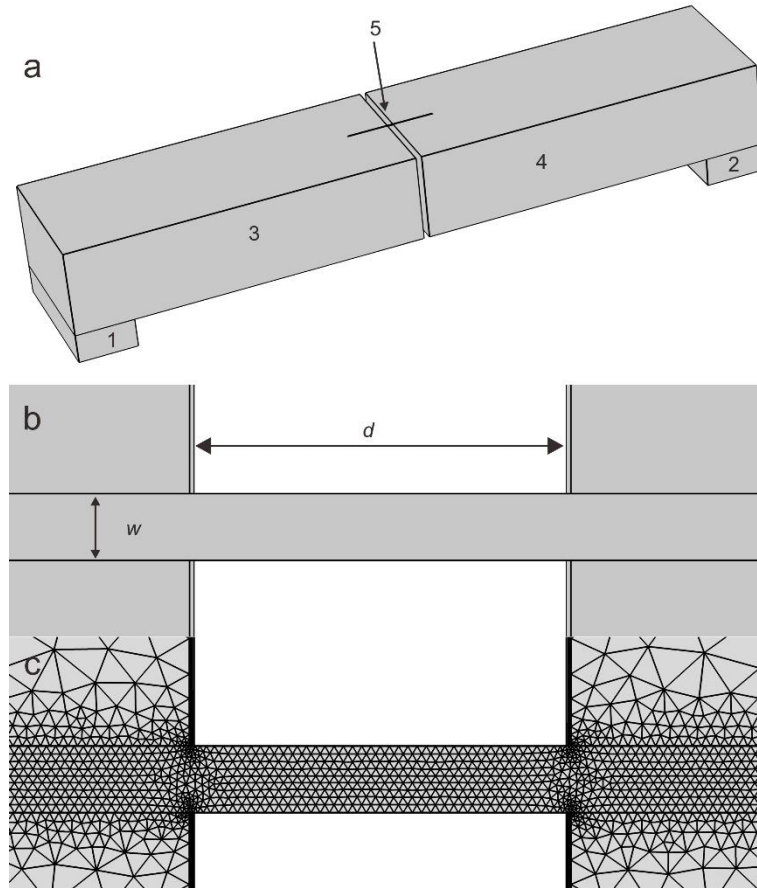
Fig. 3.10: (a) Sketch of the simplified structure of QDs-micro-machined PMN-PT actuator hybrid device simulated with COMSOL Multiphysics. (b) Zoom-in view of the membrane at the gap between the fingers of the PMN-PT actuator. *w* stands for the width of the membrane and *d* is the distance between the fingers. (c) Mesh used for FEM computation.

Although in the previous chapter we gave a comprehensive introduction on the propagation of SAWs in solids and in principle it is possible to give an analytical solution based on that, it would be too complicated to apply the theory for a realistic structure. For instance, the phase velocity of SAWs is only determined by the elastic constant of the specific material. However, our sample consists of several layers, which possess different elastic parameters, in that case, the velocity could be dispersive to frequency. In addition, the QDs are buried into the sample and it would be desirable to obtain the strain and electric field arising from SAWs directly. For this reason we performed 2D FEM simulations. Fig. 3.11 (a) is the overview of the structure cell of the sample imported in COMSOL. The width of the structure is set as one wavelength (λ_0) of the SAW, the thickness is set as three times of the wavelength of the SAW ($3\lambda_0$) since the SAW is confined close to the surface of the sample. The bottom line 4 is treated as a fixed constraint. The boundary lines 1 and 3 are periodical and phase antisymmetric to the middle line 2. The structure of the membrane is simplified as shown in Fig. 3.11 (b), the QDs are omitted and only 2 nm GaAs layer is left. Form the set of solutions provided by COMSOL, we can select the desired solutions. More results based on the simulations will be shown in Chapter 6.

Fig. 3.11: (a) Schematic structure of the sample (AS 275) used in COMSOL Multiphysics to simulate the Rayleigh waves. The width is defined as the wavelength λ_0 and the whole thickness of the sample is set as three times wavelength $3\lambda_0$. (b) An enlarged view of the active layer containing QDs.
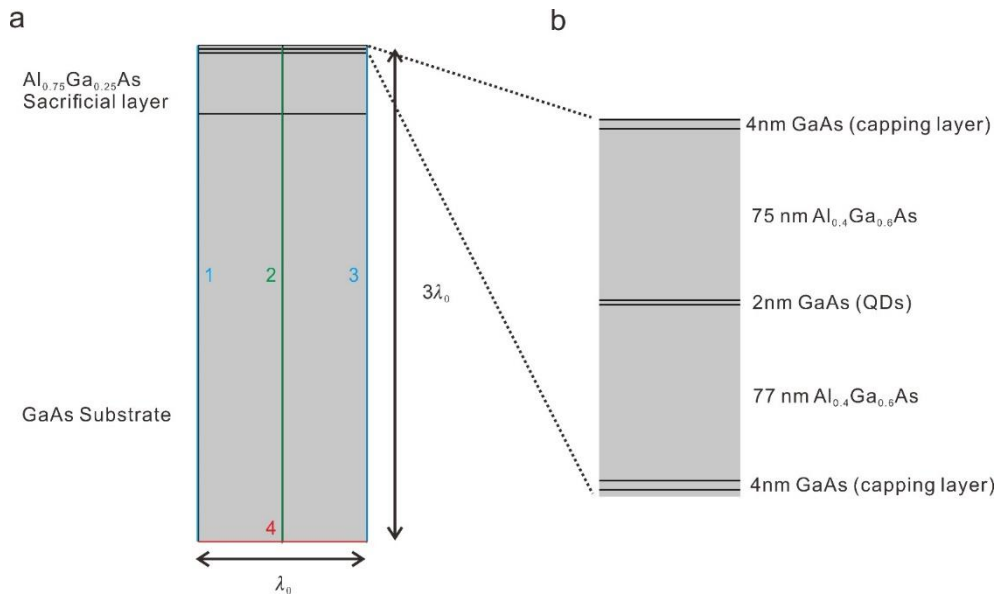
4. Uniaxial stress flips the natural quantization axis of a quantum dot for integrated quantum photonics[VI]

The selection rules of optical transitions in epitaxial quantum dots are determined to a large extent by the orientation of their quantization axis, which is usually parallel to the growth direction. This configuration is well suited for vertically emitting quantum devices, but not ideal for planar photonic circuits. In this chapter, we show that the quantization axis of a GaAs quantum dot can be turned to lie in the growth plane via uniaxial elastic stress. This rotation, which is accomplished through a complex evolution of the confined hole wave function, is possible whenever confinement can be viewed as a perturbation compared to the strain-induced effects. The experimental and computational results suggest that uniaxial stress – already employed for enhancing the performance of integrated electronic circuits – may be the right strategy to obtain quantum-light sources with ideally oriented transition dipoles and enhanced oscillator strengths for integrated quantum photonic circuits.

4.1 Motivation

Epitaxial QDs usually possess flat morphologies [schematically shown in Fig. 4.1(a)], and heights comparable to the Bohr-radius of the confined excitons. Carriers are therefore strongly confined along the growth (z) direction, which also represents the natural quantization axis[123–125]. The vertical confinement [and possibly in-plane compressive strain naturally present in QDs obtained by the Stranski-Krastanow growth mode] splits the heavy-hole (HH) and light-hole (LH) bands, so that the HGS has dominant HH_z character, with total angular momentum projection $J_z=\pm 3/2$ (in units of ħ). Dipole-allowed transitions involving such states are characterized by transition-dipoles perpendicular to z, making them well suited for efficient vertically-emitting single-photon devices[12,58,126–129] (as shown in Fig. 4.1 (a)). However, if we consider the planar integrated quantum photonics applications, it would be instead desirable to have QDs with transition dipoles perpendicular to the propagation direction, and hence a quantization axis in the x-y plane.

In spite of their importance, very little effort has been devoted to developing quantum sources optimized for planar photonic circuits. An exception is represented by Ref[130]. In this work, the quantization axis is rotated by 90 ° via a simple way: the QDs, embedded in nanowires, are removed from the substrate, and then integrated into a silicon-nitride waveguide for efficient coupling, as shown in Fig 4. 1(b). Although an in-plane oriented quantization axis is realized with this method, it still remains a time-

---

[VI] The main results in this chapter are published in *Nat. Commun.* **9,** 3058 (2018) and *Semiconductor Science and Technology* **33**, 013301 (2018).

consuming approach when we consider further potential large-scale integrated on-chip applications.

The question we addressed here is: Is there a gentler way, which allows obtaining an in-plane quantization axis while preserving the compatibility of the QD heterostructure with planar photonic processing? Inspired by predecessors' experience in our group, stress (or strain) could be a means for that. However, there are two main issues to be addressed if we want to obtain an in-plane quantization via stress (or strain). Firstly, different from most previous work of strain tuning on QDs, uniaxial stress with relatively large magnitude should be applied, so that confinement can be seen as a perturbation compared to strain-induced effects. Secondly, high quality and nearly strain-free GaAs QDs[29,131] should be used, which could maximize the effect of externally induced strain.
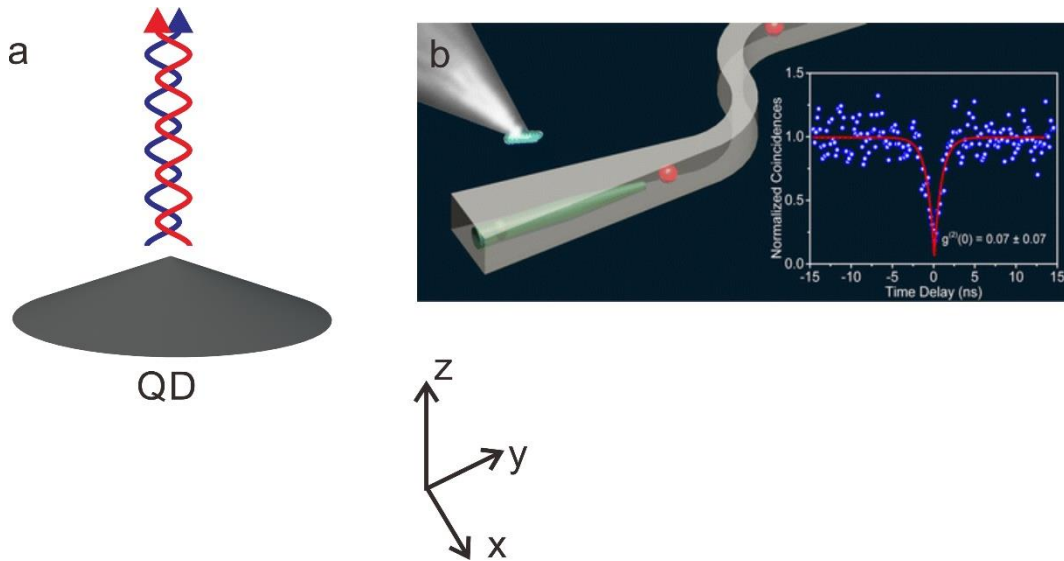
Fig. 4.1: (a) Sketch of the common "flat" QD with quantization axis along the z-direction, two bright eigenstates lead to photons polarized in the *x-y* plane, which is suitable for vertically coupling. (b) Schematic picture of a device with QDs featuring an in-plane quantization axis. The QDs in nanowires are embedded in SiN waveguides, red spheres stand for the emitted photons. The inset shows the second-order correlation properties from the emission of a QD. Adapted from [130].

4.2 Illustration of concept

A general view of the physics of the problem of a QD under uniaxial stress can be gained by inspecting the effect of stress on bulk GaAs, which is reasonable because our GaAs QDs are initially almost unstrained and have a relatively large height [see atomic force microscopy (AFM) image in Fig. 4.2 (a)], resulting in a "gentle" perturbation of the bulk crystal symmetry and providing the possibility of reorienting the relatively "soft" quantization axis with moderate strains. As mentioned above, the hole ground state of epitaxial QDs has dominant HH_z character as a consequence of the vertical confinement. The same situation is encountered when biaxial compression in the *x-y* plane is applied to bulk GaAs. In these cases, the angular dependence of the HH_z

Bloch wavefunction shows a "donut" shape (see inset in Fig. 4.2 (b)). Combined with the s-like electron Bloch-wavefunction, such a state couples only to light with polarization perpendicular to the z quantization axis. Obviously, for bulk GaAs, the quantization axis could be set to the [100] (x) direction by simply applying a biaxial stress in the y-z plane or uniaxial stress along the x-direction. Now the question is: is it possible to rotate the quantization axis of a QD through the same approach and with realistic values of stress? Previous experiments have shown that breaking the symmetry in the x-y plane results in substantial HH_z - LH_z hole-mixing[132,133], but the possibility of reaching pure HH_x or LH_x states has not been discussed so far. And in fact the answer would be negative for conventional Stranski-Krastanow QDs because vertical confinement and in-plane compression (of the order of GPa) "team up" to stabilize a vertically-oriented quantization axis. Initially unstrained GaAs QDs with relatively weak confinement energies are instead ideally suited to address the question.

To quantify to what extent the quantization axis is oriented along the original z direction or the desired x direction under uniaxial stress, the hole ground state was calculated for our QDs (Fig. 4.2 (a)) via the empirical pseudopotential method (EPM). The projection of this state onto the HH, LH, and SO (split-off) states using either the z- or the x-quantization axis is shown with symbols in Fig. 4.2 (b), (c) respectively. (Calculation were performed by Fritz Weyhausen-Brinkmann and Prof. Dr. Gabriel Bester at the Universität Hamburg).

Using the conventional quantization axis z [Fig. 4.2 (b)] we would reach the wrong conclusion that uniaxial stress results in strong HH-LH mixing even for large strains. By using instead the new quantization axis x, we see that the topmost VB has almost pure HH_x character (with some LH_x admixture) upon sufficiently strong tension and almost pure LH_x character (with some SO_x admixture) upon compression [Fig. 4.2 (c)]. Remarkably, the EPM calculations predict that *the "swapping" of quantization axis occurs already at moderate strains*: the hole ground state of our QDs should have >90% HH_x character for strains $\varepsilon_{xx} \gtrsim 0.3\%$ and >90% LH_x character for $\varepsilon_{xx} \lesssim -0.1\%$. This result crucially relies on the use of tall and initially unstrained QDs and could not be achieved with conventional Stranski-Krastanow QDs. The predicted evolution of the hole ground state upon uniaxial stress is robust and can be even caught with a simple model of bulk GaAs subject to a fixed biaxial stress in the x-y plane and variable uniaxial stress along the x direction, as shown by the curves in Figs. 4.2 (b) and (c). Under tension we expect a donut-shaped Bloch wavefunction (right inset in Fig. 4.2 (c)), an ideal configuration for light-coupling into an x-oriented waveguide. Under compression the wavefunction has instead a dumbbell shape elongated along the x-direction. This configuration is well suited for coupling into y-oriented waveguides.
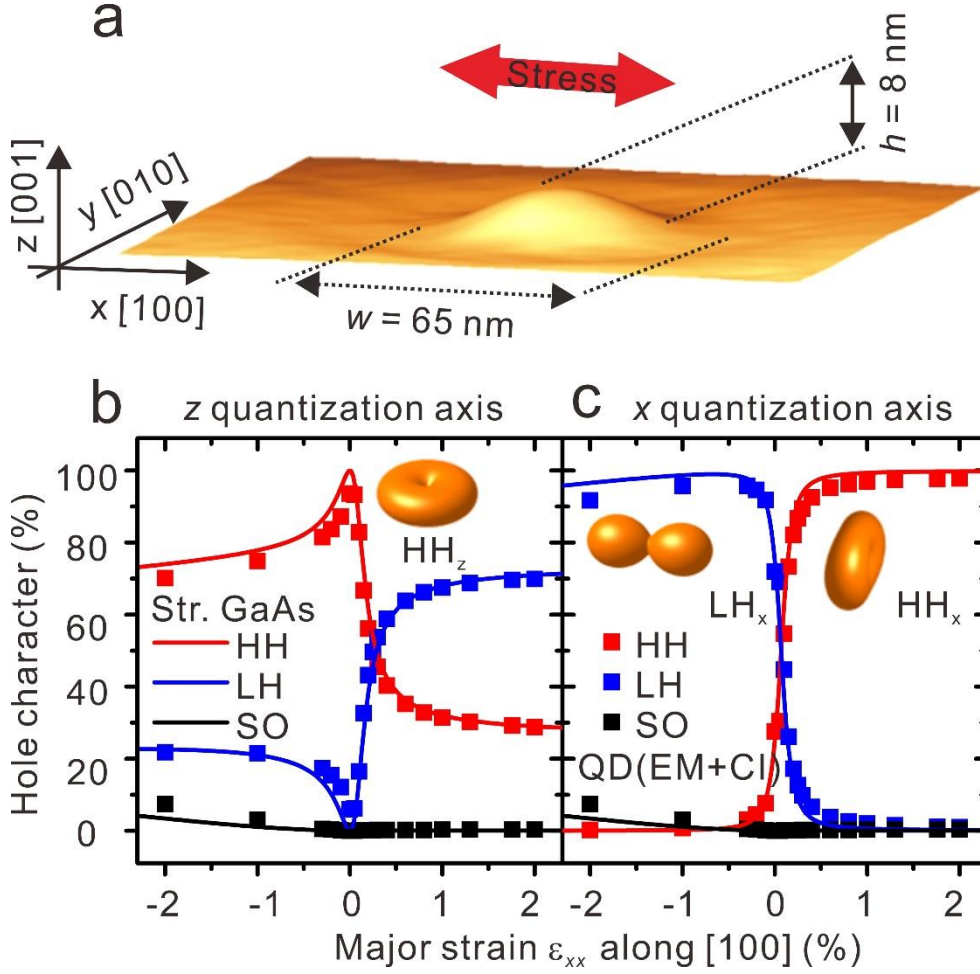
Fig. 4.2: Illustration of the concept used to rotate the quantization axis of an epitaxial QD. (a), 3D view of an AFM image of a GaAs QD embedded in AlGaAs matrix subject to uniaxial stress. (b), (c), the calculated effect of uniaxial stress on the degree of mixing of the topmost VB using the *z* and *x* quantization axis, for bulk GaAs subject to a fixed in-plane biaxial compression with $\sigma_{xx}=\sigma_{yy}=-120$ MPa (solid curves) and for the experimentally studied QDs (symbols). The plots illustrate the importance of the choice of the quantization axis when discussing VB mixing and show that the quantization axis of the chosen QDs can be rotated with moderate strains. Insets: Angular dependence of the probability density distribution of the Bloch wavefunctions of the topmost VB states at the Γ point showing the conversion of a HH_z state into a HH_x (LH_x) state under tension (compression).

In our experiment, large enough uniaxial stress can be provided that we can neglect the confinement effects. Since the spin-orbit coupling-constant Δ is relatively large, we can just focus on the topmost 4 bands, so the 4×4 block of the Hamiltonian can be written as:

$$H_{4\times 4} = -\begin{pmatrix} P+Q & -S & R & 0 \\ -S^+ & P-Q & 0 & R \\ R^+ & 0 & P-Q & S \\ 0 & R^+ & S^+ & P+Q \end{pmatrix} \tag{4.1}$$

Considering the strain configuration for uniaxial stress, $\varepsilon_{yy} = \varepsilon_{zz} = -\frac{C_{12}}{C_{11}+C_{12}}\varepsilon_{xx} = -\nu_{[100]}\varepsilon_{xx}$, S is zero (since there is no shear stress), the Hamiltonian for the relevant valence bands evolves into

$$H_U = -\begin{pmatrix} P+Q & 0 & R & 0 \\ 0 & P-Q & 0 & R \\ R^+ & 0 & P-Q & 0 \\ 0 & R^+ & 0 & P+Q \end{pmatrix} \tag{4.2}$$

The operator for the component x of the total angular moment is given by:

$$\hat{J}_x = \hbar\begin{pmatrix} 0 & \frac{\sqrt{3}}{2} & 0 & 0 \\ \frac{\sqrt{3}}{2} & 0 & 1 & 0 \\ 0 & 1 & 0 & \frac{\sqrt{3}}{2} \\ 0 & 0 & \frac{\sqrt{3}}{2} & 0 \end{pmatrix} \tag{4.3}$$

Now $[\hat{J}_x, H_{4\times4}]=0$, i.e. that the quantization axis is parallel to the x axis. So we can conclude that under large uniaxial stress the quantization axis is along x direction.
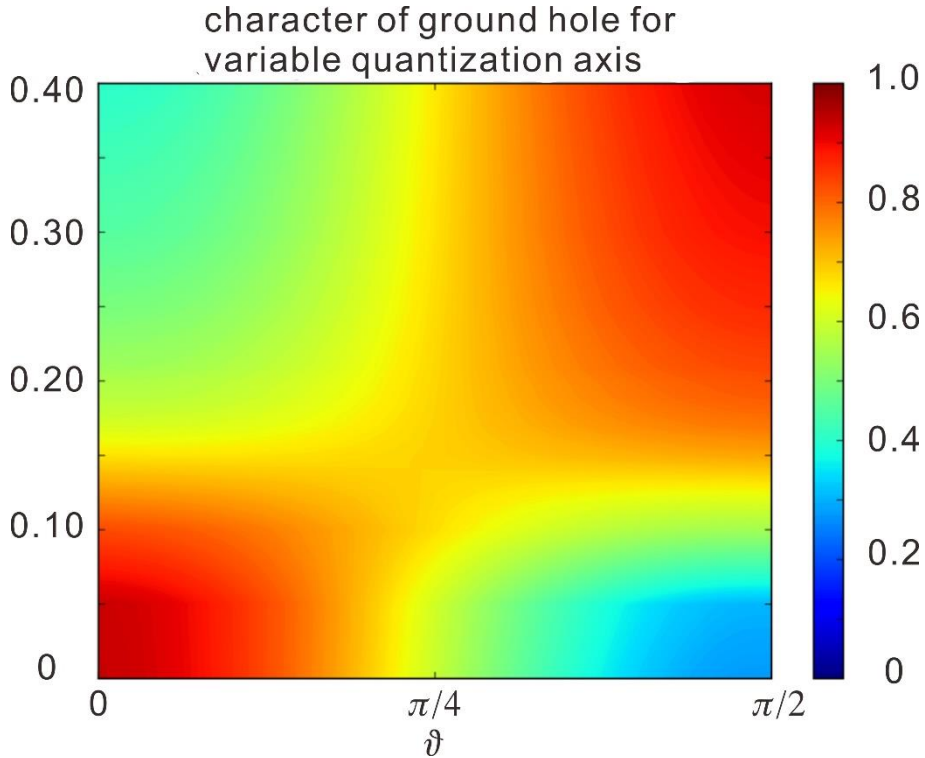

Fig. 4.3: Value of the projection of the HGS on the HH$_n$ state for different values of strain. Large values of the projection indicate that it is meaningful to define a quantization axis along the direction specified by the unit vector **n**=(cosϑ, 0, sinϑ) in the x-z plane (ϑ=0 corresponds to the z-axis while ϑ=π/2

corresponds to the x-axis).

Before presenting the experimental results we wish to further clarify that a natural quantization axis for the holes angular momentum can be defined in absence of strain and for sufficiently large strain. With EPM+CI method the hole-ground-state (HGS) was calculated as a function of stress and projected to the eigenstates of the angular momentum projection operator $\mathbf{J_n}$ (with $\mathbf{n}=(\cos\vartheta, 0, \sin\vartheta)$ in x-z plane). The result for the projection $|\langle HGS|HH_n\rangle|^2$ is graphically shown in Fig. 4.3. Large values of the projection – let's say above 0.9 (a typical value of $|\langle HGS|HH_z\rangle|^2$ for conventional Stranski-Krastanow QDs) can be interpreted as the indication that it is meaningful to define a quantization axis along the direction specified by $\mathbf{n}$. Low values indicate instead mixed HH-LH states, for which the total angular momentum is not well defined. The plot clearly shows that a z quantization axis is appropriate for our as-grown QDs, while the quantization axis is oriented along the x direction for large values of strain). The data shown in red in Fig. 4.2(b) and (c) correspond to vertical scans for $\vartheta=0$ (z-axis) and $\vartheta=\pi/2$ (x-axis), respectively.

4.3 QDs-PMN-PT-actuator device: fabrication and performance

Through the theoretical analysis of the former section, we found that in principle it is feasible to rotate the quantization axis of QDs by 90°. To test this prediction, we have developed and used a novel micromachined piezoelectric actuator, already introduced in Sec. 3.1.2. The main reason is that the maximum strain achievable with monolithic actuators at cryogenic temperature is of the order of 0.2%, which is barely sufficient to achieve the desired rotation of the quantization axis.

In this work, strain-free GaAs QDs are used, which we expect to be more tunable than conventional strained QDs under strain. Most of the samples used in this Chapter were grown by Dr. Yongheng Huo at IFW, Dresden, and some samples (with the same droplet etching method) grown by Dr. Saimon Filipe Covre da Silva at JKU, Linz are also used. Here we just present a description of the sample from IFW Dresden.

The sample was grown by solid-source molecular epitaxy (MBE) on semi-insulating GaAs (001) substrate. After oxide desorption, a 200 nm thick GaAs buffer was grown. Then a 100 nm thick $Al_{0.75}Ga_{0.25}As$ sacrificial layer was deposited, followed by 5 nm GaAs, which was used to smoothen the surface and avoid oxidation of the membranes after releasing them from the substrate. Subsequently, 90 nm $Al_{0.2}Ga_{0.8}As$ and 30 nm $Al_{0.4}Ga_{0.6}As$ layers were deposited in sequence. Later the GaAs QDs formed with the droplet etching method. The QDs were capped with 30 nm $Al_{0.4}Ga_{0.6}As$ layer, followed by 90 nm $Al_{0.2}Ga_{0.8}As$ layer. Finally, a 5 nm GaAs completes the growth. The whole structure of the as-grown sample is shown in Figure 4.4.
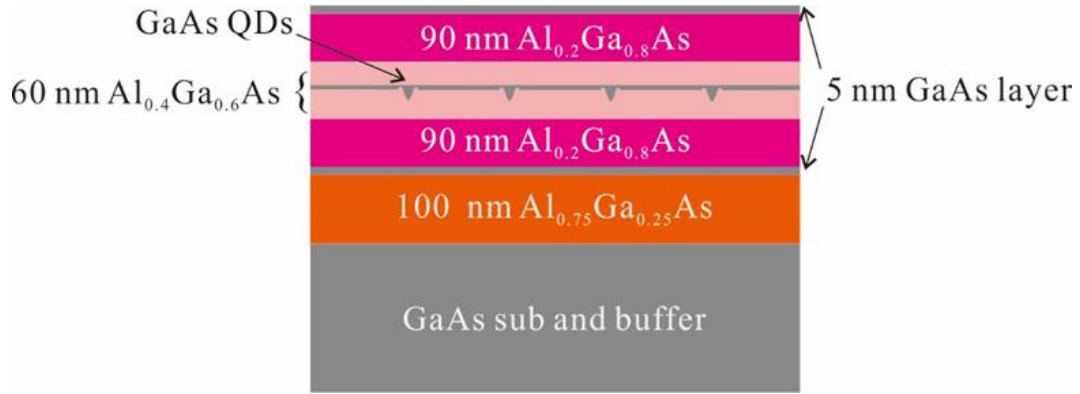
Fig. 4.4: Structure of the GaAs QDs sample used in this work.

The detailed device processing information can be found in section 3.1.2. The experimental configurations of our QDs-PMN-PT actuator devices are shown in Figure 4.5. Fig. 4.5 (a) illustrates an overview of our hybrid semiconductor-piezoelectric device. As discussed before, the PMN-PT actuator combines the advantages of a strain-amplifying suspension platform[134,135] and continuously-variable stress[42,136]. This PMN-PT actuator pattern is cut by femtosecond laser system: two long fingers are separated by a small gap, a membrane with embedded QDs is bonded between the two fingers. The [100] orientation of the membrane is aligned with the direction of two fingers, as the side-view illustration of the device in Fig. 4.5 (b). The detailed working principles of the PMN-PT actuator used in this work can be found in Section 3.1.2.
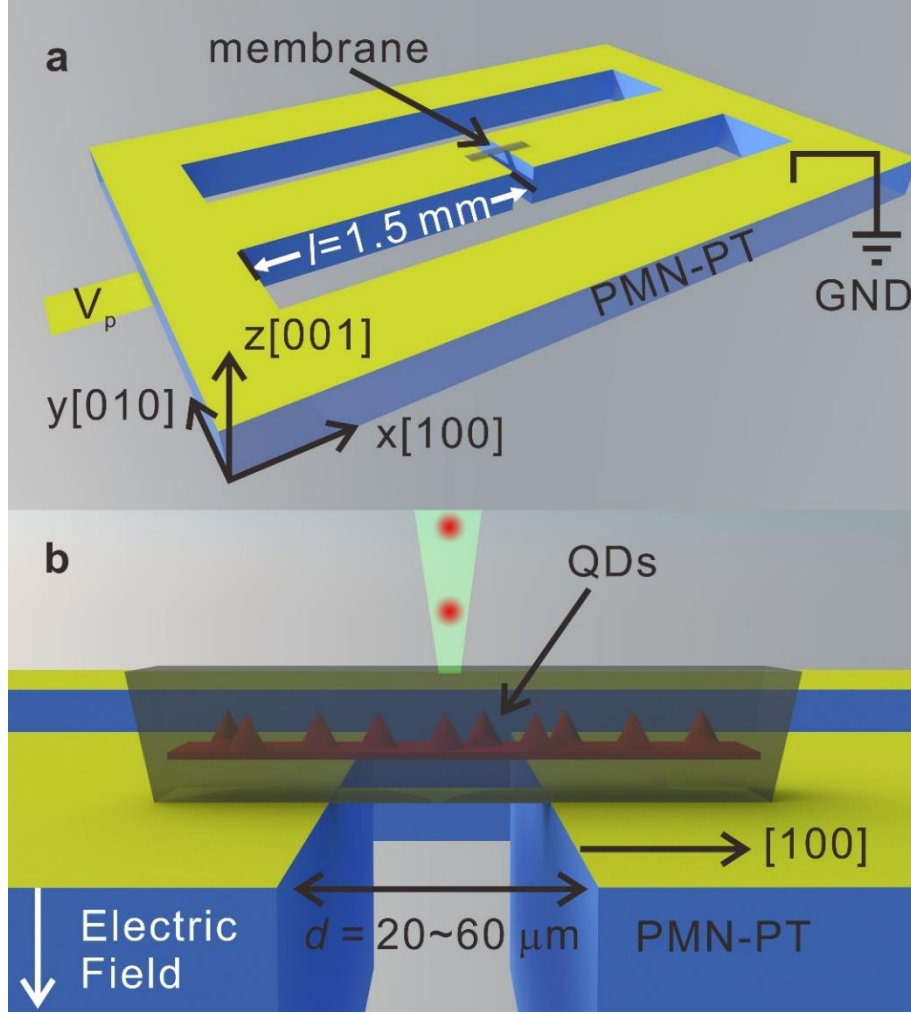
Fig. 4.5: Experimental configuration to apply uniaxial stress to GaAs QDs via a micro-machined PMN-PT actuator. (a), Sketch of the actuator featuring two fingers with length *l* separated by a gap of width *d*. A semiconductor membrane with embedded QDs is bonded on the fingers and forms a bridge above the gap. V_p is the voltage applied to the bottom of the PMN-PT actuator with respect to the top contact, which is grounded. Because of the chosen poling direction, a negative electric field F_p across the PMN-PT induces a contraction of the fingers and uniaxial tensile stress in the semiconductor along the *x*-direction. The coordinate system is the same as for the (Al)GaAs crystal. (b), Side-view of the device. PL measurements are performed by exciting and collecting PL along the *z*-axis.

Since in the experiment we were not able to provide an independent measurement of the strain configuration produced by the piezoelectric actuator, we have performed finite element method (FEM) simulations. We provide below the relation between stress and strain in the case of ideal uniaxial stress along the [100] crystal direction of GaAs and the results of the numerical calculations. Since in our case the uniaxial stress is applied along the [100] direction, there is no shear stress, so that the generalized Hooke's law of Eq 2.25 can be further simplified as:

$$\begin{pmatrix} \sigma_{xx} \\ 0 \\ 0 \end{pmatrix} = \begin{pmatrix} C_{11} & C_{12} & C_{12} \\ C_{12} & C_{11} & C_{12} \\ C_{12} & C_{12} & C_{11} \end{pmatrix} \begin{pmatrix} \varepsilon_{xx} \\ \varepsilon_{yy} \\ \varepsilon_{zz} \end{pmatrix} \tag{4.4}$$

$$\varepsilon_{yy} = \varepsilon_{zz} = -\frac{C_{12}}{C_{11}+C_{12}}\varepsilon_{xx} = -\nu_{[100]}\varepsilon_{xx} \qquad (4.5)$$

Here $\nu_{[100]}$ is the Poisson ratio for uniaxial stress along the [100] direction ($\nu = 0.31$ for GaAs at a temperature of about 10 K[137]).

Then a FEM simulation based on COMSOL Multiphysics is performed to estimate the stress configuration in our device. All calculations assume linear elastic deformations. All the parameters are set based on those of the devices.

Figure 4.6 (a) shows the major stress σ_{xx} map in our device. It shows quite homogeneous tensile stress in the suspended area of the membrane. In order to have a clearer picture of the stress distribution along the x-direction of the membrane, we make a line scan [the line is located in the middle of the membrane, marked as dashed line in Figure 4.6 (a)] along x, see Figure 4.6 (b). The suspended area (-10 μm $< x <$ 10 μm) shows homogeneous tensile stress, while the tensile stress falls rapidly when we move to the area bonded on the PMN-PT actuator and changes into compressive stress when moving away from the gap (not shown here). As mentioned above, for an ideal uniaxial stress, $\varepsilon_{yy} = \varepsilon_{zz} = -\nu_{[100]}\varepsilon_{xx}$. Figure 4.6 (c) and (d) show the in plane strain maps of the strain tensor components ε_{xx} and ε_{yy} from the simulation. It is clear that in the suspended area there is tensile strain along x direction ($\varepsilon_{xx} = 2.0\% > 0$) and compressive strain along y direction ($\varepsilon_{yy} = $ -0.62% < 0), the Poisson ratio $\nu_{[100]}$ is about 0.31, consistent with the expected value.
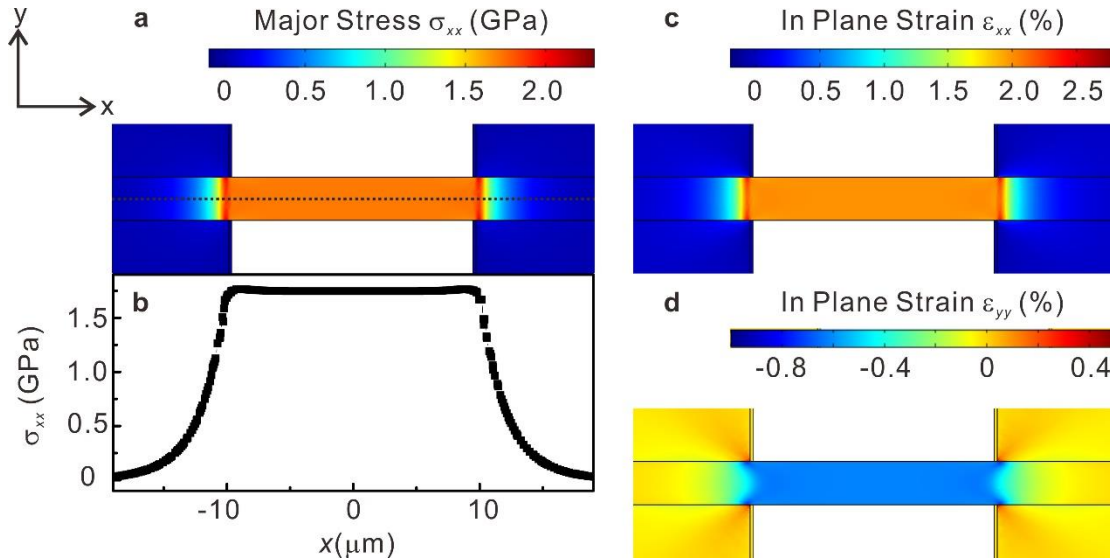
Fig. 4.6: FEM simulations of the stress and strain distribution in our devices. (a) Major stress σ_{xx} map in the middle of the membrane in z-direction (the same location of the QDs). The dashed line shows the position of the line scan in (b). (c,d) In-plane strain (ε_{xx}, ε_{yy}) maps, respectively. We verified that $\varepsilon_{zz}=\varepsilon_{yy}$, consistent with a uniaxial stress configuration.

Based on the above analysis and FEM simulation, our device is supposed to provide strictly uniaxial stress in a wide range. To test the prediction experimentally, we focus first on the achievable energy shift under uniaxial stress (detailed information can be found in section 2.2.3). Fig. 4.7 shows a typical series of PL spectra of QDs in our device with an increasing tensile stress. With the "strain amplification" device, the emission energy of GaAs QDs can be continuously shifted by more than 100 meV (estimated major strain ~2%). To our knowledge, this is already the highest tuning range achieved via piezoelectric-semiconductor device, the magnitude of strain provided with this actuator is one order larger than the monolithic ones[104]. More importantly, the emission energy of our GaAs QDs can go even below the unstrained bulk GaAs (marked with a red dashed line in Fig. 4.7) with the help of strain, which indicates that the energy shift induced by the strain already overcompensates the one arising from the confinement. This also implies that the strain modifies completely the confinement configurations from the as-grown sample, as discussed in the next section.
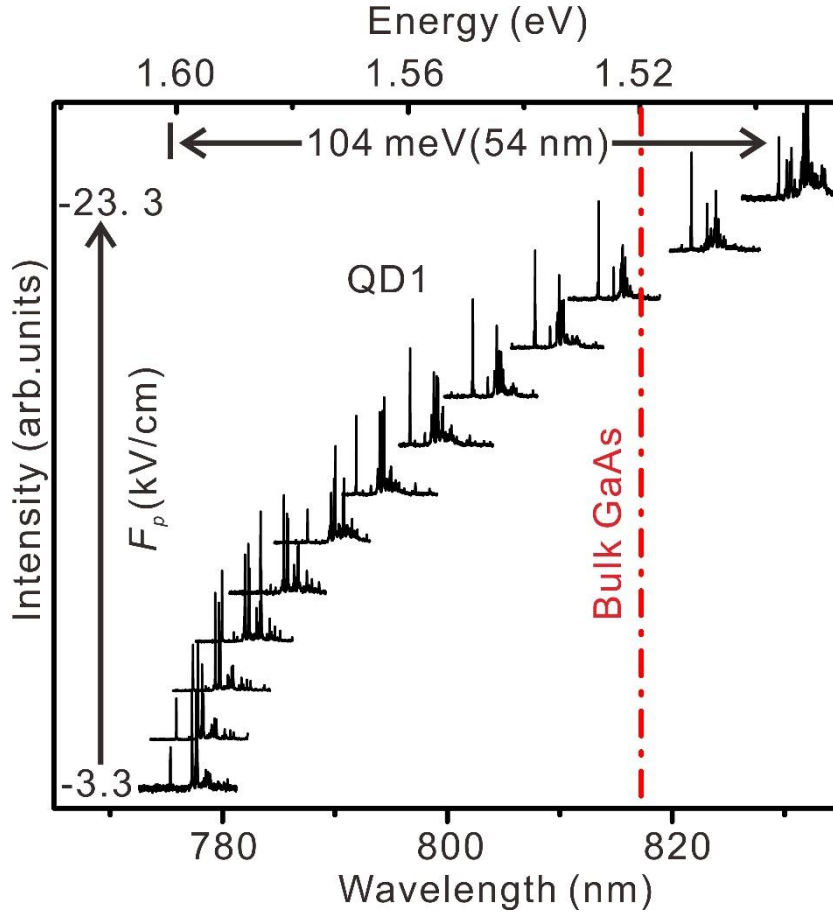
Fig. 4.7: Normalized PL spectra of a GaAs QD measured for increasing uniaxial tensile stress (from bottom to top). The large tuning range allows confinement energies to be overcompensated and leads to emission below the bandgap of unstrained bulk GaAs. The red line indicates the unstrained bulk GaAs.

Inspired by the outstanding behavior in the energy shift of GaAs QDs with our novel PMN-PT actuator, one potential application would be the interfacing single photons emitted by GaAs QDs with Rubidium (Rb) vapors. The latter can be used as a

quantum memory[138,139], which is a crucial element for a potential quantum repeater[140]. In spite of this vision, an obstacle lies in the precise matching of the emission energy of QDs to the absorption lines of natural atoms (for ^{87}Rb, the D_1 transition is near 795 nm and the D_2 transition is around 780 nm). Although several previous works have reported the tuning of QD emission to match the transition of Rb[109,141], they have two main limitations: firstly, the tuning magnitudes were limited, which means QDs with emission energy close to the desired transition must be selected; secondly, published work is still limited on the matching the QDs' energy with the D_2 line of ^{87}Rb. Although the D_2 line is used in laser-cooling experiments[142], currently some nonlinear optical process (like electromagnetically induced transparency) has been only explored with the D_1 transitions[143], and recently a quantum memory suitable for QD photons at the Rb D_1 transitions was demonstrated[144]. Here we make a simple test based on the device we have: a hot Rb cell is inserted between the QDs and the detector of the spectrometer, as shown in the inset of Fig. 4.8. By sweeping the voltage applied to the PMN-PT actuator, the emission energy of the exciton from GaAs QD is able to reversibly go through both the D_1 and D_2 lines of Rb (Fig. 4.8), this illustrates that no careful QD preselection would be needed to bring transitions of our artificial atoms into resonance with desired transitions of natural atoms.
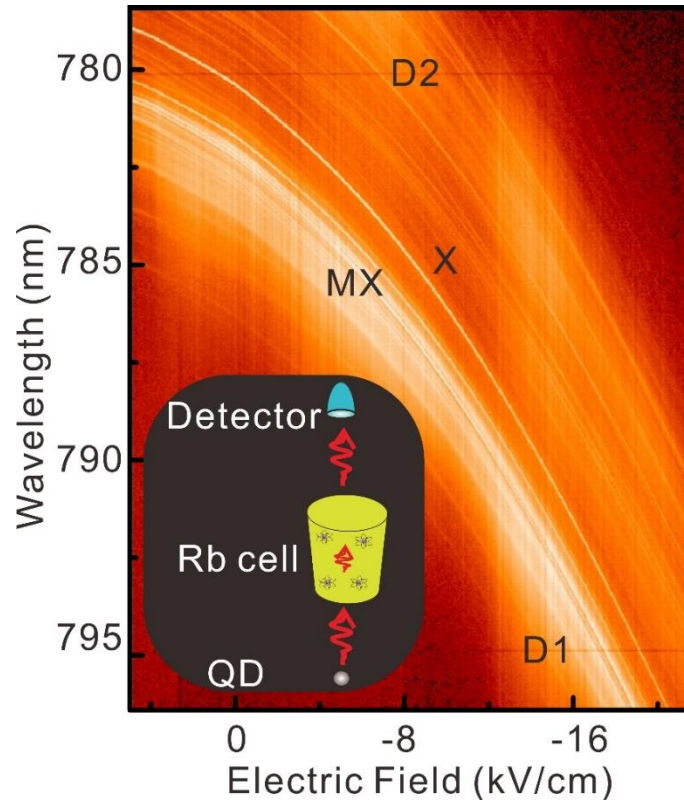

Fig. 4.8: The PL emission of a GaAs QD from our hybrid device as a function of the electric field applied to the microprocessed actuator. X and MX indicate the exciton and multiexcitons, respectively. D1 and D2 are two natural absorption lines of Rb. Inset schematically shows the experiment setup: a hot Rb cell is inserted between the QDs and the detector of the spectrometer.

4.4 Experimental proof of the rotation of quantization axis via uniaxial stress

4.4.1 Experiments using large membranes

In section 4.2, we have seen that theoretical calculations predict the possibility of rotating the quantization axis of our GaAs QD. We present now the experimental proof of the concept. At first, a device with a relatively large QDs membrane (~ 2×4 mm^2) is fabricated, the picture is shown in Fig. 4.9. Linear-polarization resolved PL spectra of emission of different GaAs QDs under increasing uniaxial stress are collected. We select 4 typical spectra under increasing uniaxial stress. Fig. 4.10 (a) shows the color-coded PL spectra of a nearly unstrained QD, here a positive electric field 5 kV/cm is applied to compensate the pre-stress which comes from the processing and cooling. The neutral exciton (X) and multi-exciton emission (MX) can be clearly resolved: the X emission shows a wave pattern dependence with the polarization angle, which stems from the FSS, as we discussed in the previous chapter. The MX lines located at the low energy side, are attributed to the recombination of a ground-state electron with ground-state hole in presence of additional carriers. The FSS has a relatively small value (~ 25 μeV) and not evident net polarization can be observed. If we apply a moderate uniaxial stress to the QD (Fig. 4.10 (b)), the FSS increases substantially to ~ 80 μeV as expected[44] and the polarization angle rotates. When we continue increasing the uniaxial stress (Fig. 4.10 (c) and (d)), significant changes are observed: both the emissions from X and MX become fully polarized parallel to the y-direction (perpendicular to the pulling (x) direction) and only one bright state can be observed in X. This is exactly what we expect based on the analysis in section 4.2, since the low numerical aperture (NA) of the used objective (0.42) and high refractive index of GaAs (~3.5) hinder the detection of the potential emerging vertically polarized component. In Fig. 4.11, we plot the linear polarization degree ($P = (I_{max}-I_{min})/(I_{max}+I_{min})$) ($I_{max/min}$ mean the maximum/minimum intensity of the neutral exciton emission peak) and polarization orientation φ* of X and MX function with electric field (the magnitude is proportional to the uniaxial stress). It is clear to see the trend that P increases with the increasing uniaxial stress and the polarization orientation φ* rotates with increasing stress. For a sufficiently large stress on our GaAs QDs, the polarization degree P can deterministically reach 1 and the polarization orientation φ* will be perpendicular to the pulling direction (x), this is not only consistent with the theoretical prediction in section 4.2 but also confirmed by measurements on one additional dot (See Appendix A.2).
The behavior of the MX line with respect to the X line under increasing uniaxial tension is presented in Appendix A.3.

56
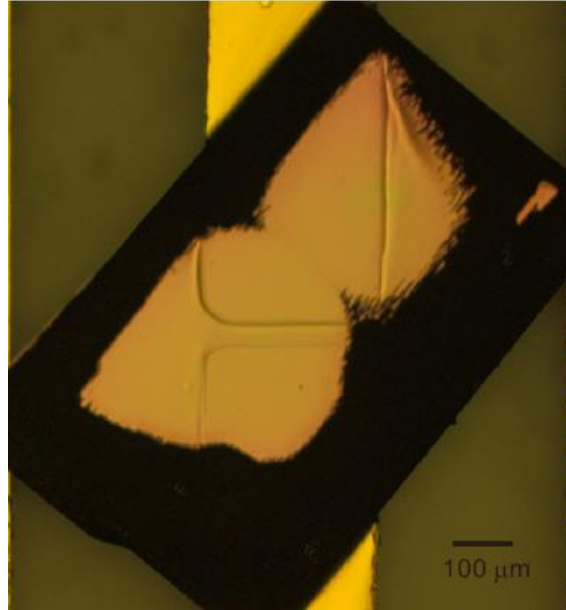
Fig. 4.9: Microscope view of the semiconductor-PMN-PT hybrid device with a large membrane (~ 2×4 mm²).
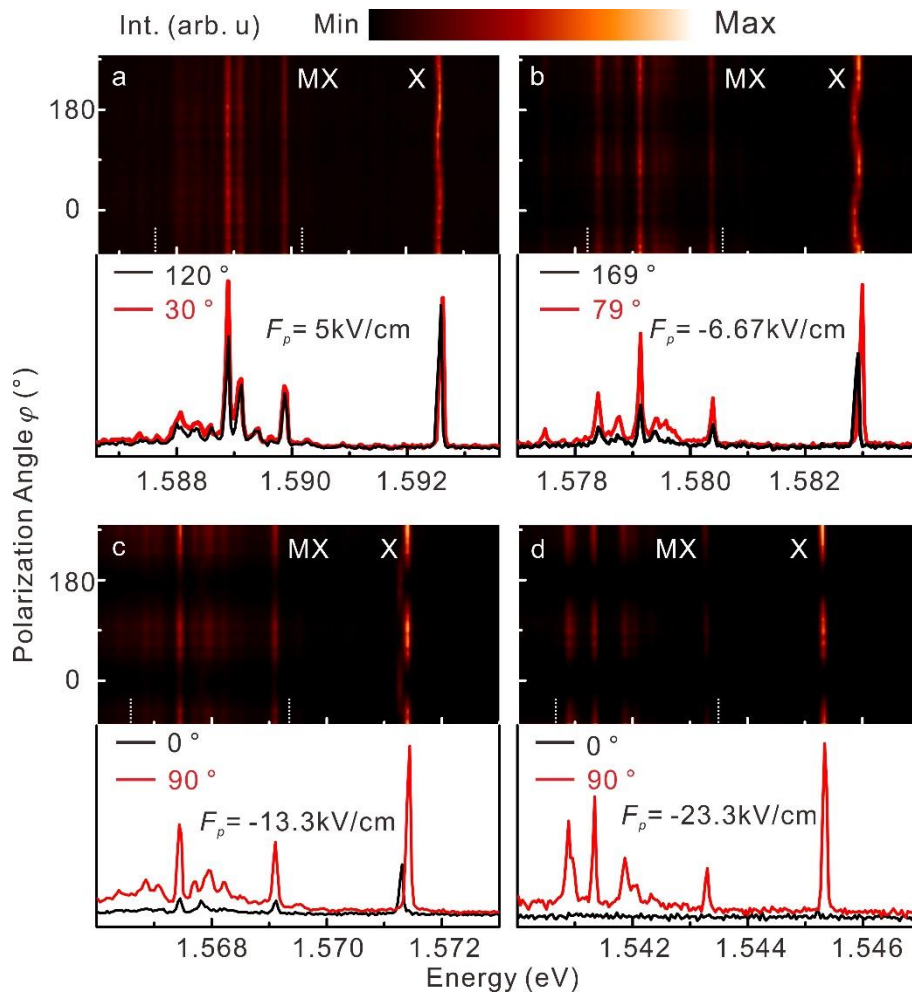
Fig. 4.10: Color-coded linear-polarization resolved PL spectra of a GaAs QD for increasing tensile stress (top) and selected spectra along orthogonal directions (bottom). The polarization angle φ is referred to

the [100] crystal direction. Initially, (a), the emission from the neutral exciton X and multiexcitons MX shows no significant net polarization and the X emission is characterized by two bright components linearly polarized along random directions (30 and 120° for this QD). This random orientation stems from slight anisotropy in the confinement potential defined by the QD and also from some process-induced prestress. At increasing stress, (b), (c) and (d), the polarization angle gradually rotates and finally is almost fully polarized along the [010] direction ($\varphi^* = 90°$).
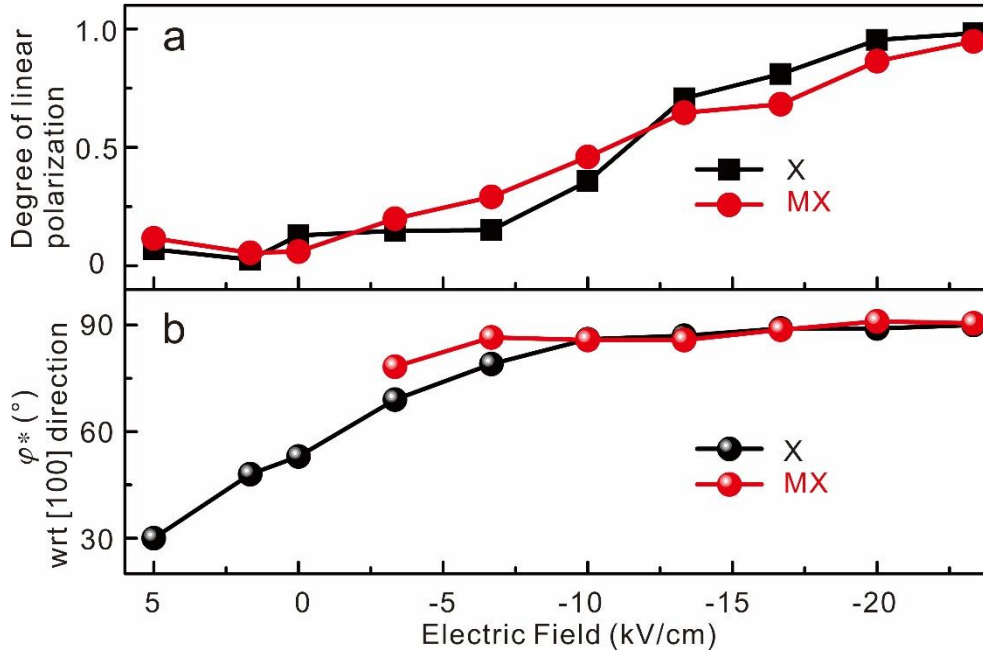
Fig. 4.11: (a), Evolution of the degree of linear polarization of X emission and MX "band" (emission between vertical dashed lines in Fig. 4.10) for increasing tensile stress (increasing magnitude of applied electric field on actuator). (b), Evolution of polarization orientation φ^* for the MX band and of the high energy component of the X line for varying stress.

Although what we observed in the QDs embedded in the large membrane is consistent with the theoretical prediction, the proof is not complete. In fact we expect that the transition from HH_z to HH_x with increasing tension should be accompanied by the appearance of transition dipoles parallel to the z direction, as explicitly seen in Fig. 4.12, which shows polar plots of the excitonic transition dipoles with increasing stress calculated with the EPM+CI methods. In the next section we unveil vertically polarized emission.

ε_{xx}= 0% ε_{xx}= 0.1% ε_{xx}= 0.15%

ε_{xx}= 0.2% ε_{xx}= 0.3%

z[001]

y[010]

x[100]
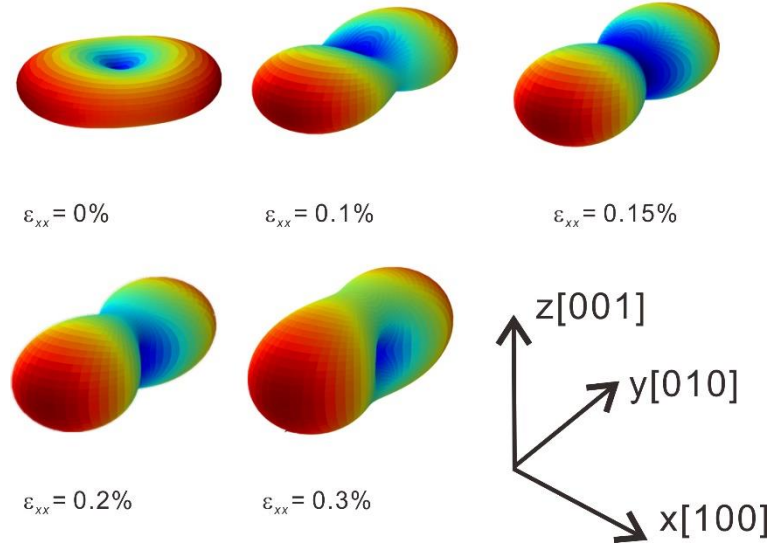
Fig. 4.12: Polar-coordinate representation of the excitonic transition dipole under different uniaxial strain calculated by the EPM+CI method using the realistic shape of our QDs (performed by Fritz Weyhausen-Brinkmann and Prof. Dr. Gabriel Bester at University Hamburg).

4.4.2 Measurements on narrow stripe membrane

Based on previous reports, there are two possible methods to detect light polarized parallel to the growth direction. The conceptually simplest is to collect light propagating in the growth plane from the sample edge, i.e. with an objective with optical axis perpendicular to the growth direction[145]. However, this strategy cannot be easily implemented in our case considering the configuration of our device: the strained part of the membranes lies far away from the edge of the PMN-PT actuator, making light collection rather difficult. An alternative way would be the fabrication of waveguide and out-coupler gratings to guide this vertically polarized component towards an objective placed above the sample[146]. Because of the unavailability of some necessary instruments (Reactive-Ion Etching (RIE) system) at JKU for the fabrication of out-couplers, we sought for an alternative approach: a wedged geometry produced via wet chemical etching can project the z polarized bright states towards the z-direction, which is compatible with the collection configuration we used (as shown in Fig. 4.5 (b)).

To illustrate the feasibility of this idea, a dummy GaAs substrate is first employed. Then conventional UV-lithography of a 3.5 μm narrow beam is performed, followed by wet chemical etching (H_2SO_4:H_2O_2:H_2O (1:8:200 in volume ratios) solution at room temperature). Then we removed the photoresist with acetone. To obtain the morphology of the pattern after etching, an AFM topography measurement is performed. From the AFM image in Fig. 4.13, it is evident that undercut occurs during the wet etching, which leads to tilted membrane side walls. When the QD membrane is bonded to the PMN-PT substrate, the membrane is flipped upside down, as shown in Fig. 4.14 (a), thus the tilted sidewalls would act as mirrors to partially project the vertically polarized components along the z-direction (marked in red in Fig. 4.14 (a)). In addition, from the geometry, we expect the z-polarized light will be converted to y-polarized light.

Following this idea, narrow stripe membranes (3.5 μm) are defined with wet chemical etching, then bonded to the PMN-PT actuator, Fig. 4.14 (b) shows the optical image of the device with a narrow beam membrane.
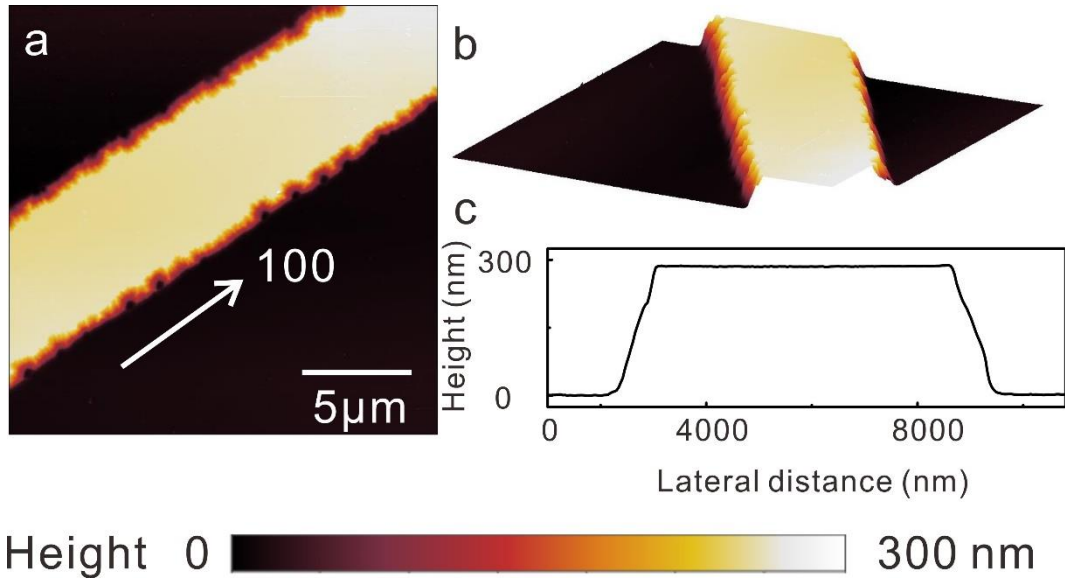
Fig. 4.13: (a) AFM image of stripe-like membrane after H_2SO_4:H_2O_2:H_2O etching (b) 3D view of the AFM image of etched membrane. (c) Line profile of etched membrane.
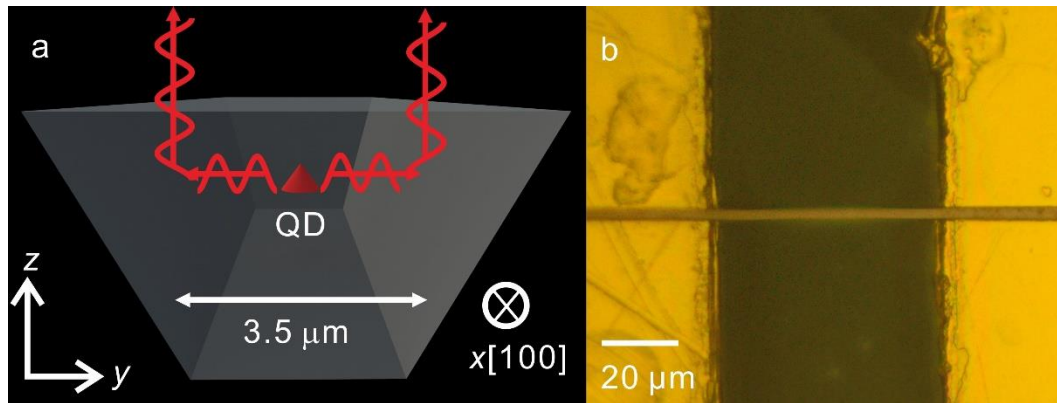
Fig. 4.14: (a) Sketch of the cross-section (y-z plane) of the stripe-like membrane used to project the vertically polarized into the collection optics. From the geometry, we expect such light to appear as y-polarized. (b) Micrograph of a device consisting of a narrow stripe (3.5 μm in width) membrane bonded to the micro-machined PMN-PT actuator.

With the narrow beam membrane, polarization-resolved PL spectra of neutral excitons X from different QDs under variable tensile uniaxial stress are measured, obtaining consistent results. Here we show a series of polarization-resolved PL spectra from two typical QDs, in Fig. 4.15. Compared to the data collected on QDs in large membranes, with the increasing magnitude of electric field applied (stress), an additional y-polarized component appears and becomes brighter with the stress. As shown in Fig 4.15 (a), the initially dark state D_z becomes partially bright with the aid of the a moderate uniaxial stress. With the increase of the uniaxial stress, the D_z

becomes brighter and moves from the low energy side to the high energy side of the bright exciton line B_y. This emerging component D_z/B_z is polarized along the y-direction, consistent with our expectation for vertically polarized light. At the same time, the initially bright state B_x moves to the low energy side of the B_y with the increasing uniaxial tensile stress, as previously observed in large membranes. Moreover, the intensity of B_x drops monotonically with increasing stress (for this reason we refer to it as D_x for large tensile stress).
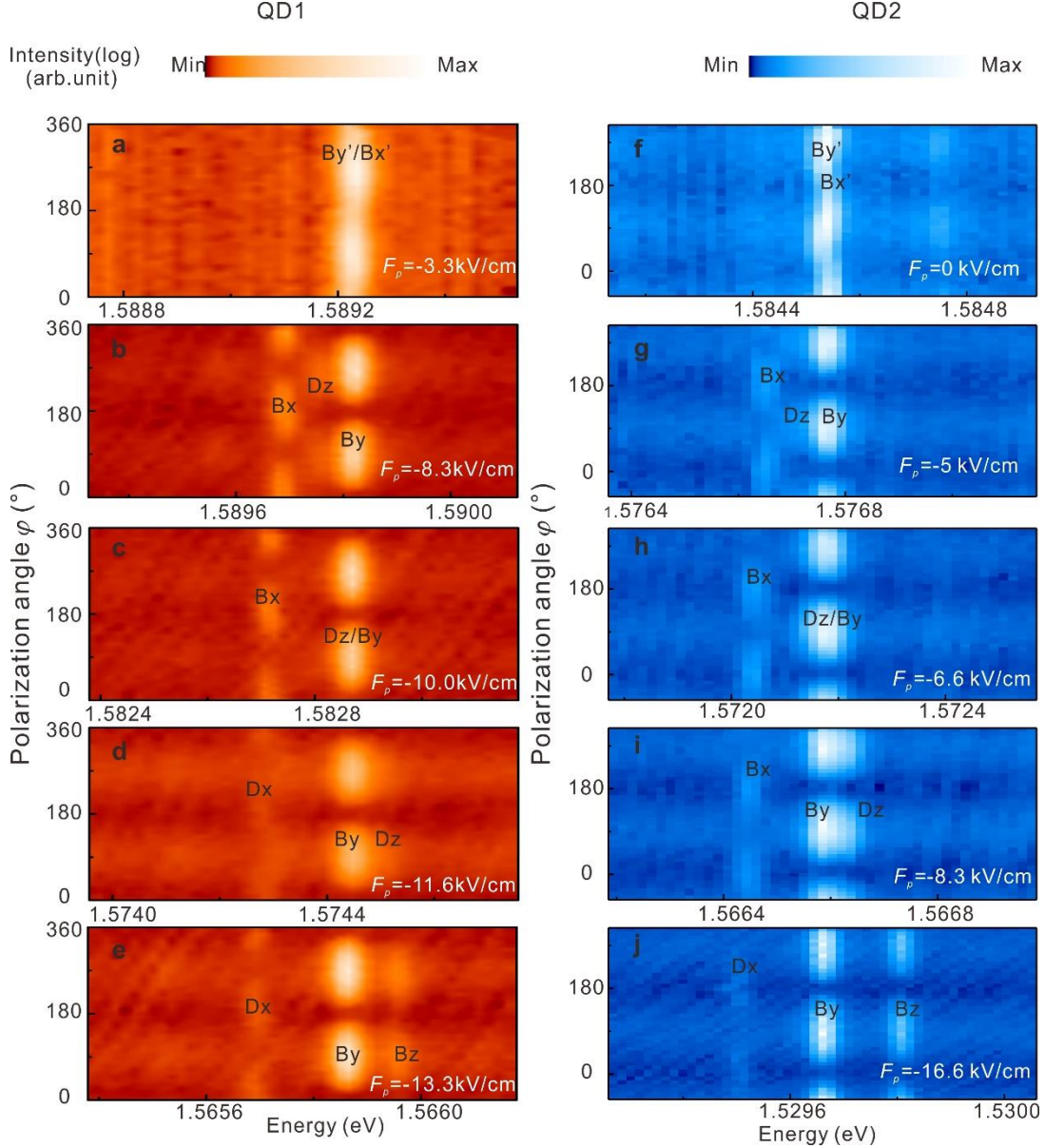
Fig. 4.15: Color-coded polarization-resolved PL signal of a neutral exciton emission in a GaAs QD for different values of the electric field applied to the actuator. Tensile stress increases from top to bottom. An angle of 0° corresponds to polarization along the pulling direction x. D_z stands for one of the initially dark states, while D_x is the dark exciton state under tensile stress, B_y and B_z are the new two bright exciton states under tensile stress. The chosen color-scale (in log scale) enhances also weak features. (a)-(e) show the evolution of exciton emission from QD1 (the same one shown in Fig. 4.7) and (f)-(j) show the evolution of exciton emission from another QD (here we name it QD2).

We show the evolution of the neutral exciton X emission from another QD (QD2) for increasing uniaxial stress in Fig. 4.15 (f)-(j). Very similar trends are observed.

Since with increasing uniaxial stress one bright state keeps bright, we employ this bright state as a reference and shift other emissions horizontally to better illustrate the evolution of neutral exciton X under uniaxial stress. Fig. 4.16 (a)-(c) show a series of PL spectra of X emission from QD2 with different stresses. Initially the emission is characterized by two lines ($B_{x',y'}$), which are linearly polarized perpendicular to each other in the x-y plane and are split by the FSS, see Fig. 4.16 (a), which is the typical signature of a HH_z exciton. For the investigated type of QDs, the orientations x' and y' are quite random and the average FSS is rather low (~ 4 μeV)[29]. We stress here that fluctuations in the azimuthal orientation of the transition dipoles are commonly encountered also for other QDs[147] and represent a problem if the light has to be efficiently coupled into a waveguide. Then with increasing uniaxial stress, the distance between the two lines becomes larger. Meanwhile, the polarization direction (φ) of the high (low) energy component rotates and align to the y (x) with increasing (Figure 4.16 (b)), and this is independent of the initial orientation of the dipoles. And as we mentioned before, the intensity of $B_{x'}/B_x$ drops with the increasing uniaxial stress, indicating that this bright states $B_{x'}$ converts to a dark state with stress. Simultaneously an initially dark state D_z increases in brightness and moves to the high energy side of B_y. With increasing uniaxial stress, one of the initially bright states becomes nearly completely dark and an initial dark state becomes a new bright state B_z. Here we want to emphasize that, since this component D_z/B_z is never observed in QDs in the large membrane, we can safely attribute this feature to be a z-polarized component. After collecting and averaging the polarization resolved PL spectra of the QD at each specific voltage applied to the PMN-PT actuator, in Fig. 4.16 (d) we show the overview of the evolution of neutral exciton X under variable uniaxial stress. From previous experiments[106] we know that the $B_{x',y'}$ undergo an anticrossing at moderate strain levels (magnitude of F_p below -7.5 kV/cm). However, when the strain is larger enough, the 'FSS' will not change linearly with the stress (F_p), which is different from the behavior of perturbative regime[38], this is also an indirect indication that it is not proper to use the old quantization axis. Moreover, the ($B_{y'}{\rightarrow}B_y$)-($B_{x'}{\rightarrow}D_x$) splitting almost saturates at a value of ~200 μeV for all investigated QDs.

Figure 4.16 (e) shows the evolution of the X emission under tensile stress along [100] as calculated with EPM+CI. As in the experiment, energies are referred to the B_y line. The size of the symbols is proportional to the strength of each transition. The calculations qualitatively reproduce all the experimentally observed features including the darkening of one of the initially bright excitons and the brightening of one of the initially dark excitons. Also the energy shifts follow the experiment, although the absolute magnitudes are systematically smaller, which is currently under investigation.
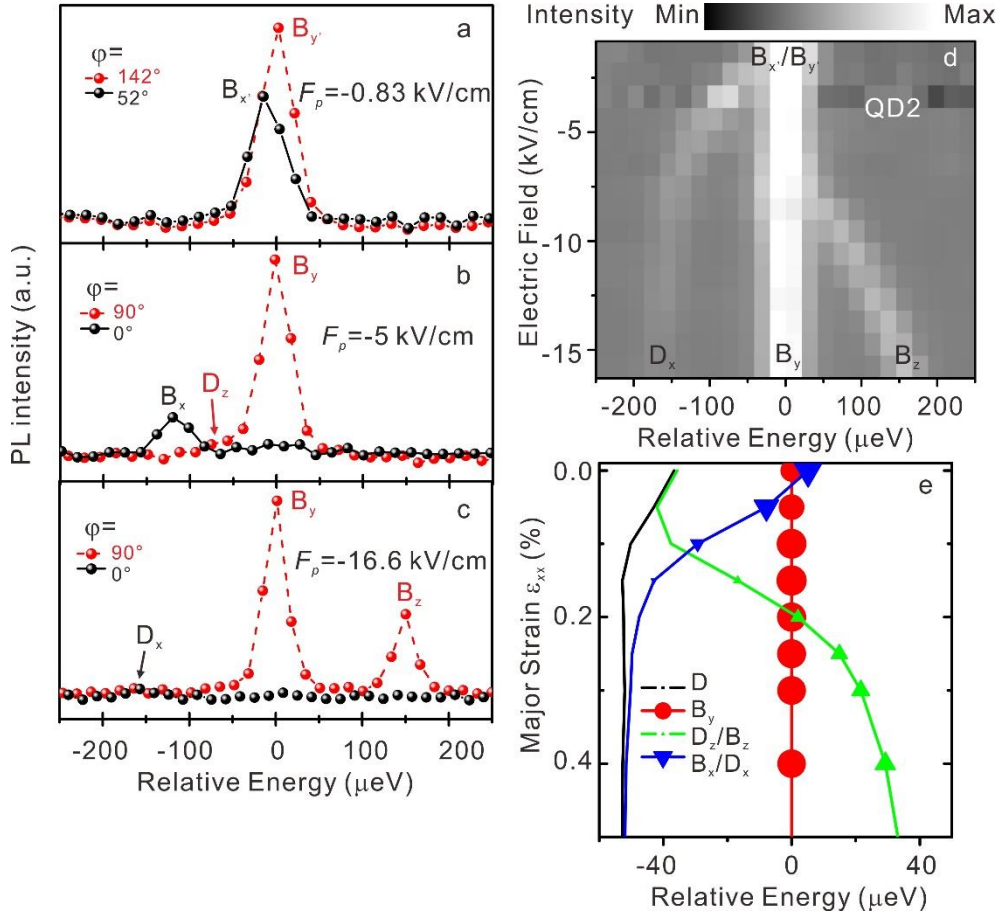
Fig. 4.16: (a)-(c), Representative linearly polarized PL spectra of the X emission in QD2 for different values of the field F_p applied to the actuator (uniaxial stress). In (a) we see the usual fine-structure-splitting (FSS) of a HH_z exciton, characterized by two orthogonally polarized lines. The observed polarization anisotropy, relatively large FSS (14 µeV), and random orientation of the polarization directions are ascribed to HH_z-LH_z mixing induced by QD anisotropy and process-induced prestress. The applied uniaxial stress aligns the transition dipoles along the crystallographic axes, as shown in (b) and (c). z-polarized emission appears first as a shoulder on the low energy side of the B_y line (marked as D_z in (b). The emission of a HH_x exciton is shown in (c). (d), PL spectra of the neutral exciton (X) emission of a QD as a function of electric field applied to the piezoelectric actuator. Spectra are shifted horizontally using the line labeled as $B_{y'}$ or B_y as reference. (e), Relative transitions energies of the four excitonic components under uniaxial stress (compressive, top and tensile, bottom) computed by EPM+CI. The symbol size is proportional to the oscillator strength of the transitions.

4.5 Quantitative determination of stress using monolithic PMN-PT actuator and embedded strain gauge

In the previous sections we have discussed the effects produced by uniaxial stress on the emission of GaAs QDs. In the used samples it was unfortunately not possible to determine the quantitative values of stress and also to study the behavior under compressive stress. To address these point and enable the quantitative comparison of

experimental results and calculations, a new device was employed, although at the expense of a narrower tuning range. In this new device, a 100 μm thick (110)-cut PMN-PT actuator was used to provide highly anisotropic in-plane (quasi-uniaxial) stress. Hence we just need to align the [100] crystal axis of GaAs to the major anisotropic stress axis of the PMN-PT actuator and make the bonding. By sweeping the voltage applied between the top and bottom sides of the actuator, the properties of QDs under both tensile and compressive quasi-uniaxial stresses can be studied, as shown in Fig. 4.17 (a). To experimentally quantify the values of stress applied on the QDs, a sample with 150 nm GaAs layer was used (the structure of the QDs-contained membrane is displayed in Fig. 4.17 (b)) and the PL emission of the GaAs layer will be used as the stress (strain) gauge, since its PL response to the deformation was well studied[110,148,149].
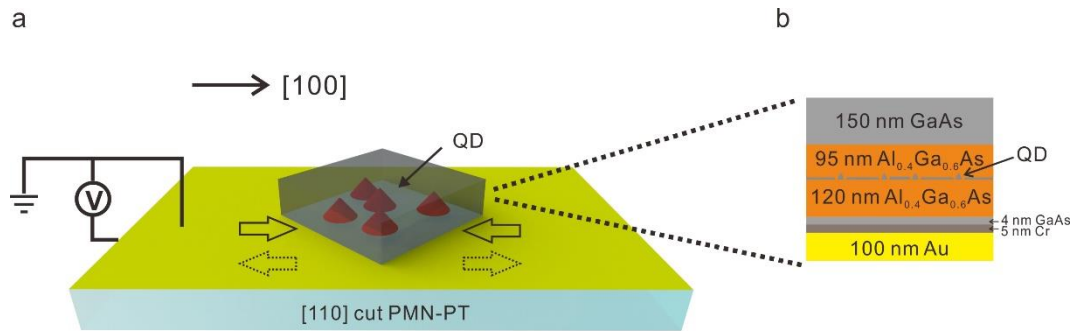
Fig. 4.17: (a) Sketch of the device, in which a QDs-containing membrane was bonded on a (110) cut PMN-PT substrate. A quasi-uniaxial stress can be obtained through applying the voltage between the top and bottom sides of the actuator. (a) The schematic structure of the membrane, which consists of 150 nm GaAs, 95 nm $Al_{0.4}Ga_{0.6}As$, 120 nm $Al_{0.4}Ga_{0.6}As$, 4 nm GaAs, 5 nm chromium and 100 nm gold. The QDs were sandwiched between layers of $Al_{0.4}Ga_{0.6}As$.

The main idea is as follows: LH and HH are degenerate at Γ point in absence of strain, while in-plane stress will break the crystal symmetry and eliminate the degeneracy, leading to the appearance of two PL emission peaks (as shown in Fig. 4.18 (a)-(c)). These two peaks can be attributed to the radiative recombination of the electrons in CBs and holes in the strain-split VBs. Using these energy values and polarization angles of the two peaks as input data, we adopted the Pikus–Bir Hamiltonian model[148] (see Sec. 2.2.3) to figure out the strain configurations which show minimum deviations between the experimental and fitted value. Fig. 4.18 (b)-(f) are the polarization resolved PL spectra of the neutral exciton X under different strains (the ε_{xx} were calculated from the PL spectra of thick GaAs layer). Compared to the studies using two-finger PMN-PT actuator, qualitatively consistent results were obtained: with an increasing tensile quasi-uniaxial stress, the FSS increased and an evident linear polarization was observed. While if we took a sight to the compressive regime, which was within the scope of study using the two-finger PMN-PT actuator, the FSS kept increasing with an increasing amplitude of compressive stress and linear polarization degree, which is parallel to the compression direction, started to emerge. Besides, the FSS and DOLP for neutral exciton X showed an asymmetric dependence under tension and compression. Some further studies, including the physical origin and intrinsic

lifetime dependence on the uniaxial stress, are under investigation within a collaboration with Dr. Petr Klenovsky from Masaryk University, Brno.
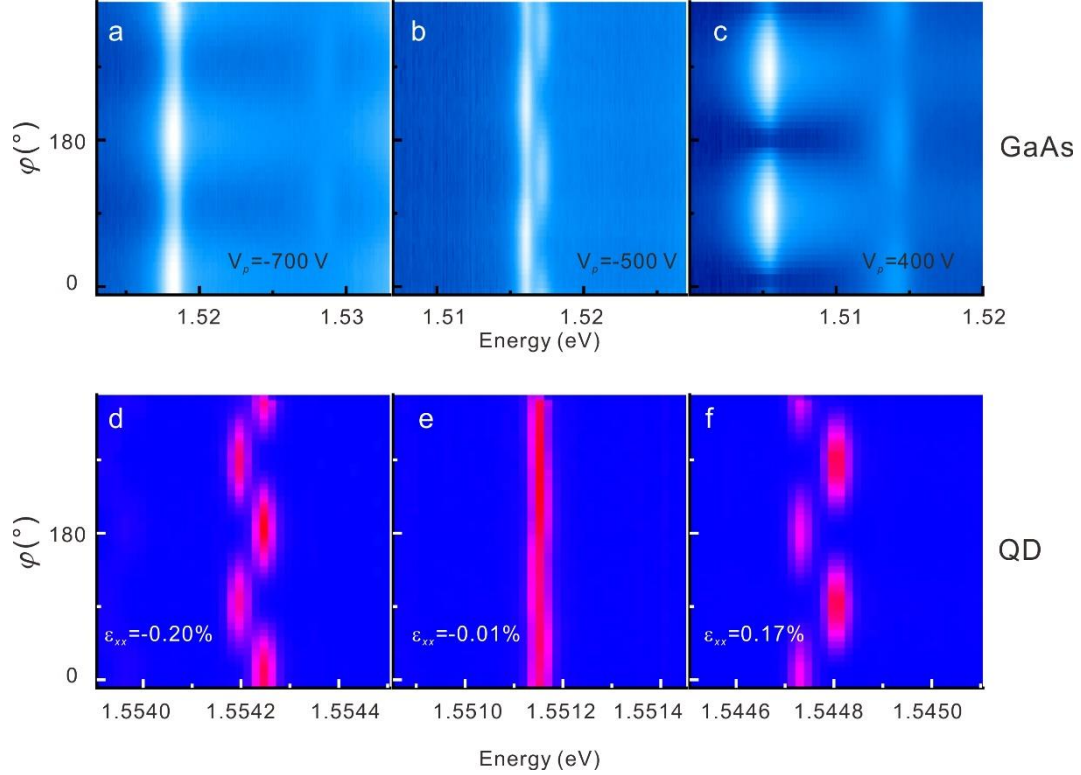
Fig.4.18: (a)-(c), Polarization resolved PL spectra of GaAs (the 150-nm-thick layer seen in Fig. 4.17(b))for various voltages (V$_p$) applied to the PMN-PT actuator. (d)-(f) Polarization resolved PL spectra of the neutral exciton (X) emission from GaAs QDs at different strains, the ε$_{xx}$ indicated the major strain obtained from the PL spectra of thick GaAs layer.

4.6 Conclusion and outlook

In summary, the rotation of the natural quantization axis of GaAs QDs is demonstrated upon application of uniaxial tensile stress. With this new quantization axis, two new bright eigenstates replace the old ones.

Through a novel micro-machined PMN-PT actuator, strain-free GaAs QDs and narrow stripe membranes with tilted sidewalls, we managed to experimentally prove the rotation of quantization axis with uniaxial effect. We believe this work will have potential implications for integrated quantum photonics[124,150]. Especially relevant features of quantum emitters in such applications are: (i) efficient light-coupling to guided modes. Indeed what counts is the orientation of the transition dipoles d with respect to the electric field E_k corresponding to the guided mode k in a photonic waveguide. The coupling efficiency is in fact proportional to $|d \cdot E_k|^2$. For optimal coupling, the QDs should thus feature at least one transition dipole parallel to E_k. However, in conventional QDs, (with the heavy-hole ground state, described by a total angular momentum projection Jz=±3/2 along the z-quantization axis, which coincides with the growth direction) the azimuthal orientation of the transition dipoles (in the

growth plane) is affected by random fluctuations[29,147]. By setting instead the of quantization axis for the holes total angular momentum in the growth plane, we achieve a deterministic control of the orientation of the transition dipoles. (ii) Fast radiative recombination, which is beneficial for high photon rates and indistinguishability. Indistinguishable single photons are considered as the most fundamental and key building blocks for quantum computation and networks, however the non-ideal indistinguishability of photons emitted by QDs is a longstanding obstacle to application. The QDs used in this work already show excellent single photon purity and good indistinguishability when excited resonantly with two-photon absorption[22,70,71], which is compatible with planar photonic circuits and strongly reduces exciton recapture. Besides, no line broadening is observed during the experiments presented above, which make us confident that the optical properties are not deteriorated by the uniaxial stress along [100] direction. (Results of experiments with stress applied along piezoelectric directions ([110] and [$1\bar{1}0$] directions) are shown in Appendix A.4)

If we inspect the calculated transition strengths of excitonic dipoles under uniaxial compression (shown in Fig. 4.19 (a)), the emission of a LH_x-exciton is dominated by a single emission line with polarization parallel to the compressive stress direction and with an oscillator strength which is almost twice that of each of the two bright excitons in our HH_z QDs. Considering that HH_z excitons in GaAs QDs are already characterized by very short lifetimes (~250 ps)[70,71], the combination of deterministic QD positioning in photonic structures[151,152], and uniaxial-strain-engineering (as sketched in Fig. 4.19 (b)) may lead to ideal single-photon sources with enhanced recombination rate [~8 GHz, see right axis of Fig. 4.19 (a)] and indistinguishability levels. Different from the most common strategy to couple the QDs to high Q optical cavity[153,154], here strain induced suppression y and z polarized emission will result in a "oscillator-strength concentration" on the x-polarized emission, and a lifetime reduction and higher indistinguishability are expected.
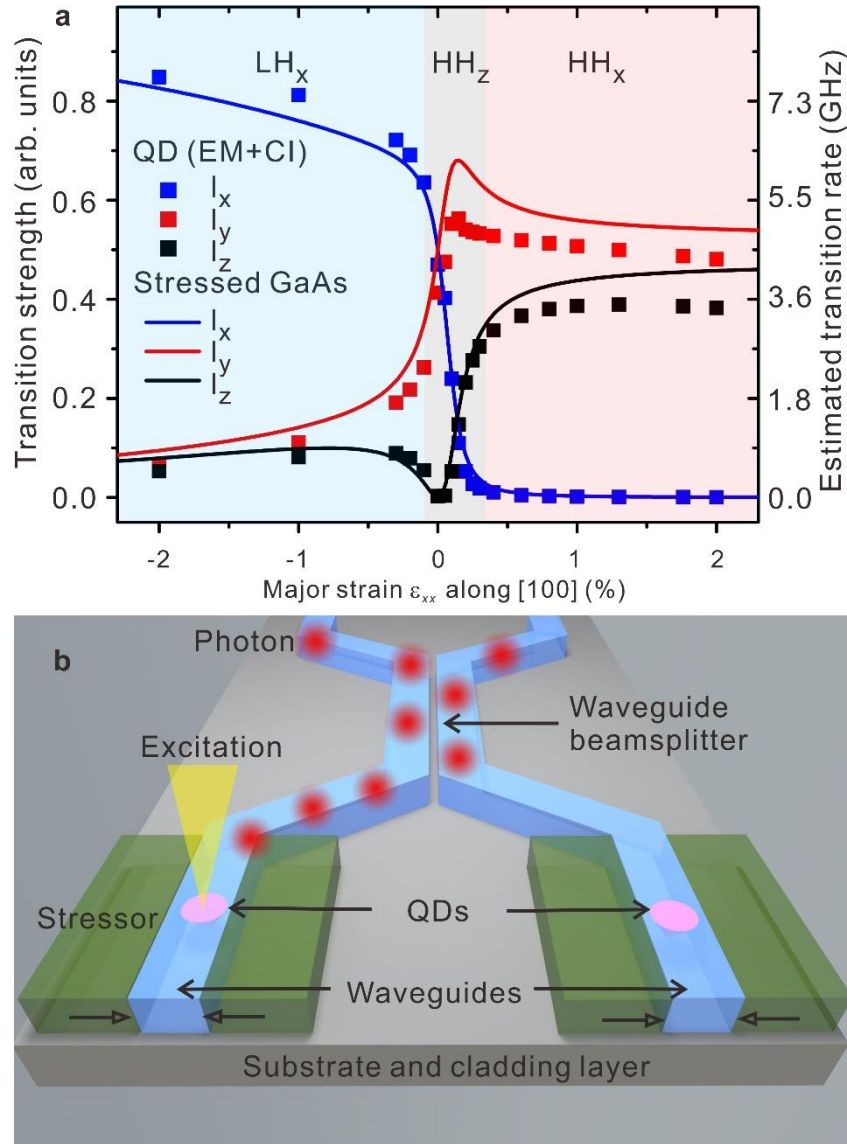
Fig. 4.19: Envisioned applications of strain-engineered single photon source for integrated quantum photonic circuits. (a), Calculated transition strength and estimated rates for light polarization along the x (blue), y (red), and z (black) directions for varying uniaxial stress along x for QDs with structure taken from experiment (symbols) and GaAs subject to a fixed biaxial compression with $\sigma_{xx}=\sigma_{yy}=-120$ MPa (solid lines). (b), Envisioned approach to obtain high-speed single-photon sources based on LHx excitons confined in GaAs QDs. A waveguide is fabricated to contain preselected QDs followed by deposition of side dielectric layers, which act at the same time as cladding, passivation and stressor layers. The uniaxial stress (produced, e.g. by the different thermal expansion coefficients of dielectric and (Al)GaAs heterostructure aligns the quantization axis of the QD along the stress direction (x) and the resulting LHx exciton acts as an ultrafast source of single photons ideally matched to the propagating modes in the waveguide.

5. Monitoring the motion of a frequency-tunable micromechanical oscillator with single quantum dots

In the previous chapter, we have discussed how a novel micromachined piezoelectric actuator can be used to study the effects produced by uniaxial stress on the electronic structure and optical properties of GaAs QDs embedded in suspended nanomembranes. These nanomembranes, with mass down to about 100 picograms, can be considered as micromechanical oscillators. Because of the high sensitivity of QDs to mechanical deformations, we now use the emission of single QDs to monitor the oscillations of nanomembranes and show that our actuator can be used both to excite mechanical resonances and tune their frequencies.

5.1 Introduction

Micro- and nano-mechanical resonators are widely employed as sensors because of their response to, e.g., electric, magnetic and optical forces. New avenues for nano-mechanical resonators have recently opened up by combining such mesoscopic objects with two-level quantum systems [155]. Ideas range from mechanical control of quantum mechanical systems such as single spins[156], quantum non-demolition (QND) measurements of the state of the quantum systems by reading the mechanical state of the resonator[157], to the use of mechanical oscillations to mediate the interaction between distinct quantum mechanical systems[158,159]

Work on optically active quantum dots coupled to mechanical resonators is still limited. Yeo *et al.*[160] and Montinaro *et al.*[161] presented first steps towards the experimental realization of these hybrid devices: QDs embedded nanowires were coupled with the mechanical resonance. In both cases oscillations were excited by piezoelectric actuators. In a recent work, Carter *et al.*[162] have investigated the coupling of spins to the motion of a cantilever excited with an amplitude-modulated laser. They found that the hole g-factor sensitively responds to the modulated strain produced by the oscillations. The possibility of modulating the g-factor of electrons or holes confined in QDs via strain opens up the possibility of controlling the state of confined spins via g-tensor modulation techniques at constant magnetic fields [163]. Compared to electric-field based g-tensor modulation, a strain-field g-tensor modulation may be beneficial because of reduced hole dephasing produced by charge noise [164]. In all the mentioned works the frequency of the oscillations was dictated by the structural parameters of the used mechanical resonators.

Although some groundbreaking works on QDs optomechanical device have been achieved[160,161], the coupling strength and resonant eigenfrequencies are not in-situ

tunable through the external fields. In this chapter, we realize a novel tunable hybrid quantum-dot-mechanical-resonant-system, a strong coupling is implemented between nanomembranes and QDs. Since QDs are sensitive to strain fields, here we take the advantage of the vibration theory of beams to couple the QDs with the mechanical vibrating of nanomembrane.

5.2 Vibrations theory of beams

The mechanical resonator used in this work can be simplified as a vibrating beam. Oscillations are excited by applying an AC voltage across the two fingers of the micromachined actuator. Considering the deformation caused by the PMN-PT actuator, there will be two main modes of the vibrations: transverse and longitudinal vibrations. In this work we only focus on the transverse modes and more information on longitudinal mode can be found in Ref[165]. Here a classic model on the effect of an axial force on the transverse vibration of beams will be introduced. A vibrating beam is subject to a tensile force S along x, as shown in Fig. 5.1. The differential equation for the deflection v at a position x under dynamic transverse loading reads (Euler-Lagrange equation)[166,167]:

$$EI\frac{d^2v}{dx^2} = M + Sv,$$ (5.1)

where E is the modulus of elasticity, M stands for the bending moment produced by a transverse loading of intensity w, I is the area moment of inertia. Then by two times differentiation of equation (5.1) with respect to x, we get

$$\frac{d^2}{dx^2}\left(EI\frac{d^2v}{dx^2}\right) = w + S\frac{d^2v}{dx^2}$$ (5.2)

To obtain the differential equation for transverse vibrations, the inertial force per unit length for w is assumed and equation (5.2) can further reads:

$$\frac{\partial^2}{\partial x^2}\left(EI\frac{\partial^2v}{\partial x^2}\right) - S\frac{\partial^2v}{\partial x^2} = -\rho A\frac{\partial^2v}{\partial t^2}$$ (5.3)

Where ρ is the density of beam and A is its cross-section area.
Assuming the beams is under one of the modes of transverse vibration, the solution of equation (5.4) can be expressed in the form as follows,

$$v = X(A_1\cos\omega t + A_2\sin\omega t)$$ (5.4)
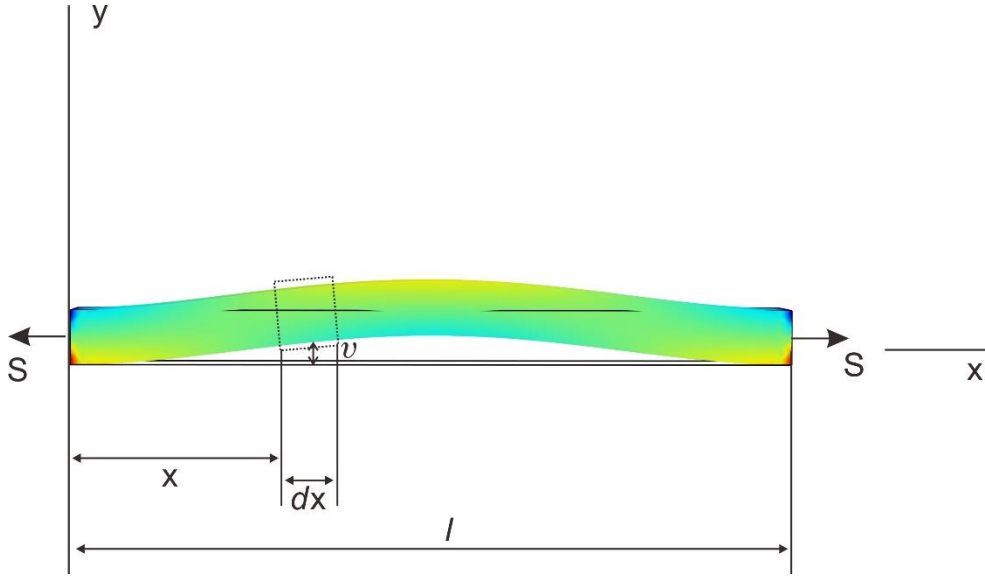
Fig. 5.1: Schematic picture of an axially forced beam

Where X is a spatial distributed function, and substituting equation (5.4) into equation (5.3),

$$EI\frac{d^4X}{dx^4} - S\frac{d^2X}{dx^2} = \rho A\omega^2 X \tag{5.5}$$

To obtain the analytical solution of the equation, we follow Ref.[168]. By introducing the dimensionless beam coordinate $\varsigma = x/l$, where $0 \le \varsigma \le 1$, the general solution of (5.5) can be written as:

$$X = c_1 \sinh M_1\zeta + c_2 \cosh M_1\zeta + c_3 \sin N_1\zeta + c_4 \cos N_1\zeta \tag{5.6}$$

Where c_1, c_2, c_3, c_4 are constants and M, N are defined as:

$$M_1 = l\sqrt{\frac{S}{2EI} + \sqrt{\left(\frac{S}{2Ei}\right)^2 + \frac{\rho A}{EI}\omega^2}} = \sqrt{U + \sqrt{U^2 + \Omega^2}}$$

$$N_1 = l\sqrt{-\frac{S}{2EI} + \sqrt{\left(\frac{S}{2Ei}\right)^2 + \frac{\rho A}{EI}\omega^2}} = \sqrt{-U + \sqrt{U^2 + \Omega^2}} \tag{5.7}$$

$U = \frac{Sl^2}{2EI}$ is the dimensionless tension parameter, $\Omega = \frac{\omega l^2}{\alpha}$ is dimensionless natural frequency parameter, I is the second moment of area, $\alpha = \sqrt{\frac{EI}{\rho a}}$ is a dimensionless parameter and i is the vibration mode number.

If we consider the boundary conditions for the doubly clamped beam model, which are：

$$X_{x=0} = 0; \left(\frac{dX}{x}\right)_{x=0} = 0; X_{x=l} = 0; \left(\frac{dX}{x}\right)_{x=l} = 0 \tag{5.8}$$

After a series substitution and simplifications, we obtain a final "*characteristic-beam-equation*"[165]:

$$\Omega + U \sinh \sqrt{U + \sqrt{U^2 + \Omega^2}}^2 \sin \sqrt{-U + \sqrt{U^2 + \Omega^2}} - \Omega \cdot$$

$$\cosh \sqrt{U + \sqrt{U^2 + \Omega^2}} \cos \sqrt{-U + \sqrt{U^2 + \Omega^2}} = 0 \qquad (5.9)$$

A numerical solution of this equation can be obtained[165]:

$$f_i^{stress} = f_i^{free} \cdot \overline{\Omega}$$

$$f_i^{free} \approx \left(i + \frac{1}{2}\right)^2 \cdot \frac{\pi}{2\sqrt{12}} \cdot \frac{h}{L^2} \cdot \sqrt{\frac{E}{\rho}} \qquad (5.10)$$

f_i^{stress} and f_i^{free} are the vibration eigenfrequencies with and without axial stress, respectively.

$$\text{And } \overline{\Omega} = \frac{\Omega}{\Omega_i} = \sqrt{1 + 0.97\overline{U}} \qquad (5.11)$$

Which defines the variation of the normalized natural frequency parameters with the normalized tension parameter for all modes, Ω_i is the dimensionless natural frequency parameter under no axial force in vibration mode i. Here the normalized tension parameter $\overline{U} = \frac{U}{U_{mi}}$, $U_{mi} = \frac{(i+1)^2\pi^2}{2}$, and U_{mi} denotes the dimensionless critical buckling load.

Lastly, if insert the second moment I for a rectangular cross-sectional area with $\frac{Ah^2}{12}$, $T = \sigma A$, σ is the tensile stress. Equation (5.11) can be further written as:

$$\overline{\Omega}(\sigma) = \sqrt{1 + 0.97 \cdot \frac{12}{\pi^2} \cdot \frac{\sigma l^2}{Eh^2} \cdot \frac{1}{(i+1)^2}} \qquad (5.12)$$

From this equation we see that the resonance frequency increases with tensile stress. To give a visualized image of the transverse vibration modes, the first four transverse vibration modes are presented (with COMSOL Multiphysics) in Fig. 5.2
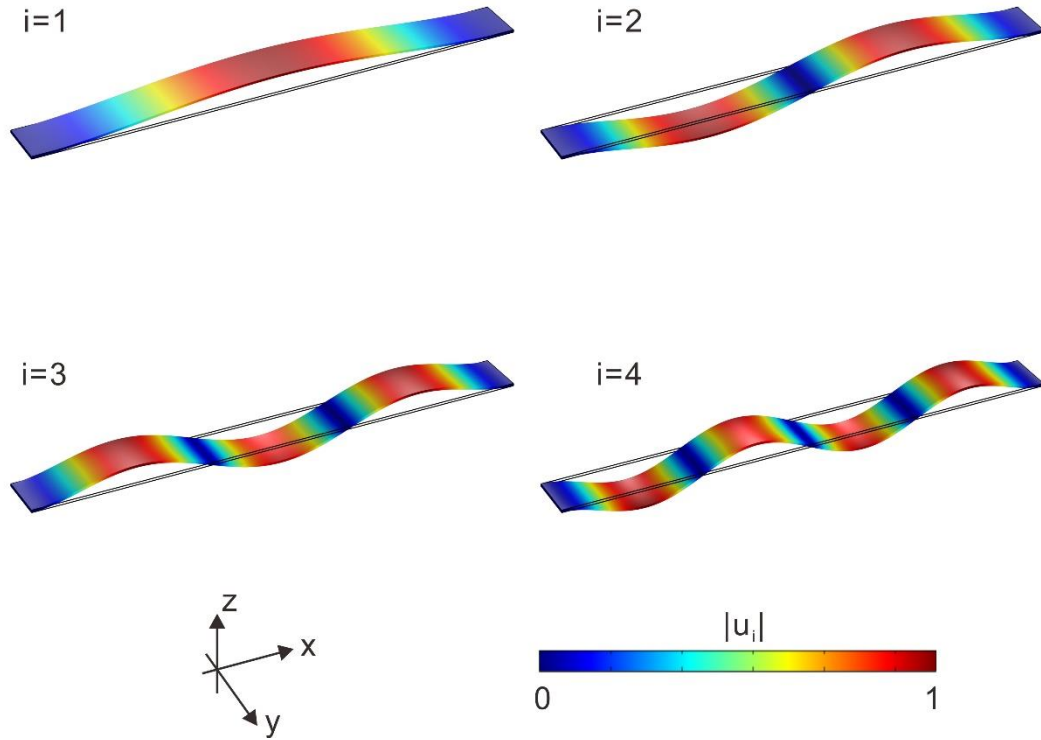
Fig. 5.2: Transverse vibration modes (lowest four modes) of the double clamped beam model obtained via COMSOL Multiphysics. The color scale is proportional to the deformation amplitude |u_i|, normalized to the unity.

5.3 Experimental implementation of frequency-tunable oscillator

As in the previous chapter, stripe-like nanomembranes with embedded QDs are bonded on a micro-machined piezoelectric actuator, forming a double-clamped beam mechanical resonator. With the introduction of a bias tee, both an alternating current (AC) voltage (acting as the mechanical driving force) and a direct current (DC) voltage (adjusting the hydrostatic axial stress) can be simultaneously applied to the PMN-PT actuator. The chosen arrangement not only guarantees a strong intrinsic coupling between actuator and mechanical resonator but also allows the resonant frequencies to be reversibly tuned through different uniaxial stresses.

A sketch of our device is shown in Fig. 5.3 (a). There is a small gap (usually the distance ranges from 20~60 μm, as shown in Fig. 5.3 (b)) between the "two fingers" of the PMN-PT actuator and the suspended stripe-like nanomembranes lie on the gap. A voltage is applied between the bottom and top (ground) of the actuator. The induced electric field will lead to a deformation of fingers, which will induce uniaxial stress to the nanomembranes. Since the total length of the fingers (3.0 mm) is much larger than the gap width, strain is strongly amplified. In addition, here we keep the same length of fingers in order to avoid in-plane displacement of QDs arising from the stress.

To ensure that the QD emission is affected by transversal oscillations, the QD layer is displaced from the center of the membrane. Specifically, the membrane structure comprises the following layers (from bottom to top): 100 nm Au, 10 nm Cr, 127.4 nm

GaAs, In(Ga)As QDs and 127.4 nm GaAs. During an oscillation period the QD will be alternatively subject to compressive and tensile strain, leading to an oscillation of the transition energy with an amplitude $2\delta\omega$ (see Fig. 5.4).
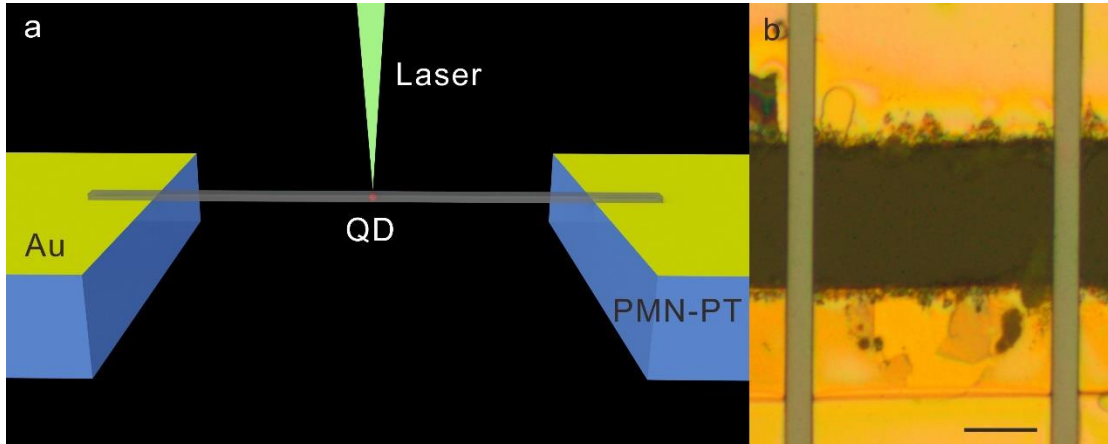
Fig. 5.3: (a) Sketch of the quantum dot embedded in a mechanical resonator. QDs are embedded in stripe-like nanomembranes with both sides bonded to the PMN-PT actuator. (b) Micrograph showing two membranes. The scale bar corresponds 30 μm.

.

74
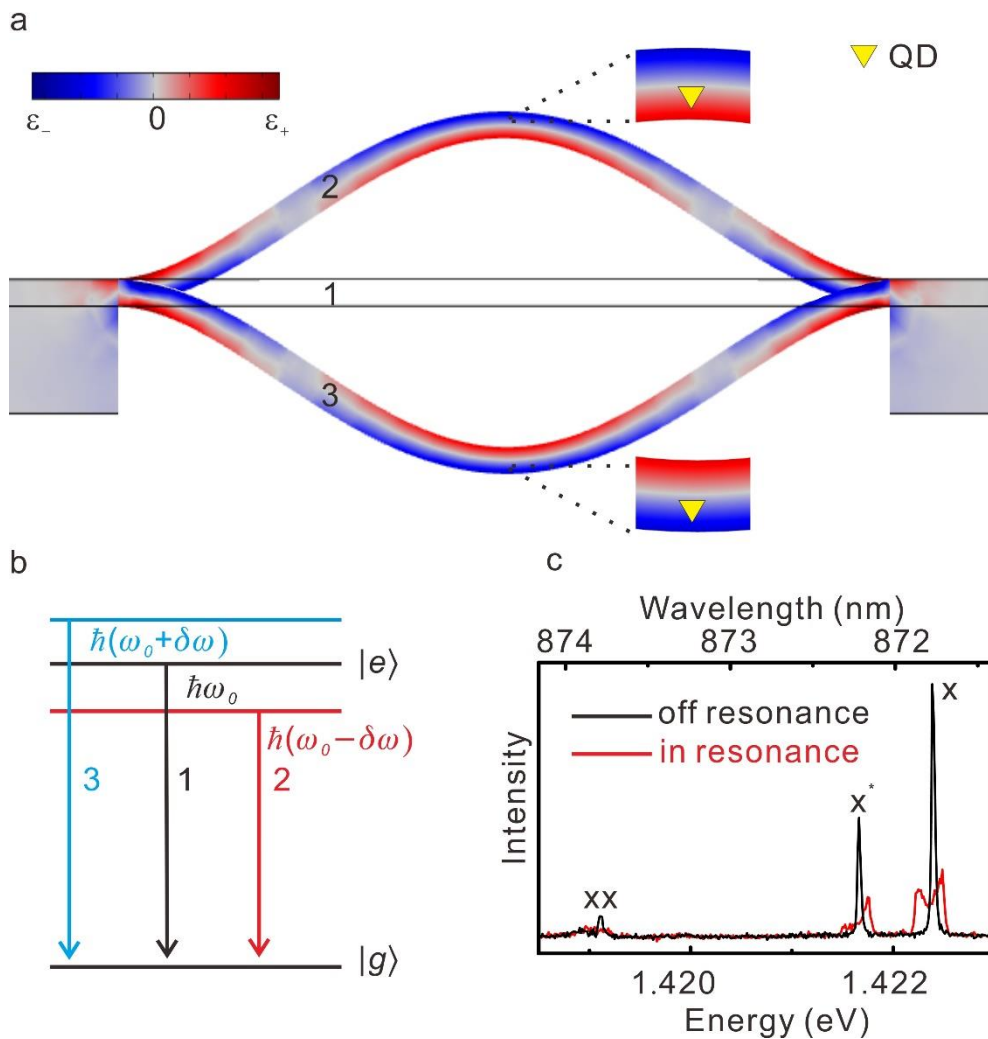
Fig. 5.4: (a) Sketch map of the nanomembrane deformation in the first-order transverse vibration mode. The hydrostatic strain field is plot in blue-to-red scale (blue: compression, red: tension). 1 is the static state, 2 and 3 are the typical states when the QD experiences tensile and compressive strain. The yellow inverted triangles indicate the QD. (b) Energy level diagram of QD in static states (1), under strain fields (2, 3), the strain fields shift the transition energy by $-\hbar\delta\omega$ and $+\hbar\delta\omega$. (c) Typical QD PL spectrum off (black) and in (red) mechanical resonance.

The whole experimental setup is shown in Fig. 5.5. In order to collect the photoluminescence (PL) signal, the device shown in Fig. 5.3 is mounted in a liquid-helium-flow cryostat that can be cooled to a cryogenic temperature below 10 K. A continuous-wave (cw) laser with wavelength of 532 nm was employed as the optical excitation source, the PL signal emitted from QDs is collected by a 50× objective with numerical aperture 0.42. After passing through a long-pass filter to block the laser, the signal is introduced into a spectrometer equipped with an 1800 *groves/mm* grating and liquid-nitrogen-cooled silicon Charge-Coupled-Device (CCD). To study the time-resolved PL evolution, an avalanche photodiode (APD) is employed. In this case, a mirror is used to send the signal to the APD and the spectrometer acts as a monochromator. Mechanical oscillations of the nanomembranes are excited by AC signals provided to the PMN-PT actuator. As mentioned before, a static uniaxial stress can be simultaneously applied by adjusting the DC voltage applied to the actuator
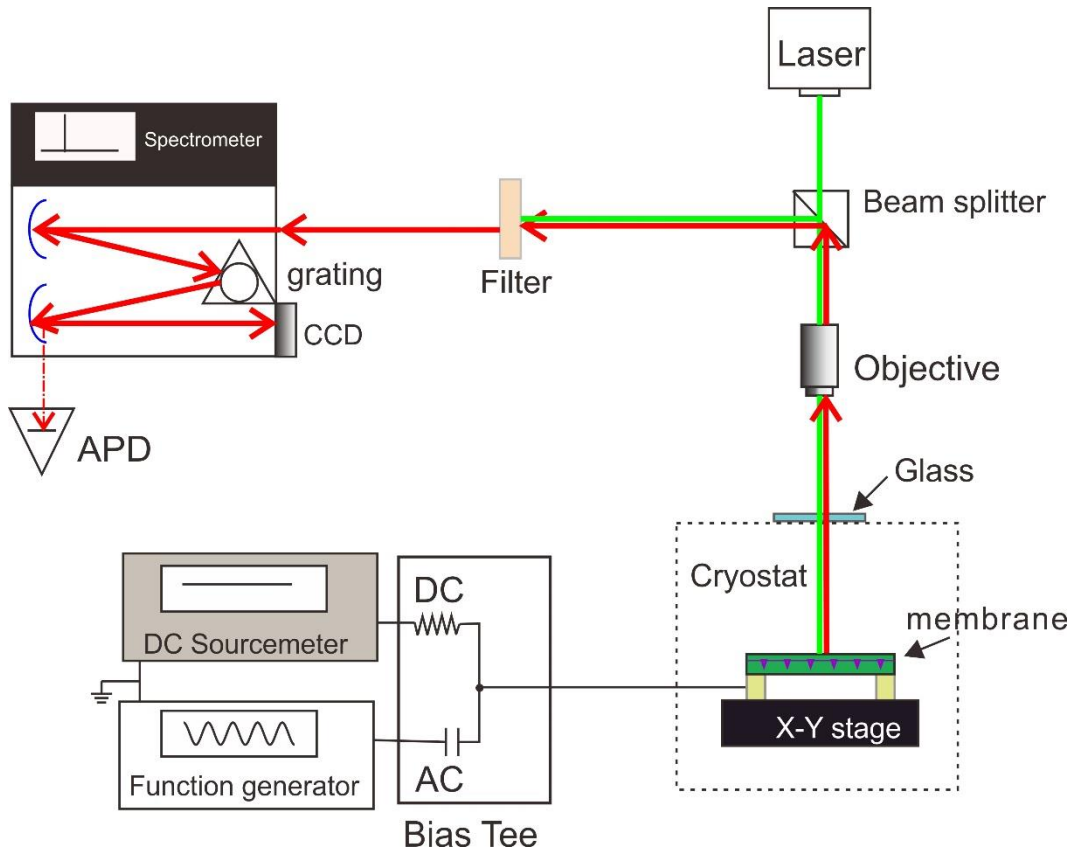
Fig. 5.5: Schematic diagram of experimental setup: DC sourcemeter and function generator are employed to apply DC and AC signals to the PMN-PT actuator. The PL signal, dispersed by a grating spectrometer, is collected either by a CCD camera or by an avalanche photodiode (APD).

5.4 Opto-mechanical behavior of beam oscillators

As mentioned above, strain will produce an energy shift of the QD emission. For oscillations with small amplitude we can assume that the energy shift is proportional to the local strain. In time-integrated PL spectra, such as those shown in Fig. 5.4(c), oscillations produce broaden emission lineshapes. We first fit this broaden emission lineshpes with a time-integrated Lorentzian equation[169,170], which a strain modulated energy shift $\Delta E$ can be extracted, then we quantify the amplitude of the oscillations with ΔE. Fig. 5.6 (a) shows one of the resonances and its evolution with varying driving amplitude. Here the trion emission line of a QD is chosen because of its relatively sharp linewidth (full width at half maximum (FWHM) of 29 μeV, corresponding to the resolution limit of the used setup) and relatively high intensity. An example of data used to generate Fig. 5.6 (a) is shown in the inset, which present PL spectra collected for different driving frequencies with a driving amplitude of 100 mV. At lower driving amplitude the lineshape of the resonance is symmetric and has a quality factor between 5500 and 6500.

With increasing driving amplitude, the peak becomes more asymmetric and shifts to lower frequency. This shark-fin shape can be attributed to the onset of nonlinear behavior, which can be modelled with a Duffing oscillator model[171]. In this model, the restoring force takes the form: $\alpha x + \beta x^3$, in which x stands for the displacement, α is the linear stiffness parameter and β is the non-linear parameter in restoring force. The cubic term becomes important at sufficiently large excitation forces.

In order to exclude non-linear effects and investigate the tuning of the resonance frequency, a smaller driving amplitude of 25 mV is used. The resonance evolution with different DC voltages (tensile stress) is plot in Fig. 5.6 (b). With increasing tensile stress, the PL emission shows a redshift. At the same time, the resonance frequencies (marked by red dashed circles) increase with the increasing tensile stress, which follows the rising tendency of equation (5.11). However, due to the limited hydrostatic axial stress applied, no clear $f \propto \sqrt{\sigma}$ dependence can be observed. Although the frequency tuning shown in Fig. 5.6 (b) is not large (~0.46%, from 2.772 MHz to 2.785 MHz), the axial strain we applied here is also moderate (below 0.1%). Since the actuator is capable of strains of up to ~2%, much larger tuning ranges could be in principle achieved.

The reason for the limited tuning range shown here is that in several attempts resonances disappeared during the experiment, so that we were not able to follow them systematically. A possible explanation is that some irreversible structural change occurred (for instance a structural change of the bonding layer or detachment of particles present on the membrane). Fabrication imperfections also prevented a quantitative comparison of calculated and measured resonance frequency positions. For possible further experiments, the bonding and cleaning procedures should be therefore improved.
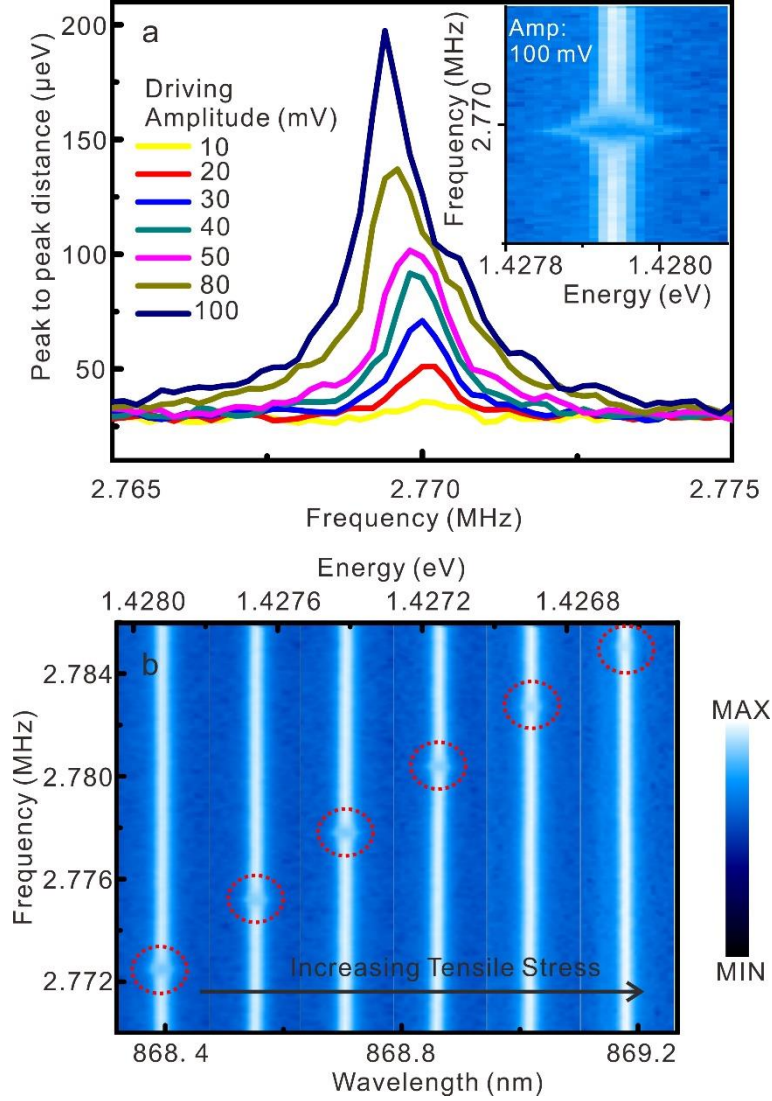
Fig. 5.6: (a) Variation of the width of the PL emission of a trion confined in a QD as a function of driving frequency and with different driving amplitude of the AC voltage applied to the piezoelectric actuator. The DC voltage is kept at 0 V (no external static stress is applied through the PMN-PT actuator). Inset represents color-coded PL spectra of the trion emission as a function of driving frequency with 100 mV driving amplitude. (b) Frequency-resolved PL spectra of trion emission with different tensile stresses. From left to right, the DC voltage is 0 V, 10 V, 20 V, 30 V, 40 V, 50 V. The driving amplitude (AC) is kept at 25 mV.

For possible applications of the oscillator (e.g. for g-tensor modulation), higher operation frequencies than those shown in Fig. 5.6 will be required. In spite of the bulky structure of the actuator employed here, we searched for high-frequency resonances.

Fig. 5.7 (a) shows the time-integrated spectrum for a resonance at a frequency of 19.75 MHz and an AC driving voltage of 1.9 V. To study the oscillations in the time-domain we have performed series of time-resolved PL measurements using an APD. The general measurement procedures are as follows: first we choose a mechanical resonance, indicated by line broadening in time-integrated PL (here we chose a trion emission line), then a monochromator was used to select emission at several particular

wavelengths and the photons were detected by an APD with the time correlated counting electronics triggered by the RF function generator. The APD counted the photons at each specific wavelength within the RF period. Lastly, we collected all the data (three demensional matrix of wavelength-time-photon count) and plot a color-mapped time-resolved QD emission shift under mechanical resonance, An example of result is shown in Fig. 5.7 (b). For this experiment a square pulse wave (generated by a Keysight (Agilent) Technologies 81134A Pulse Pattern Generator), instead of a sinusoidal wave, was employed as the mechanical excitation source.

Due to the limitations of the available function generator, the maximum resonant frequency we observed was around 61.5 MHz, the time-resolved PL spectra are shown in Fig. 5.7(c). We note that in this experiment the rate at which the emission energy shifts exceed values of 50 µeV/ns. Taking into account that the typical lifetime of the excitonic transitions in the used GaAs QDs is of the order of 250 ps and the corresponding natural linewidth is 2.3 µeV, this means that the strain modulation produces energy shifts of the order of 5 times the natural linewidth during the lifetime of the exciton. As strain also changes the excitonic fine-structure splitting, this speed may be already sufficient to observe non-trivial phenomena, such as Landau-Zener transitions[172,173].
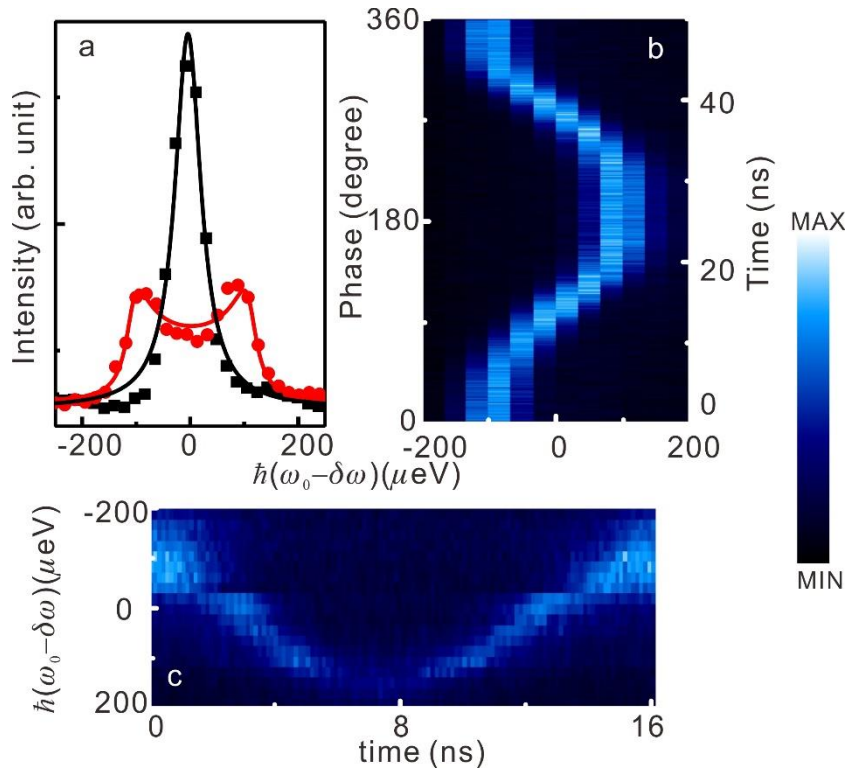
Fig. 5.7: (a) Comparison of the PL Spectra of the trion emission when the mechanic frequency applied out of (open squares with black line) and in (filled squares with red line) resonance with the mechanical mode. Time-resolved PL evolution at (b) 19.75 MHz and (c) 61.5 MHz.

5.5 Conclusion and outlook

In summary, we have investigated here the possibility of using microprocessed piezoelectric actuators to drive oscillations in micromechanical resonators consisting of semiconductor nanomembranes with embedded QDs. By combining the AC voltage used for excitation with DC voltages, the resonance frequencies can be tuned in-situ through the tensile stress provided by the PMN-PT actuator. Furthermore, through the time-resolved PL measurement of QDs, we confirmed the feasibility to modulate the transition energies on timescales faster than the excitonic lifetime, opening the way to interesting experiments on two-level systems with time-varying energies.

One of the disadvantages of our hybrid device lies in the mechanic resonator. In principle, the resonances should be well-resolved, as discussed in section 5.2. However, the resonance frequencies in our device show no sign of deterministic, which may arise from frowsy integration between the membrane and PMN-PT. Compare to the monolithic device[160,174], the SU8 adhesion layer is a poor medium to effectively transfer the strain. In addition, some residue particles (which can be found in Fig. 5.3 (b)) from the SU8 and by-product of chemical etching will make some non-negligible effect on the effective mass of the membrane[161,175], which definitely will alter the resonant frequencies and decrease the Q-factors, further restrict the optomechanics engineering. Considering the most promising application to use the hybrid device as transducer for quantum information, the hybrid interaction rate should be comparable to decoherence time of the quantum system to the local environment[176,177], high vibration modes (higher frequencies) and large optomechanical coupling parameter are needed. However, all of this get stuck with the chaotic vibration modes in the present device. So a hybrid device with deterministic resonant frequencies should be fabricated in the next step, or some other mechanical excitation method (such as SAWs) should be adopted.

6. Quantum dots manipulation with surface acoustic waves[VII]

6.1 Motivation to manipulate QDs with SAWs

In the previous chapter, a promising QD-mechanical resonator hybrid system was described and its tunability was demonstrated. However, several issues still exist through the straight strain modulation from the piezoelectric actuator: the mechanical coupling between actuator and semiconductor resonator turned out to be little predictable and high mechanical frequencies (in the GHz regime, needed to achieve the quantum coherent coupling to the QDs) may be challenging unless the piezoelectric actuator is miniaturized.

SAW technologies have been thoroughly developed over several decades[178]. Definitely, it would be an advantageous method to manipulate the QDs with SAWs: a monolithic device with robust and stable SAWs coupling can be monolithically fabricated since GaAs is piezoelectric material, and SAWs in GaAs have been thoroughly investigated.

Although QDs emerged as a leading single photon source for much impressive progress being made during the past decade, the dephasing and resulting indistinguishability reduction of emitted photons is a long-term obstacle for QDs being the ideal single-photon source[179,180]. Considering the solid-state nature of QDs, several elements could lead to the reduction of photon coherence and decrease the indistinguishability level[181–183]. Phonons are commonly believed to play complex but vital roles to the decoherence properties of photons emitted by QDs[153,154,184]. It would be thus desirable to control and manipulate the phonons and their interaction with excitons confined in QDs as will. Analogous to photonic structures, phonons can be engineered via designed phononic structure. Thus with the integration of photonic structure and phononic structure to the QDs, a fully on-chip hybrid optomechanical system can be realized via the independent manipulation of light (photons), sound (phonons) and matter (excitons)[170].

Although many excellent works on the combination of SAWs and QDs have been done, most of the works are still limited on Rayleigh waves[116,119,185], basic research work on the QDs reaction to phononic structures need to be done. In this chapter, we will make a systematic study of the behavior of QDs located in a basic waveguide with SAWs.

6.2 Device design and experimental implementation

In order to make a systematic study of the sound wave propagation properties and make a comparison with the usual Rayleigh waves, a new device is designed and fabricated. The sketch of the whole device is shown in Fig. 6.1 (a). An IDT is placed on one side of the sample, the IDT's fingers are aligned to be perpendicular to the [110] direction on the (001) GaAs surface. Along this direction the piezoelectric coupling is maximum and employed to generate SAWs. A signal generator is connected to the IDTs- to apply a radio frequency voltage to the interdigital comb electrodes. Thus the (Al)GaAs material will deform underneath the comb fingers. The sample we used consists of three main layers: GaAs substrate, (Al)GaAs sacrificial layer and a second (Al)GaAs layer of lower Al-content with QDs embedded in its center. With this kind of structure, suspended beams can be fabricated through a series of processing steps (the details will be introduced later). In this work, two regions are mainly studied: the bulk material area (marked with red dashed line) and the suspended area (marked with white dashed line). The geometry of the suspended beams studied here can be seen in the scanning electron microscope (SEM) image in Fig. 6.1 (b). These beams possess the same width but different lengths. In the SEM image, the suspended areas of all three beams are clearly visible.
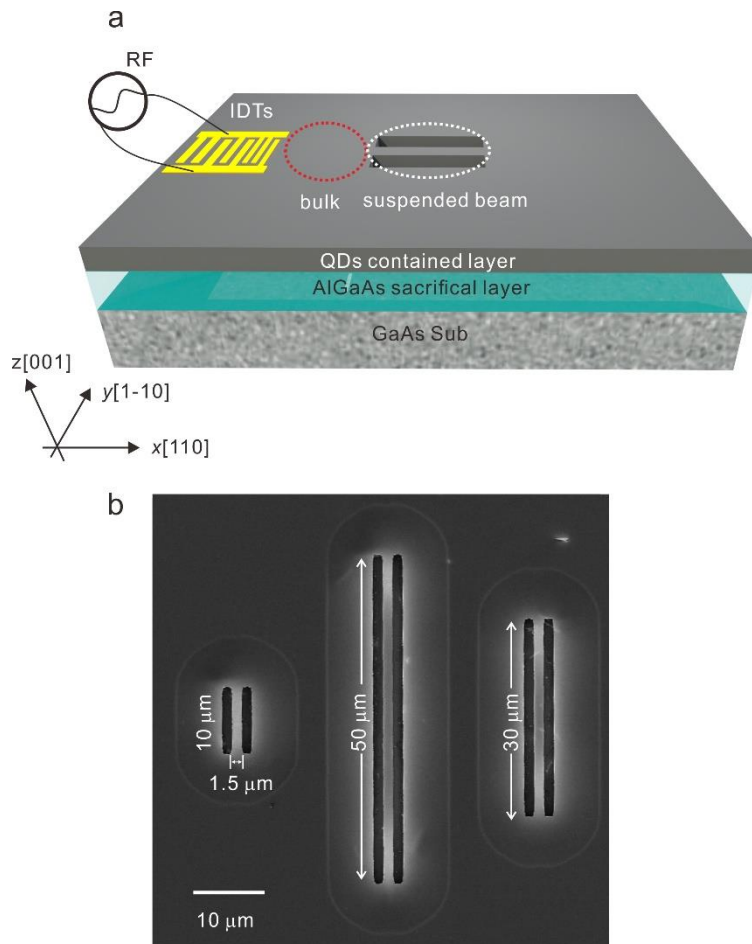
Fig. 6.1: (a) Sketch of the device in our work, the coordinate system corresponds to the crystal orientation of cleaved GaAs. (b) SEM image of the suspended beams studied in this chapter, the widths of them are all 1.5 μm and the lengths are 10 μm, 50 μm, and 30 μm.

The sample used here (AS275) contains GaAs QDs grown with the droplet etching method. The detailed structure of the as-grown sample is illustrated in Fig. 6.2 (a), which is the same as the "bulk" area shown in Fig. 6.1 (a). The sample comprises GaAs substrate, 1.2 μm $Al_{0.75}Ga_{0.25}As$ sacrificial layer and the layer with embedded QDs. The GaAs QDs are sandwiched by 75 nm and 77 nm $Al_{0.4}Ga_{0.6}As$ layers, with 4 nm GaAs capping layer on the top and bottom sides. In the "suspended beam" area, only the layer containing the QDs is left. Two types of GaAs QDs exist in our sample: one comes from the deposition of GaAs on the surface of the AlGaAs layer (type I), where residual roughness induces the unintentional localization of excitons, giving rise to "natural QDs"; the other one is formed by the GaAs filling to the nanoholes etched by Al droplet (type II). A typical PL spectrum of the sample is shown in Fig. 6.2 (c). Because of the difference in forming mechanisms, these two types QDs show different properties. First of all, the type II QDs have larger sizes compare to type I, as indicated in Fig. 6.2 (c), the PL emission of type 2 is usually located from 775 nm to 800 nm, while the type I QDs emit around 680~730 nm. Secondly, the density of type I is much higher than type II, which is also apparent from Fig. 6.2 (c).
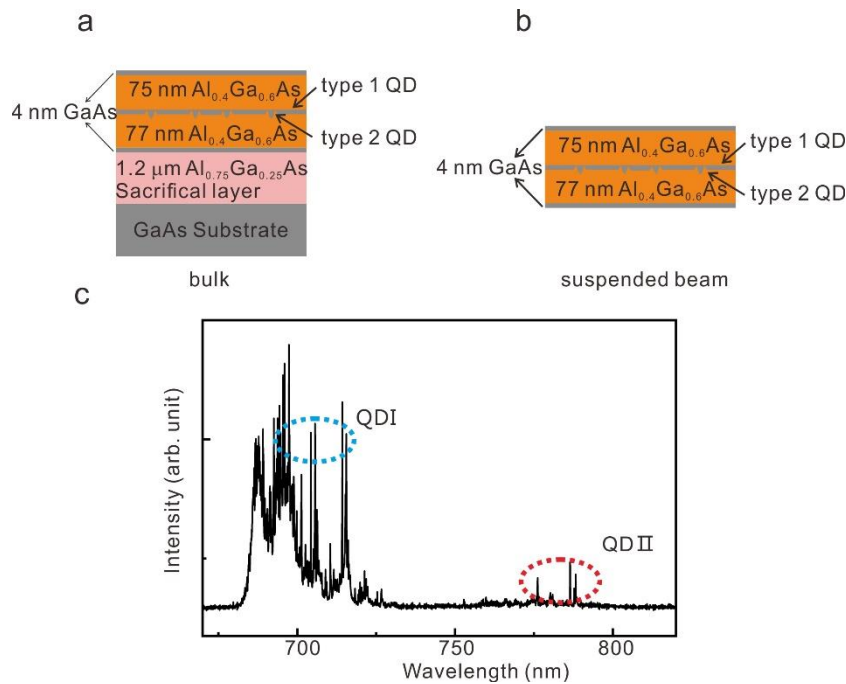
Fig. 6.2: Sample structure of (a) bulk and (b) suspended beam area. Besides intentional dots obtained by droplet etching (type II), thickness fluctuations in the 2-nm-thick GaAs quantum well induce "natural QDs" of type I. (c) Typical PL spectrum of the sample we used in this work, QDⅠ,Ⅱ are marked.

The device processing was performed by Matthias Weiß at the "Lehrstuhl für Experimentalphysik 1", University Augsburg, and the whole processing flow is

presented in Fig. 6.3. To illustrate the steps, the view is chosen to be perpendicular to (110) plane. The processing proceeds as follows: after proper cleaning, the sample was spun with photoresist and electron beam lithography (EBL) was employed to write the pattern. After development, the sample was inserted into the chamber of a Reactive-Ion Etching (RIE) system, the remaining photoresist was used as mask. A RIE dry etching step was performed down to the (Al)GaAs sacrificial layer. After that, the sample the photoresist was removed. Later the sample is immersed in a 20% HF solution for 20 s to make the undercut etching of the (Al)GaAs sacrificial layer. Then supercritical drying was performed in order to avoid the collapse of the suspended area after the cleaning of the residue of HF. Lastly, plasma cleaning was carried out to clean the residues, which may come from the remnant resist or hydroxide of aluminium[175].
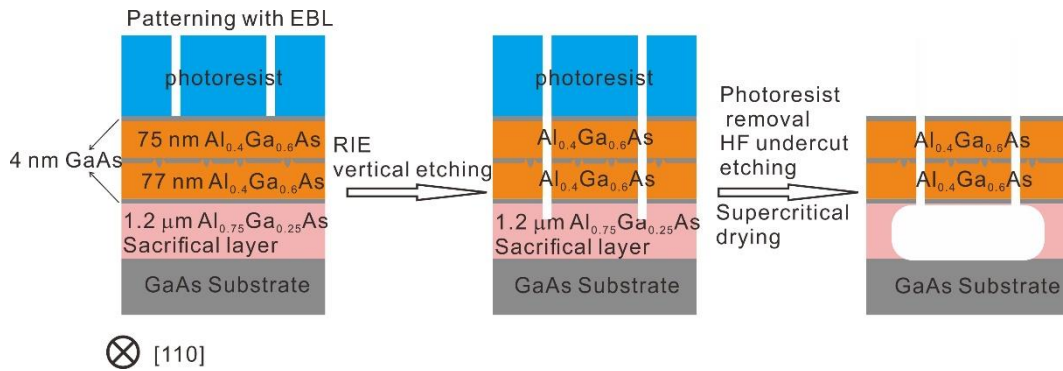
Fig. 6.3:   Schematic flow chart of the processing steps for the studied device. The view is perpendicular to the (110) plane. The device was fabricated by Matthias Weiß at University Augsburg.

6.3 FEM simulation of SAWs interaction with QDs

Due to the different materials contained in the multilayer structure, we use the software COMSOL Multiphysics to analyze the propagation of SAWs (frequency-velocity relations, strain field, electric field, etc.) in our structures.

6.3.1 Simulation of Rayleigh waves

First, we consider Rayleigh waves. The setting and boundary conditions is briefly described in Section 3.4. In this simulation, only a single unit cell is considered: its width is set to one SAW wavelength (λ_{SAW}) and the depth of the unit cell is set as three times of λ_{SAW}, since the Rayleigh waves decay exponentially with the distance from surface (usually limited to one wavelength). The two side edges are set as periodic boundary conditions with the middle line as antisymmetric axis. Then we set different wavelengths, make a parametric sweep for searching the eigenfrequencies. With this method, we can obtain the dispersive frequency-velocity relations, the result of our sample is shown in Fig. 6.4 (a). Inset of Fig. 6.4 (a) show the hydrostatic pressure and electric potential. Here we point out that these mechanical and electric properties scale linearly with the SAWs amplitude, so the absolute value is not critical. These simulations clearly show the surface-confined mode of the Rayleigh waves. Fig. 6.4 (b)

is the total displacement u_{total}, longitudinal displacement u_x and transverse displacement u_z of the QDs along the propagation [110] direction. As introduced in Section 2.3.2, for a Rayleigh wave a lattice site follows an elliptical trajectory, which is indicated by the $\pi/2$ phase difference and amplitude difference of d_x and d_z. The calculated electric potential ϕ is plot in the inset of Fig. 6.4 (a) and the longitudinal and transverse electric fields E_x and E_z with x position are in Fig. 6.4 (c). Here the electric fields at the QDs positions from the longitudinal and transverse components reflect again the $\pi/2$ phase difference.
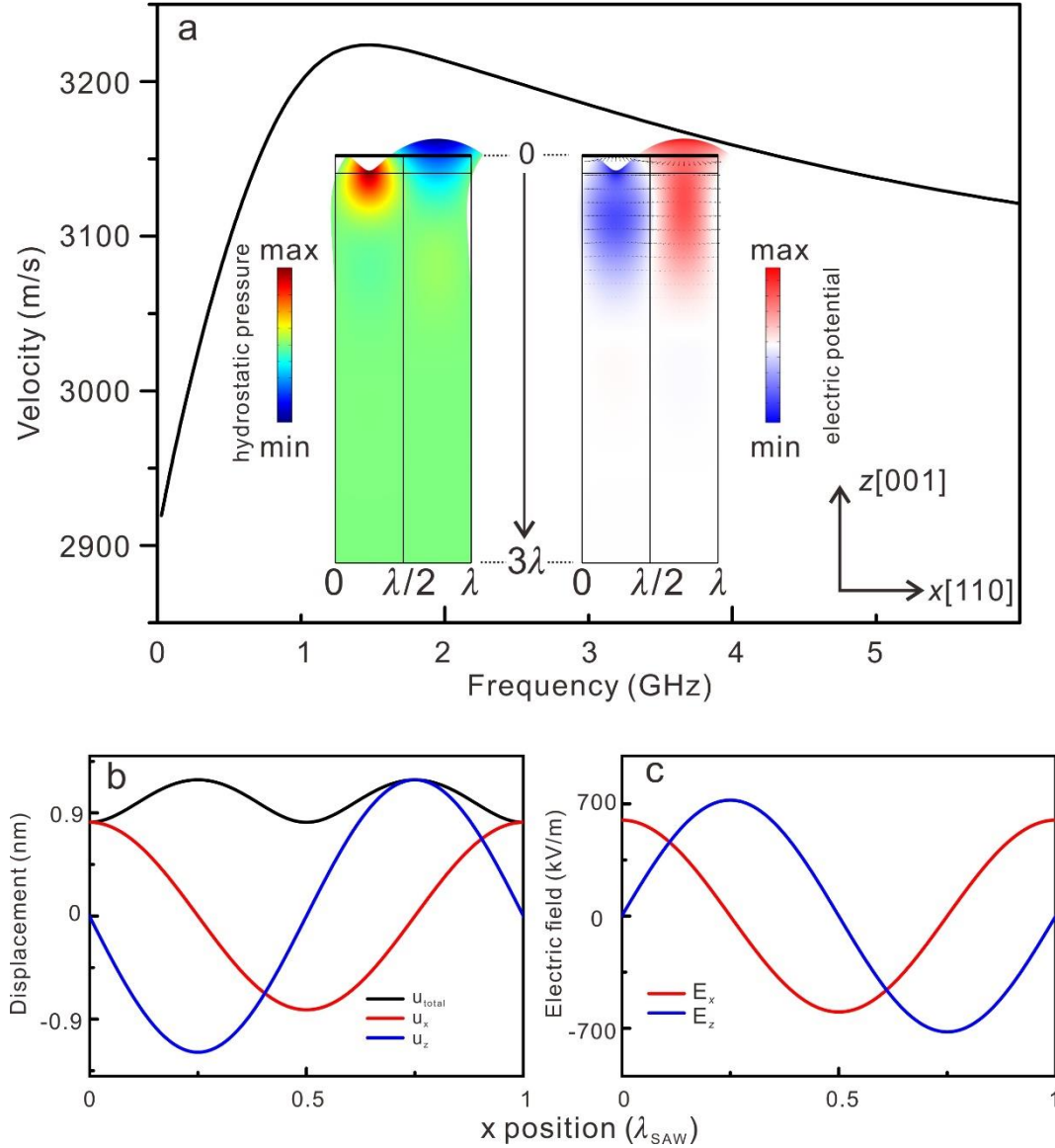
Fig.6.4: (a) Calculated velocity dependence with frequency when SAWs are propagating along the [110] direction of the sample AS275. The inset shows the mechanical and electric properties of the unit cell of the sample with the interaction of SAWs. The [110] direction is defined as x-direction while [001] direction is defined as z-direction. The extracted displacements components (b) and electric fields components (c) at the QD position.

6.3.2 Simulation of Lamb waves

With regard to the Lamb waves, the settings for FEM simulation are similar, the difference is that now the layer containing the QDs is suspended. Because of the lack of a bottom matter-vacuum interface, the solutions corresponding to Lamb waves is significantly more difficult to indentify than that of Rayleigh waves. According to the brief introduction to Lamb waves in Section 2.3.4, there are two types of solutions, which correspond to the symmetric and antisymmetric (flexural) modes (shown in Fig. 6.5 (a)). If we go back to the equation (2.41) and (2.42) for the two modes, the allowed values of velocity will emerge for a given value of angular frequency w. Fig. 6.5 (b) shows the velocity dispersion curves of Lamb waves propagating in a suspended beam of the AS275 sample. For moderate frequencies (<15 GHz), only a single symmetric and a single antisymmetric (flexural) modes exist, referred to as the fundamental modes, labeled as S_0 and A_0. As the frequency increases, additional new modes (labeled as S_n, A_n according to their order) appear. In our work, we focus exclusively on the low-frequency range to exclude the high order modes. The fundamental modes S_0 and A_0 have distinct velocities, which is also helpful to distinguish them.
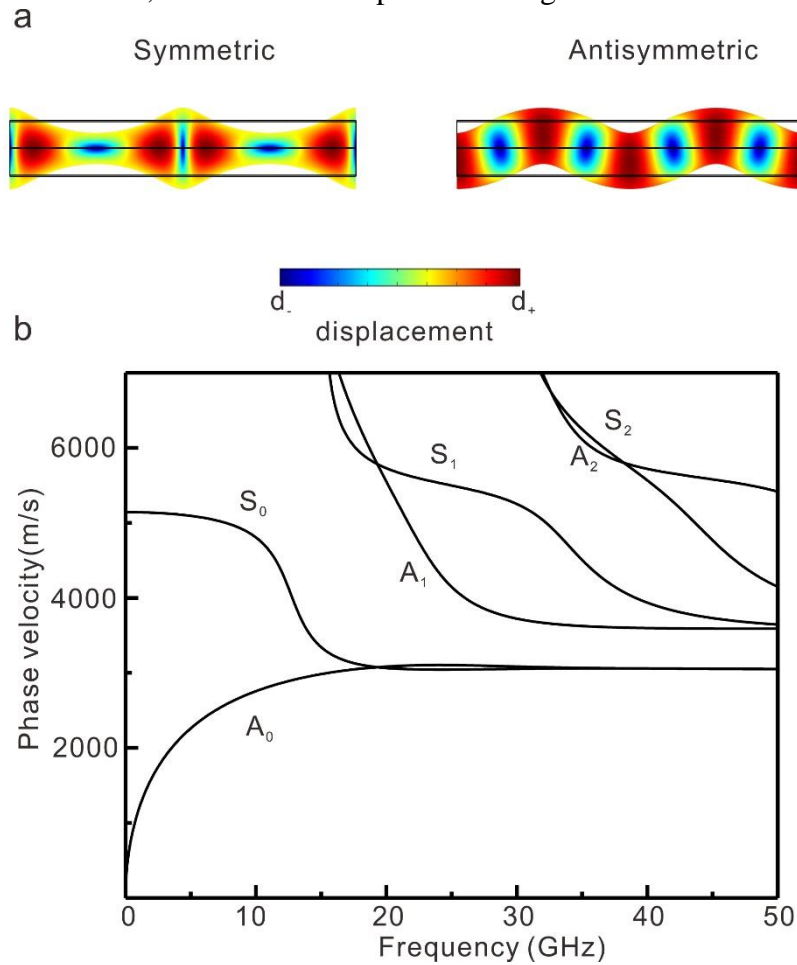
Fig. 6.5: (a) Calculated profile of symmetric and antisymmetric Lamb waves. (b) Calculated phase velocity relations with frequency. A indicates antisymmetric modes and S symmetric modes.

6.4 Experimental data and analysis

After the theoretically analysis, we now move to the experimental results. The first element to consider is the IDTs used to generate a SAW to be after a free propagation distance coupled into the suspended membrane. In this work, we employ wide passband IDTs, which have the same design with the ones in Ref[185]. A schematic picture of the IDTs is illustrated in Fig. 6.6 (a), this IDT is designed based on a split-52 configuration, the $\lambda(x)$ is the wavelength of the generated SAW fulfilling the relation $2p(x) = \lambda(x)$, with p the fundamental periodicity of the IDT. With this split-52 configurations, usually one fundamental resonant frequency $f_{SAW,1}$ (Here $f_{SAW,1} = 250$ MHz) and three overtone harmonic frequencies $f_{SAW,n}$ exist. By introducing a linear variation of the fundamental periodicity

$$2p(x) = \lambda(x) = \lambda_0 + \alpha x, \tag{6.1}$$

with α is the dimensionless chirp parameter, the IDT resonance can be expressed as

$$f_{SAW,n} = \frac{n v_{SAW}}{\lambda(x)} = \frac{n v_{SAW}}{(\lambda_0 + \alpha x)} \tag{6.2}$$

Hence with the introduction of a chirp, broadened resonances will be obtained. Fig. 6.6 (b) shows the SEM image of this wide passband IDT, and the variation of the periodicity of the IDTs can be clearly seen from the enlarged picture of the IDTs at left and right panels. More details about the design and parameters of this IDTs can be found in Ref[185].
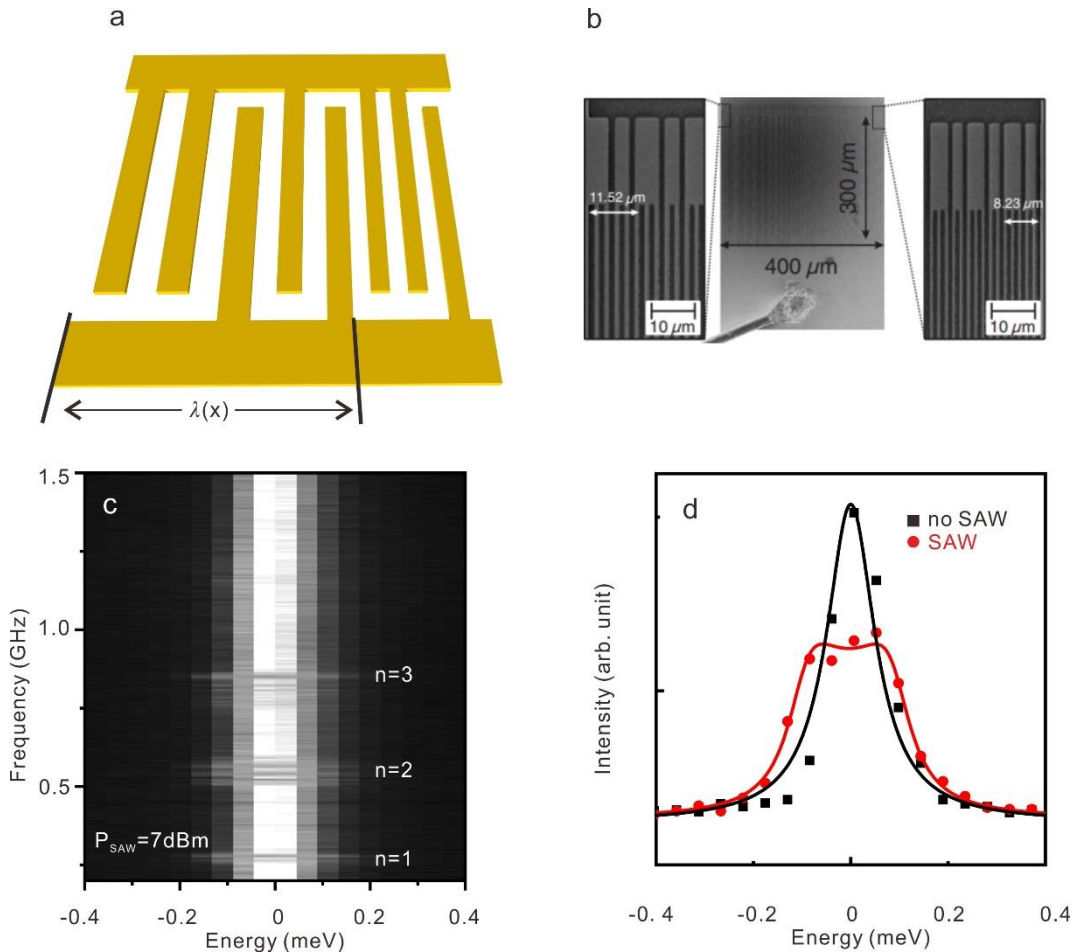
Fig. 6.6: (a) Schematic picture of a patterned metal IDT used in this work. λ indicates the wavelength of the SAW. (b) SEM image of the IDTs, the left picture represents a region used to generate long wavelengths and the right short-wavelengths. Adapted from[185]. (c) False color plot of the frequency scan of the PL emission of a single QD. The characteristic frequency bands for IDTs are marked as n=1, 2, 3. (d) PL spectra of emission from QD with and without SAW. The solid lines are fitted with a Lorentz function (black) and the equation (6.3) (red).

We characterized the passbands of the fabricated IDTs by frequency-resolved PL spectra of QDs in the bulk area, which is presented in Fig. 6.6 (c). If the frequency corresponds to a resonance, periodical strain field (and electric field) from the SAW will be applied to the QDs, a periodical emission energy shift will occur. Since here the acquisition time for PL is much larger than the period, abroadened PL peak will be observed. If the frequency is not in resonance, the input power will be reflected by the IDT and no SAW will propagate to the QDs, thus in principle the PL peak keeps the same. From the plot of Fig. 6.6 (c), we observe the fundamental resonance and the first two harmonic resonances. Furthermore, these resonances show relatively wide passband, especially the first harmonic one. Fig. 6.6 (d) shows the typical Lorentzian emission peak of QDs and the emission modulated by SAWs. Assuming a harmonic modulation, the time-integrated broadening peak can be fit by the[169,185]

$$I(E) = I_0 + f_{SAW} \frac{2A}{\pi} \int_0^{1/f_{SAW}} \frac{w}{4(E-(E_0+\Delta E\cdot\sin(2\pi f_{SAW}t)))^2+w^2} \, dt, \qquad (6.3)$$

where A is the integrated intensity without SAW and *w* is the linewidth without SAW, E_0 is the unperturbed energy and ΔE is assumed as the energy shift induced by the SAW. The solid line in Fig. 6.6 (d) is the fit according to the equation (6.3).

After confirming that the IDT used in this work is capable of generating SAWs at different frequencies, we switch to the suspended beam, which is the core of this study. According to the previous analysis, two main types of Lamb waves are expected in the suspended beam (because the thickness of the beam is much smaller than the sound wavelength, see section 2.3.4). Here, we only explore the low-frequency range (200 MHz < f < 1000 MHz) in which only two fundamental modes (A_0 and S_0) propagate in the suspended beam. Fig. 6.7 (a) is the typical cross section color plot of the calculated displacement in our device at a specific time. We assume an ideal condition in this case: no attenuation in the suspended beam; the suspended beam has infinite length so that there is no reflection and related interference. When the sound waves propagate in bulk materials, only Rayleigh waves propagate. In contrast, when it reaches the bounadary to the suspended beam, the Rayleigh wave is converted to Lamb waves, potentially as a superposition of antisymmetric and symmetric modes. After injection, the antisymmetric and symmetric modes will gradually separate over time because of the velocity difference. Fig. 6.7 (b) is the calculated wavelength-frequency relations of the Rayleigh wave, antisymmetric and symmetric Lamb waves. In the frequency range between 200 MHz and 1000 MHz, the symmetric modes shows much larger wavelengths compare to the antisymmetric mode. Similar to an optical waveguide, a cut-off wavelength exists in the acoustic waveguide. By optimizing the width of the suspended beam, it is possible to suppress the propagation of symmetric

mode. With the width w of 1.5 μm (cut-off wavelength $\lambda_{cut-off} = 2w = 3$ μm) of the suspended beams, only waves which possess wavelength shorter than 3 μm can effectively propagate through the suspended beam. Based on the extracted wavelength-frequency relation results shown in Fig. 6.7 (b), the symmetric mode can not propagate in the frequency range between 200 MHz and 1000 MHz.
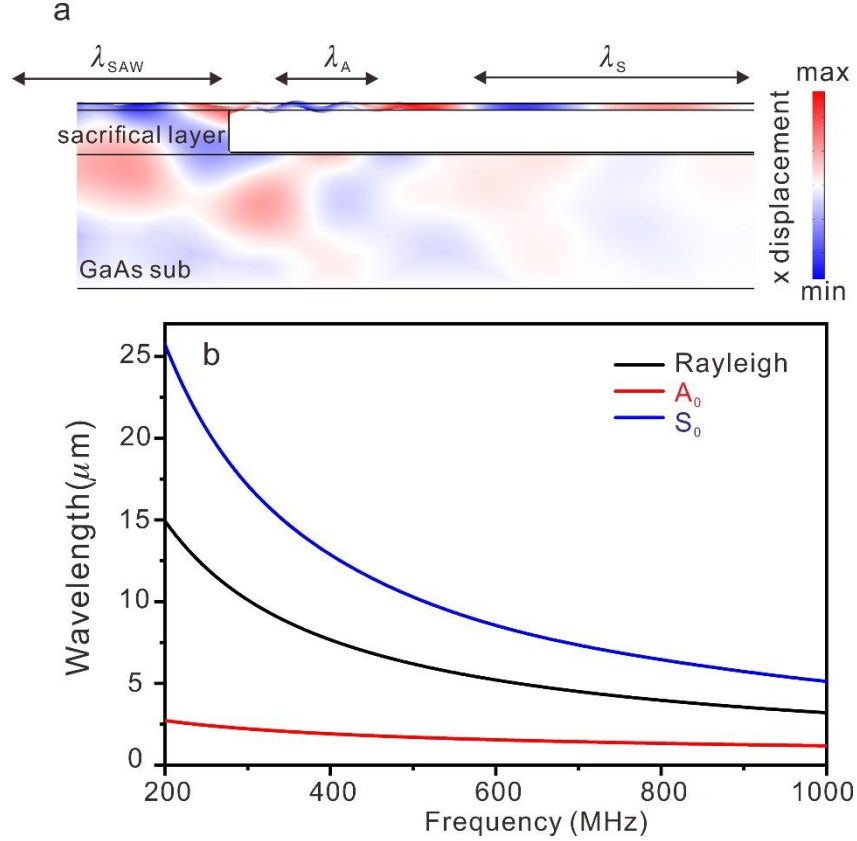
Fig. 6.7: (a) Color plot the propagation of sound waves in our sample in the ideal case of no attenuation and no reflection. Adapted from [186]. (b) Extracted wavelength-frequency relations of the Rayleigh, Lamb waves (A_0 and S_0 are the fundamental antisymmetric and symmetric mode, respectively).

After confirming the different propagating wave modes between the bulk area and suspended beam area, it is important to make a comparative study on the corresponding optomechanical coupling effect between them. A qualitative comparison of the optomechanical coupling effect in membrane between Rayleigh wave and Lamb wave is illustrated in Fig. 6.8. The experimental configurations are schematically shown in Fig. 6.8 (a), an IDT-generated SAW (with a frequency of 260 MHz and 7 dBm power) propagates from left to right. Here, we select two QDs, which are located in the bulk area and inside suspended beam, respectively. According to the analysis above, these two QDs were modulated by the Rayleigh wave and Lamb wave, respectively. And the time-integrated emissions of these two QDs without and with Rayleigh/Lamb wave applied were plot in Fig. 6.8 (b) and (c), with the center energy of unperturbed QDs' emission being a reference. Remarkably, the spectral broadening induced by the Lamb wave is clearly enhanced compared to that by the Rayleigh SAW. The extracted spectral broadening ΔE from the Lamb wave ($\Delta E_L = 1.46$ meV) is about three times of the one

(ΔE_R=0.485 meV) induced by Rayleigh wave, which further confirms a stronger modulation from Lamb wave, and more investigation on the mechanism of it should be made in the future.
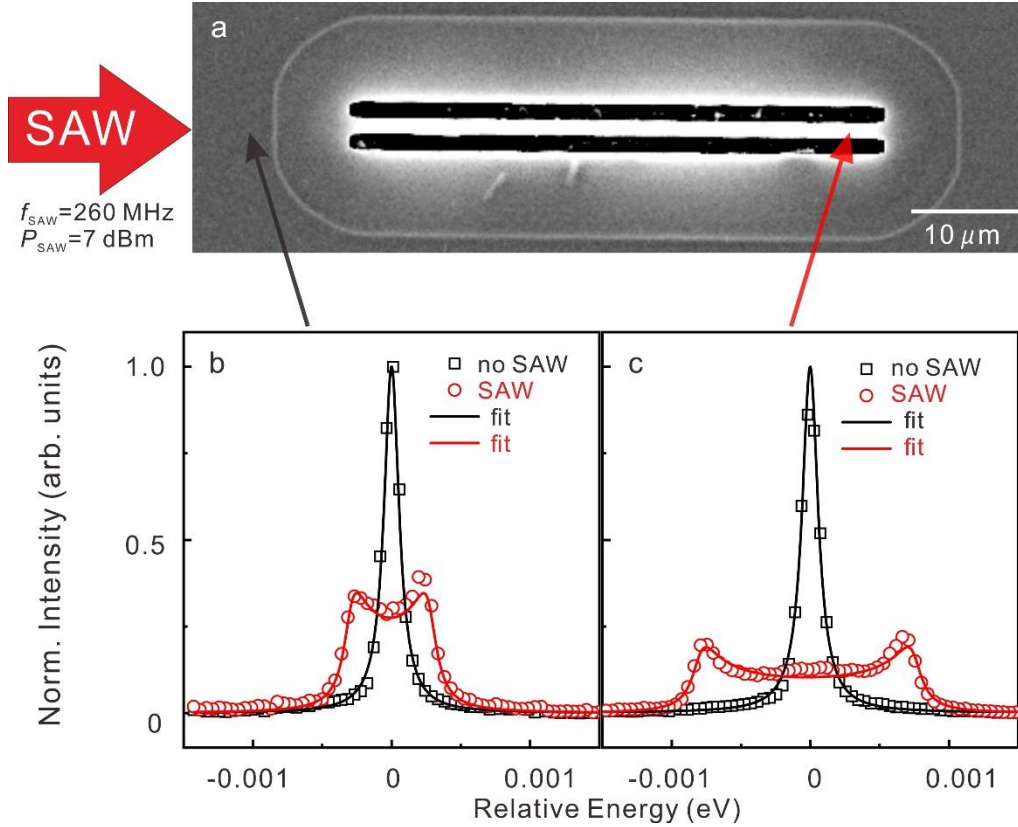
Fig. 6.8: Optomechanical coupling study of Rayleigh wave and Lamb wave. (a) SEM image of the device, in which different areas (bulk area and suspended area, as indicated by arrows) were chosen to make a comparison on the optomechanical coupling. Emissions of QDs (b) in bulk area and (c) in suspended beam without SAW applied (black squares) and modulated by a 260 MHz SAW (red circles). Solid lines are the fit results from equation (6.3). Data courtesy of Anja Vogele at University Augsburg[187].

The frequency dependent Lamb waves interaction with QDs in the suspended beam are characterized by measuring the PL spectra of QDs while sweeping the radio frequency f generated by the signal generator, as shown in Fig. 6.9 (a). From the color plot of the normalized PL spectra, spectral broadening could be clearly observed at the same frequencies as what we observed in the bulk area, as also illustrated in Fig. 6.9 (b), which is the extracted energy broadening ΔE as a function of frequencies f using the equation (6.3).
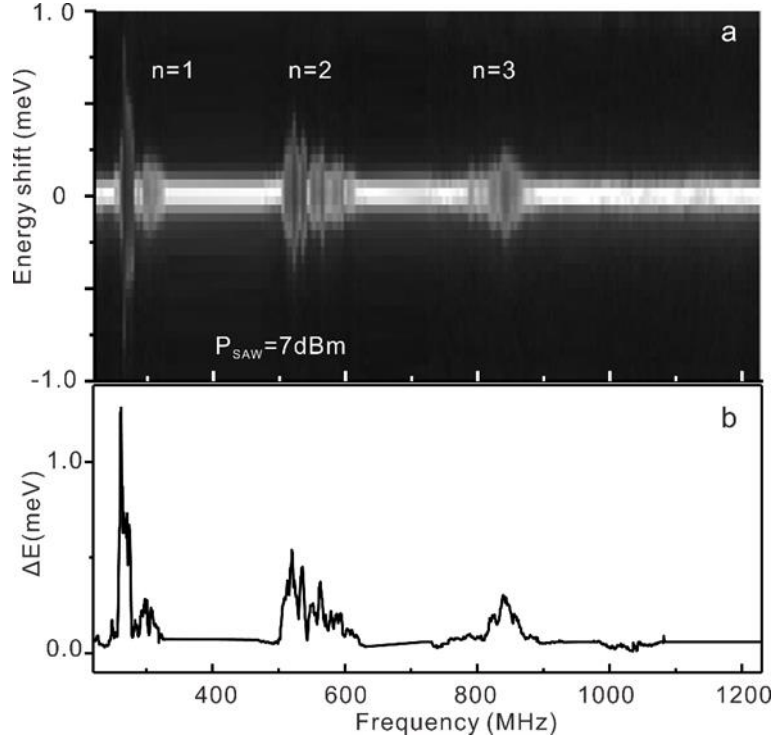
Fig. 6.9: (a) Color plot of the normalized emission of QDs located in a suspended beam as a function of frequency f and energy shift ΔE. The characteristic frequency bands for IDTs are marked. (b) The energy shift ΔE-frequency f relation derived from the data in the upper panel with equation (6.3).

Before further distinguishing the Rayleigh wave and Lamb waves, which propagate in our sample, let's first introduce a phase scan measurement via phase-locked setup. There are several methods to perform the time-resolved measurement of the QDs emission under periodical modulation. In the last chapter, we used an APD to make the time-resolved measurement. The biggest advantage of this method is the high time resolution in time scale. However, APD is a single channel detector and each time only one specific position (wavelength) can be chosen, this is a limitation and makes it difficult to compare the behavior of different QDs. A stroboscopic method is therefore adopted. The overview of the experimental setup of the phase-locking method is illustrated in Fig. 6.10 (a). In this setup, a delay generator is used for synchronization. Control pulse signals will be sent to both laser and function generator, and a short delay Δt is provided to the signal to the laser to compensate the velocity difference between light (laser) and sound (SAW). Laser and SAWs are only active with the "ON" stage of the control pulse signal, which is an effective way to avoid heating effects from the laser and SAWs. Different from previous experiments, here a frequency relation between SAWs and laser should be fulfilled to get the phase locking: $f_{SAW} = m \cdot f_{laser}$, m is an integer. As illustrated in Fig. 6.10 (b), then the laser will always hit the same phase of the signal of the SAW. Through changing the delay time Δt or phase difference $\Delta\varphi$ between the signal of SAW and laser, we can make a phase sweep measurement through the whole period.

a

b
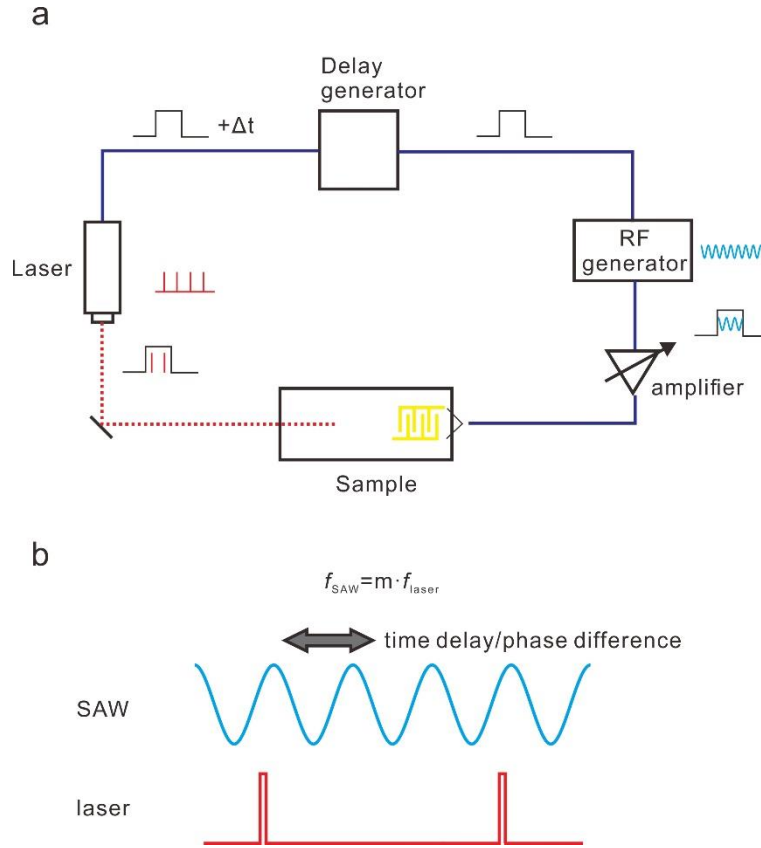
Fig.6.10: (a) Schematic picture of the experimental implementation of the phase scan. (b) Sketch of the electric signal of SAW and laser with phase-locked configuration. The frequency of SAW is integer multiples of the frequency of the laser.

Considering that the wavelength of antisymmetric Lamb waves (0.7 μm<λ_A<2.5 μm) is much shorter than the one of Rayleigh waves (5μm<$\lambda_{Rayleigh}$<15μm) in the working frequency (full data see Fig. 6.7 (b)), and the diameter of the excitation laser is roughly 1~1.5 μm, the QDs modulated by antisymmetric Lamb modes should exhibit quite an evident phase difference compared to the ones interfaced with Rayleigh waves. In aother words, we need to make a comparison of the phase sweep measurements of QDs in the bulk area and suspended beam under the modulation of SAWs. For this purpose we use the type I QDs because of their higher surface density. Fig. 6.11 (a) is the PL spectrum of QDs which are excited in the unsuspended, bulk area, where Rayleigh waves propagate. Several peaks appear in this spectrum, which we attribute to different QDs located in the laser spot area and are excited simultaneously. With these QDs, a phase sweep measurement was performed under the SAWs resonance. The right inset is the color plot of the PL emission of a QD (QD2) during the phase scan. The position of the peak is fitted with a Lorentz function, then the peak position-phase relations is fitted with sinusoid. Fig. 6.11 (b) summarizes the fitted data of all the seven QD lines labeled in Fig. 6.11 (a). These data are fitted with a general sinusoidal function $y = y_0 + A * \sin(\pi * (x - x_c)/\omega)$, x_c is the phase constant. The calculated phase constants for each QDs are shown below:

QD	0	1	2	3	4	5	6
x_c (°)	-40.67	-40.16	-27.53	-19.07	-28.82	-49.18	-20.73

The phase constants x_c for all QDs are quite close. The deviations could mainly come from the following aspects: the natural phase difference. Considering the diameter of the laser spot is 1μm and the wavelength of the Rayleigh wave is 11.5 μm, the maximum phase difference $\Delta x_c = \frac{1}{11.5} \times 360\,° \approx 31.3\,°$, and the phase variations are below this threshold.
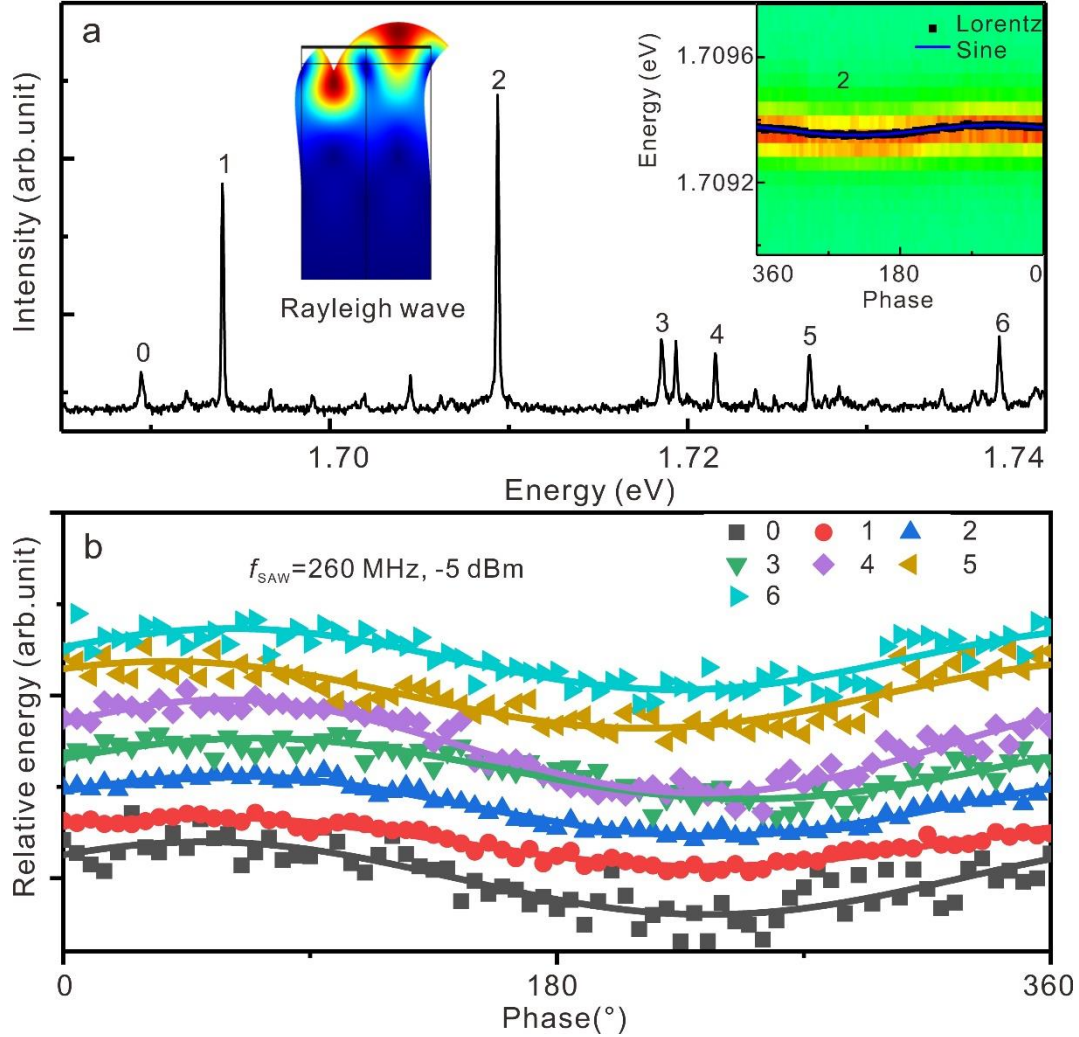
Fig. 6.11: (a) PL spectrum of QDs in the bulk area, which are excited with the same laser spot. The different peaks are attributed to the emission of different QDs and are marked with numbers. The left inset shows schematically the mode deformation of a unit cell of sample AS275 due to the interaction to Rayleigh wave. The right inset is the color plot of phase-resolved PL spectra of QD2 with a sinusoidal fit. (b) Summary of all the QDs energy shift as a function of phase. The data (symbols) are fit with sinusoidal functions (solid lines). Data courtesy of Anja Vogele at University Augsburg[187].

Then we perform the same phase sweep measurements on the suspended beam, the PL spectrum is shown in Fig. 6.12 (a). Following the same procedure as above, we obtain the data shown in Fig. 6.11 (b). The phases x_c for each QD are shown in the table.

Here it is evident to see the QDs experience a periodical oscillation with substantially different phases, which can be explained by the shorter wavelength of the fundamental antisymmetric Lamb wave (λ_A=2.38 μm for f=260 MHz). In summary, through the phase sweep measurement on QDs located in bulk area and suspended beam, we manage to obtain an indirect proof of the propagation of the antisymmetric Lamb wave in the suspended beam.

QD	0	1	2	3	4	5
x_c (°)	-70.56	253.79	236.79	-76.32	275.34	-60.55
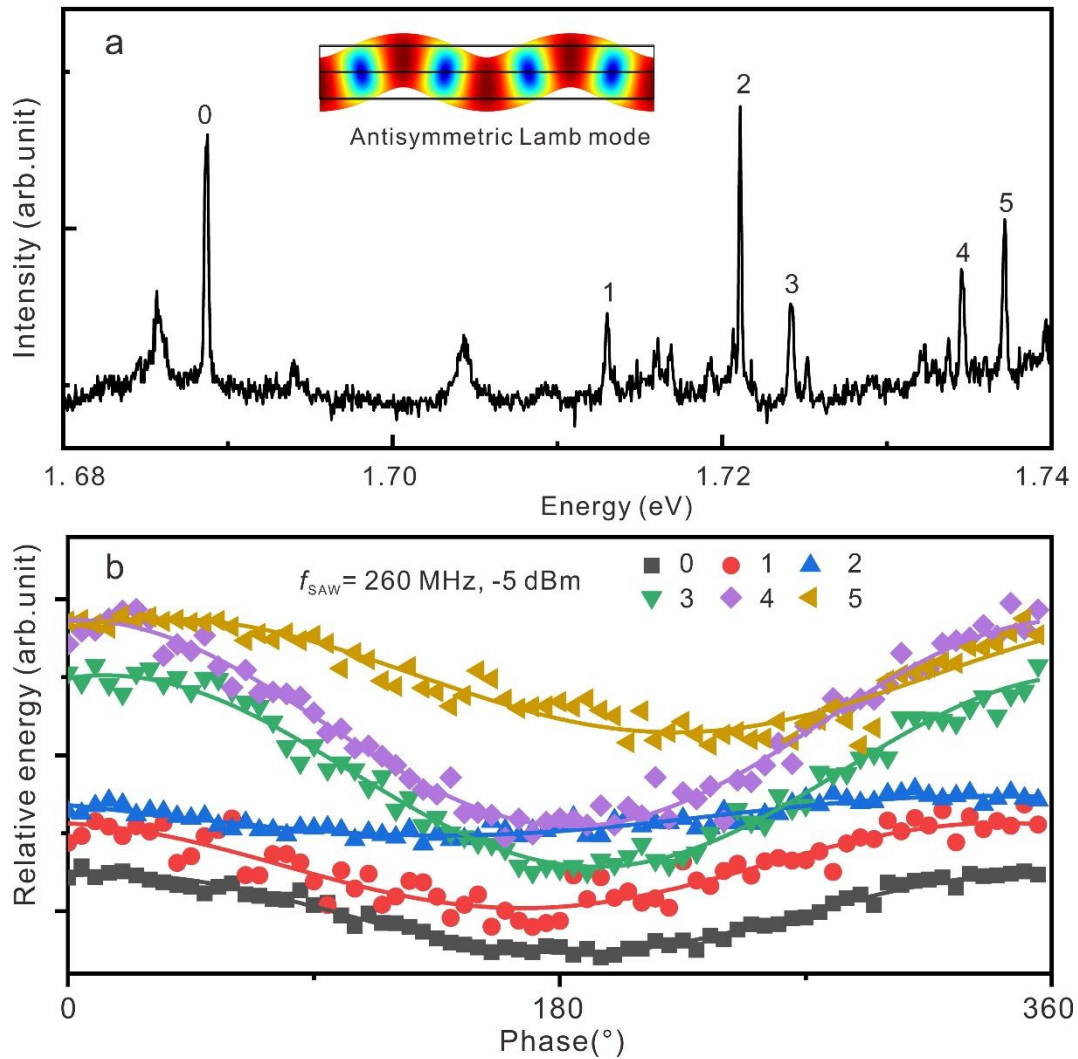
Fig. 6.12: (a) The PL spectrum of QDs in the suspended beam, which is excited with the same laser spot. The inset shows the mode deformation of the suspended beam with the propagation of an antisymmetric Lamb mode. (b) Relative energy shift of all the QDs in the suspended beam as a function of the phase (symbols are the experimental data, solid lines are sinusoidal fit to the data).

Another important issue which is important in this study is the attenuation of the propagating Lamb waves in the suspended beam. Thus, we studied three suspended beams (50×1.5 μm^2) and measured modulated PL spectra of the QDs for different Lamb

wave frequencies. The QDs are located at different positions along the propagation direction to obtain information on the attenuation. . A schematic of this experiment is shown in Fig. 6.13 (a). Fig 6.13 (b) shows as an example the positions of five QD we chose in one particular beam.
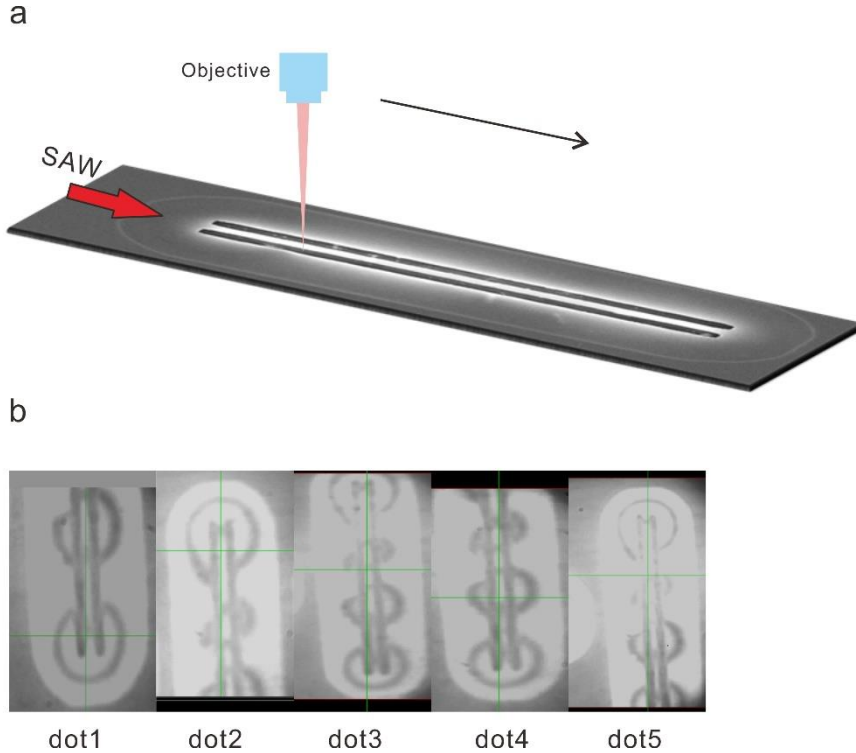
Fig. 6.13: (a) Schematic picture of the measurement on QDs located at different positions along the sound wave propagation direction. (b) Microscope pictures of the typical 5 dots we chose for the measurement, the green crosses indicate the position of QDs. The sound waves propagate from top to bottom.

The spectral broadening ΔE is again obtained by fitting the time-averaged spectra using equation (6.3), and the obtained data are shown in Fig. 6.14. To further analyze the possible attenuation properties, an exponential attenuation function is assumed:

$$y(x) = y_0 10^{\delta \cdot x} \tag{6.4}$$

y_0 is the amplitude at x=0 and δ is the attenuation coefficient. Then we take the log of

the equation: $\log y(x) = \log y_0 + \log\left(10^{\delta \cdot x}\right) = A + \delta \cdot x$, A is a constant. Therefore,

the spectral broadenings ΔE induced from the Lamb wave are shown in log scale. Then we perform a linear fit of the spectra broadening ΔE-position x relations for different frequencies, the slopes of the linear fits (δ) for different frequencies are listed in Table 6.1. From Figure 6.14 and the slopes of the linear fits in Table 6.1, it is obvious that no clear trend can be extracted. Most importantly however, no pronounced attenuation is observed in all data. This finding indicated that on these length scale the elastic wave is hardly damped at all. Moreover, we assume that extrinsic effects (such as local imperfections of the beams or different distance between a QD and one edge of the beam) are responsible for the scatter of the data points, preventing us a reliable estimate of the small attenuation coefficient.
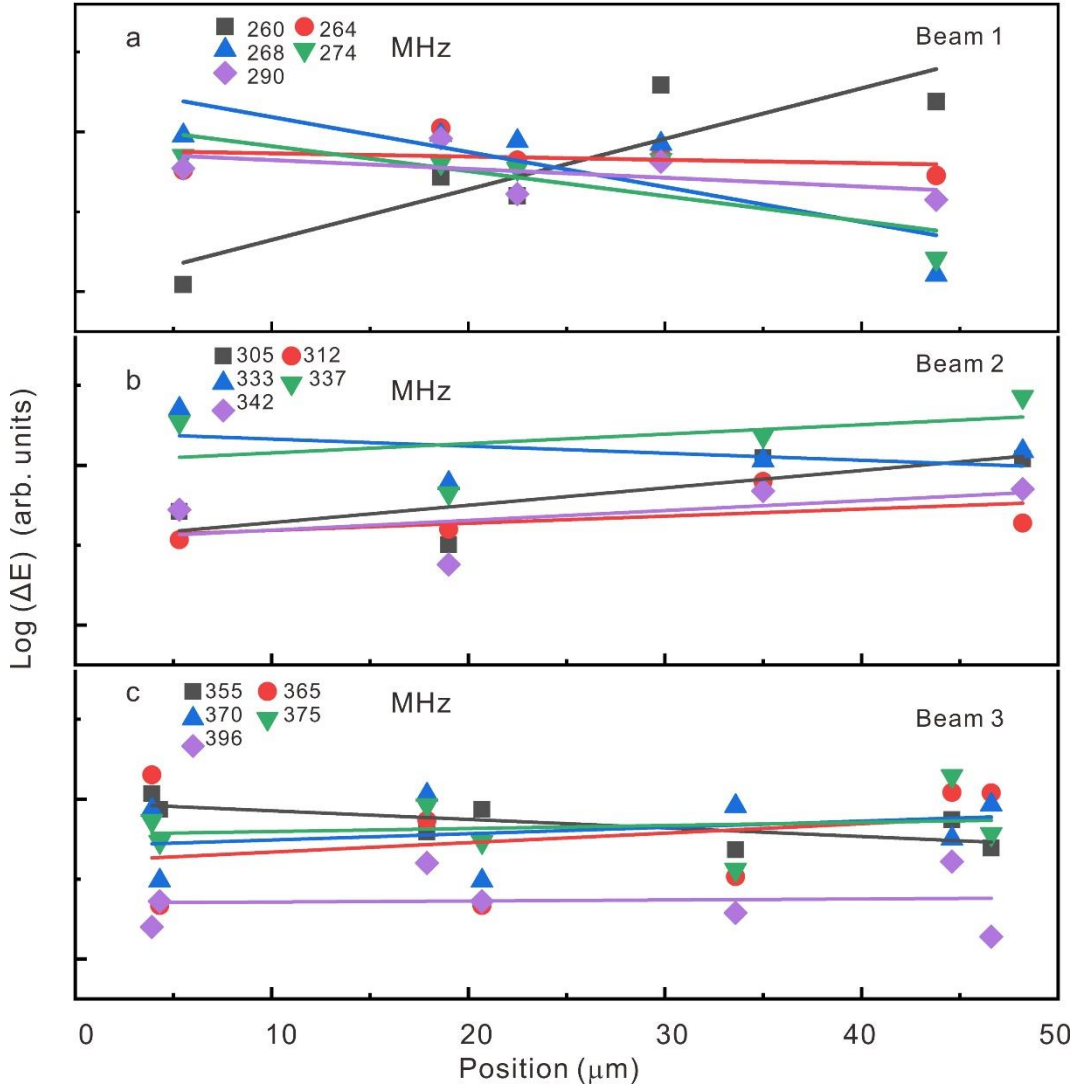
Fig. 6.14: Log scale plot of the spectral broadening ΔE induced by Lamb waves of different QDs located at different positions along the propagation direction. (a), (b) and (c) are data from three different suspended beams of identical size (50×1.5 μm^2, referred to as Beam 1, 2 and 3, respectively). Data courtesy of Anja Vogele, University Augsburg[187].

Beam 1	Frequency (MHz)	260	264	268	274	290
	Slope δ (0.1·dB/μm)	0.03164 ± 0.00928	-0.00204 ± 0.00456	-0.02189 ± 0.00909	-0.01562 ± 0.00653	-0.0053 ± 0.00556
Beam 2	Frequency (MHz)	305	312	333	337	342
	Slope δ (0.1· dB/μm)	0.01087 ± 0.00650	0.00444 ± 0.00515	-0.00442 ± 0.00665	0.00588 ± 0.00873	0.00612 ± 0.00712
Beam 3	Frequency (MHz)	355	365	370	375	396
	Slope δ (0.1·dB/μm)	-0.00536 ± 0.00232	0.00592 ± 0.00853	0.00395 ± 0.00554	0.00191 ± 0.0047	0.00064 ± 0.00462

Table 6.1: Extracted attenuation coefficient δ (the slopes of linear fit) at different frequencies. Data

courtesy of Anja Vogele at University Augsburg[187].

6.5 Conclusion and outlook

In summary, a sample with suspended beams containing QDs was fabricated. Firstly, employing wide passband IDTs, we are able to study and make a comparison of the acoustic wave propagation properties in bulk and suspended beams over a wide range of frequencies. Secondly, with a stroboscopic, phase-locked spectropscopy, we verify the propagation of predominantly the antisymmetric, flexural Lamb wave in the suspended beam, consistent with the simulation. Last but not least, using QDs as vibration sensors, the propagation attenuation properties of the antisymmetric Lamb waves is studied and no evident sign of attenuation is observed along the propagation direction.

Based on the work we have presented in this chapter, next steps can be envisioned:

1. Although no clear indication of pronounced attenuation of Lamb waves was observed in the suspended beams, some more detailed and convincing experiments need to be performed in particular using waveguides of different geometries.

2. In chip hybrid devices which sound-light-matter interaction can be fully integrated between the phononic/photonic resonators and QDs, and we believe this will make a great advancement of state-of-the-art quantum cavity electrodynamic, nano-photonic and optomechanical systems[188,189].

3. Since SAWs is a very powerful method to manipulate the QDs, more work may be done on the optomechanical systems (as proposed in Chapter 5), resolve the acoustic sidebands of QDs[116], especially based on the novel droplet etched GaAs QDs.

7. Conclusion and outlook

7.1 Conclusion

In this thesis, we focused on the tuning of the properties of QDs with strain fields and the following contributions to the field have been made:

1. A novel micro-machined PMN-PT actuator, which combines the advantage of strain amplifying suspension platform and continuously variable stress, is designed and implemented. With this PMN-PT actuator, a highly variable uniaxial stress up to 1.5 GPa was applied to strain-free GaAs QDs. Through a wedged geometry of the suspended membranes, we were able to follow the evolution of the excitonic emission as a function of applied stress. Together with theoretical calculations, our findings prove that the natural quantization axis of GaAs QDs can be flipped into the growth plane, which paves a new door for the use of QDs as light emitters in integrated quantum photonic systems.

2. A QD-based mechanical resonator is proposed and realized. Here a PMN-PT piezoelectric actuator is employed for the mechanical excitation. With the use of a bias tee, AC and DC signals can be applied to the PMN-PT actuator simultaneously to achieve the reversible tuning of the resonant frequency. Besides that, we show that the actuator can sustain oscillations of at least up to 61.5 MHz, according to time-resolved measurement. The hybrid quantum device, once optimized and miniaturized, may be appealing for applications in which tuning of the resonant frequency is important.

3. A GaAs QD sample with suspended beams (phononic waveguide) is fabricated. With the assistance of wide bandpass IDTs, we are able to observe the acousto-optic spectroscopy of the QDs located both in the bulk and suspended beam over wideband frequencies. Through the stroboscopic spectroscopy of QDs based on phase-locked scheme, the propagation of antisymmetric Lamb waves in the suspended beam is proved. Lastly, the propagation attenuation properties of the sound waves in suspended beam is studied.

7.2 Outlook

In this thesis, substantial progress has been made on the strain tuning of the optical and electronic properties of QDs. To make QDs the suitable quantum source for the future large-scale quantum system the following requirements have to be met:

1. According to the theoretical calculation on the transition strength of the QD dipoles under uniaxial stress (Fig. 4.19) in Chapter 4, it would be very interesting to go to the compression regime, in which in-plane light hole exciton LH_x can be obtained. The lifetime of one component will prominently drop under the compressive stress, which we expect to lead to an improvement of the indistinguishability due to the

effective suppression of spectral jitter. To achieve this, several obstacles need to be overcome. First, the PMN-PT actuator we used now is not suitable for compressive stress, some other methods need to be used, such as the employment of materials with different thermal expansion coefficient[94]. Second, a proper excitation method is required to obtain the real lifetime. Due to the existence of long relaxation time in GaAs QDs, resonant excitation or specific quasi-resonant excitation methods should be. A scheme in which the QDs is excited quasi-resonantly one LO-phonon above the exciton energy[190] level could be a suitable method for that.

2. In Chapter 5 a hybrid system with QDs (two-level system) coupled to the mechanic resonator is demonstrated to mechanical eigenfrequencies up to 61.5 MHz . However, one of the most appealing features of the hybrid optomechanical system is the QND readout, which require a comparable mechanical period to the lifetime of QDs (InAs QDs: 1 ns, GaAs QDs: 250 ps), which may be hard to achieve. Furthermore, instead of using electric field to manipulate the g tensor[163], strain field provided by the device we presented in this thesis would be a better choice because of the exclusion of charge noise. However, to effectively manipulate electron spin (relatively short decoherence time in QDs: 0.1-1 ns)[191], high frequency resonance is desirable and an optimized hybrid system with excellent high-frequency behavior is needed for the future work. For long-lived quantum systems such as spins, mechanical modulation may be instead feasible. Here systematic studies of the effect of strain on the g-tensor will be required first.

3. In Chapter 6, we present a first study of the propagation properties of the sound waves in suspended beams. In the future, it would be desirable to continue on the phononic/photonic circuits on chip, which can interact with the QDs[188]. Besides, considering the lateral electric field generated by the Lamb wave, the Lamb wave could act as a "clean" method to study the effect of lateral electric field modulation to the properties of the QDs.

Appendix

A.1 Piezoelectric parameters of PMN-PT (RT)

The PMN-PT piezoelectric actuators used in this work are purchased from TRS Technologies, and we get the piezoelectric parameters (RT) from the company, we employ these parameters in the stress/strain simulations by COMSOL Multiphysics. The piezoelectric parameters are listed as below:

Compliance matrix

$$s_E =$$

$$
\begin{bmatrix}
52.1 \times 10^{-12} & -24.6 \times 10^{-12} & -26.4 \times 10^{-12} & & & \\
-24.6 \times 10^{-12} & 52.1 \times 10^{-12} & -26.4 \times 10^{-12} & & & \\
-26.4 \times 10^{-12} & -26.4 \times 10^{-12} & 59.9 \times 10^{-12} & & & \\
0 \quad 0 \quad 0 & & & 16.0 \times 10^{-12} & 0 & 0 \\
0 \quad 0 \quad 0 & & & 0 & 16.0 \times 10^{-12} & 0 \\
0 \quad 0 \quad 0 & & & 0 & 0 & 28.3 \times 10^{-12}
\end{bmatrix}
$$

1/Pa.

Piezoelectric coupling matrix

$$d =$$

$$
\begin{bmatrix}
0 & 0 & 0 & 0 & 164 \times 10^{-12} & 0 \\
0 & 0 & 0 & 164 \times 10^{-12} & 0 & 0 \\
-699 \times 10^{-12} & -699 \times 10^{-12} & 1540 \times 10^{-12} & 0 & 0 & 0
\end{bmatrix}
$$

C/N

Relative permittivity

$$
\epsilon_{rT} =
\begin{bmatrix}
1560 & 0 & 0 \\
0 & 1560 & 0 \\
0 & 0 & 5400
\end{bmatrix}
$$

And density $\rho = 8093 \text{ kg/m}^3$.

A.2 Additional PL data on macroscopic and narrow stripe membranes

To confirm the reliability and reproducibility of the results shown in Chapter 4, measurements on another device with a macroscopic membrane were performed. The data collected on a randomly chosen QD located in the area of the membrane suspended above the actuator gap are shown in Fig. A.1. Fig. A.1 (a) shows the color-coded PL

spectra of the selected QD as a function of linear-polarization direction with no applied voltage to the actuator ($F_p = 0$ kV/cm). In spite of the fact that no stress is intentionally applied to the membrane, we see slightly polarized emission from the neutral exciton (X) and multiexcitonic lines (MX) and a substantially larger X fine-structure-splitting (FSS) compared to the values obtained on as-grown samples. We attribute these two observations to residual (anisotropic, see below) stress arising from the device processing and from the different thermal expansion coefficients of the materials present in the device (PMN-PT, semiconductor, SU8 etc.). Under strong tension, see Fig. A.1 (b), all lines are nearly 100% polarized, similar to the results shown in Fig. 4.10 (c). In Fig. A.1 (c), we plot the degree of linear polarization P of X and MX as a function of F_p (tensile stress). For the MX lines we integrated the intensity of all lines. It is obvious that P increases with the increasing tensile stress, which is consistent with the experimental and theoretical analysis in the main text.

The presence anisotropic prestress combined with random fluctuations in the confinement potential defined by the QD lead to emission which is partially linearly polarized along a random direction. In Fig. A.1 (d) we plot the polarization direction φ^* along which the emission intensity is maximal as a function of the electric field across the actuator fingers (which we expect to be approximately proportional to the applied uniaxial stress). Although the QD was initially pre-stressed, the emission lines (X and MX) become fully polarized perpendicular to the pulling direction at large uniaxial stress, which is consistent with the theoretical prediction.
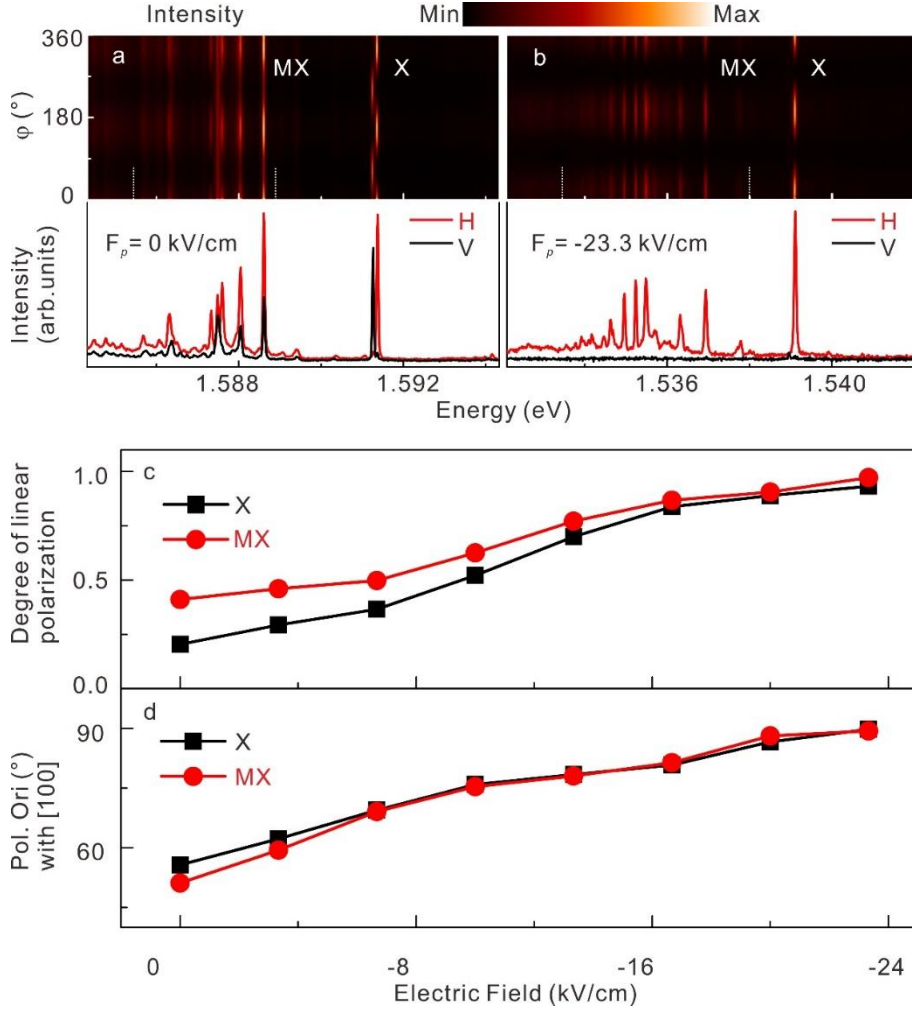
Fig. A.1: Color coded linear-polarization-resolved PL spectra of a GaAs QD in macroscopic membrane at (a) 0 applied field across the actuator and under (b) high tensile stress. X and MX stand for neutral exciton and multiexcitonic lines. The slight polarization anisotropy observed in (a) is attributed to process- and cooling- induced stress. (c) Evolution of polarization degree with increasing tensile stress (magnitude of electric field F_p). (d) Evolution of the polarization orientation of X and MX for increasing $|F_p|$. While the initial polarization is randomly oriented, light becomes fully polarized parallel to the y direction (perpendicularly to the pulling direction) at large stress.

Figure A.2 shows a set of polarization-resolved PL spectra of a neutral exciton X confined in a GaAs QD (QD1) under different tensile stresses [the same dot shown in Fig. 4.7]. These spectra provide a clear picture of the evolution of the X fine structure during the transition from a HH_z to a HH_x hole ground state (HGS). With increasing uniaxial stress, the initially dark exciton D_z becomes bright and gradually moves from the low energy side of the bright exciton B_y to its high energy side, and finally becomes a bright exciton B_z. The z-polarized component (D_z or B_z) is reflected by the sidewalls of stripe membrane and appears to have polarization approximately parallel to the y direction, as expected. The initially bright exciton B_x moves to the low side energy side of B_y with increasing stress. Moreover, the intensity of B_x drops monotonically with increasing stress (for this reason we refer to it as D_x for large tensile stress). Data shown

in Fig. 4.15 and additionally collected for different values of the field F_p applied to the actuators were averaged to obtain a single spectrum for each value of F_p. To highlight the evolution of the fine structure, such spectra were shifted along the energy axis using the B_y as a reference. The result is shown in Fig. A.2 (a,b). The same procedure was used for another QD (QD2) [Fig. 4.15], which shows fully consistent behavior. Similar data for still another QD (QD3) are shown in Fig. A.2 (c,d).
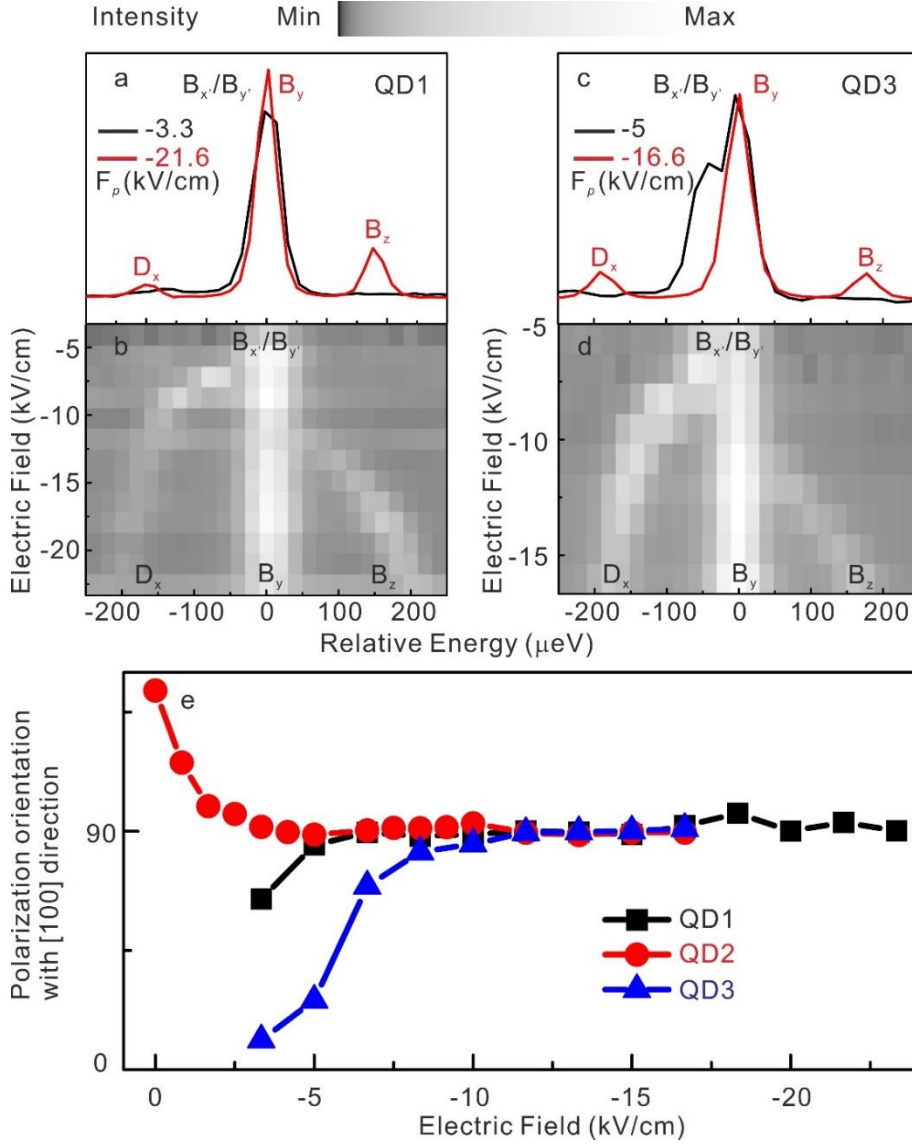
Fig. A.2: Evolution of fine structure of the neutral exciton confined in different QDs in narrow stripe membrane for increasing magnitude of electric field applied (uniaxial stress). (a), (b) for QD1, (c), (d) for QD3. Similar plots for QD2 are shown in Fig. 4.16 of Chapter 4. (e) Evolution of the neutral exciton polarization orientation for different QDs for varying magnitude of electric field applied to the actuator (uniaxial stress).

Overall, we see very similar behavior for all QDs. In addition, the high energy component B_z is consistently observed only in QDs contained in narrow stripes and not in large membranes. It should be noted that - especially for QD3 - a "full darkening" of

the D_x line is not achieved within the applied range of F_p values. We qualitatively attribute this observation to the presence of prestress with main axes away from the [100] and [010] directions, consistent with the large FSS observed at low F_p.

Lastly, the polarization orientation of the neutral exciton in QDs embedded in stripe membranes with increasing magnitude of the electric field (uniaxial stress) is plotted in Fig. A.2 (e). Consistent results are obtained with QDs embedded in macroscopic membranes: the polarization orientations show initially (no intentional uniaxial stress applied) quite a random direction, and become perpendicular to the pulling direction ([100] direction) with increasing uniaxial stress. All these results provide compelling evidence that uniaxial stress can be used to deterministically set the orientation of the transition dipoles in a QD, consistent with the theory.

A.3 Energy shift of other excitonic species under uniaxial stress along the [100] direction

In Chapter 4 and in the previous appendix, we have mostly focused on the behavior of neutral excitons under uniaxial stress. The main reason is that the origin of the other lines was not well established at the time of writing this thesis and attempts to reproduce the behavior of charged excitons via theoretical calculations were not conclusive. Fig. A.3 shows the relative shift of the excitonic spectra for two QDs obtained by using one of the bright states of the neutral excitons as references. We clearly note that different lines react differently to the applied stress. In particular, a bright line on the low energy of the X (most probably related to the positive trion, consisting of an electron and two holes[192]) shows a non-monotonic shift relative to the neutral exciton.

These data, combined with other experiments, may be helpful to obtain a complete picture of the excitonic structure of GaAs QDs used here and in other recent works of our group and other groups[69,70,193].
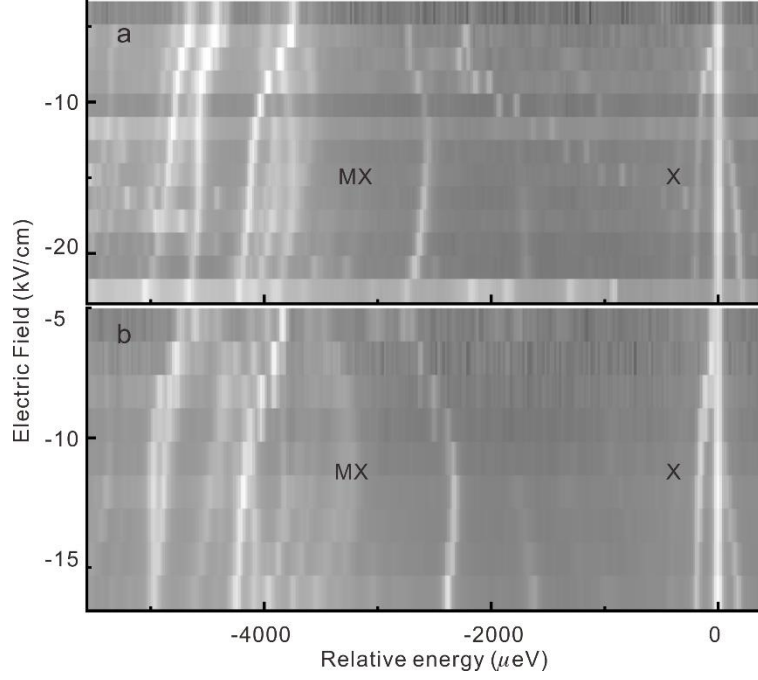
A.3: Representative evolution of the emission of different GaAs QDs ((a) and (b)) as a function of electric fields (F_p) applied to the PMN-PT actuator (uniaxial stress). Here the same bight states ($B_{y'}$ or B_y, as illustrated in Fig. 4.15 and Fig. 4.16) are used as reference to shift the spectra horizontally. X indicates the neutral exciton and MX means the multiexciton.

A.4 Uniaxial stress tuning along piezoelectric directions

Since [110] direction is another a vital uniaxial stress direction to effectively tune the excitonic properties of QDs[44,45], it would be desirable to see what we can get if we apply the uniaxial stress along [110] direction.

Before go to the experimental results, stress configurations were analyzed. Here using the same coordinate system as in Chapter 4, the uniaxial stress along [110] direction can be decomposed into uniaxial stresses along [100] σ_{xx}, [010] σ_{yy} directions and shear stress σ_{xy}, with the same amplitude. The Hooke's law for cubic semiconductor reads

$$\begin{pmatrix} \sigma_{xx} \\ \sigma_{yy} \\ \sigma_{zz} \\ \sigma_{yz} \\ \sigma_{xz} \\ \sigma_{xy} \end{pmatrix} = \begin{pmatrix} C_{11} & C_{12} & C_{12} & 0 & 0 & 0 \\ C_{12} & C_{11} & C_{12} & 0 & 0 & 0 \\ C_{12} & C_{12} & C_{11} & 0 & 0 & 0 \\ 0 & 0 & 0 & C_{44} & 0 & 0 \\ 0 & 0 & 0 & 0 & C_{44} & 0 \\ 0 & 0 & 0 & 0 & 0 & C_{44} \end{pmatrix} \begin{pmatrix} \varepsilon_{xx} \\ \varepsilon_{yy} \\ \varepsilon_{zz} \\ 2\varepsilon_{yz} \\ 2\varepsilon_{xz} \\ 2\varepsilon_{xy} \end{pmatrix}$$

With $\sigma_{xx} = \sigma_{yy} = \sigma_{xy} = \sigma_{yx}, \sigma_{zz} = \sigma_{yz} = \sigma_{xz} = 0$.

then we can get $\varepsilon_{xx} = \varepsilon_{yy}, \varepsilon_{zz} = -\dfrac{2C_{12}}{C_{11}}\varepsilon_{xx}, \varepsilon_{xy} = \dfrac{C_{44}\cdot\sigma_{xy}}{2}, \varepsilon_{yz} = \varepsilon_{xz} = 0,$

Besides, a electric field inside GaAs crystal appears under the shear stress or strain, the piezoelectric field under [110] stress or strain reads[194]

$$E_{[001]} = -\frac{d_{14}\sigma_{xy}}{2\varepsilon_0(1+\chi)} = -\frac{e_{14}\varepsilon_{xy}}{\varepsilon_0(1+\chi)}$$

Where d_{14} and e_{14} are the piezoelectric tensor coefficients, ε_0 is the permittivity of free space and $(1+\chi)$ is low frequency dielectric constant. So in the case of uniaxial stress along [110] direction, an additional vertical electrical field need to be taken into account. There are two effects could be induced by the vertical electric field: (i) valence and conduction bands become tiled, which causes a relevant energetic difference between electrons and holes, which is called Stark effect[195]. (ii) Carrier capture from the AlGaAs layer is sensitive to the electric field, When the tunneling rate arrives at a comparable level of the radiative recombination rate, the emission peaks get broaden and even quenched[196–198]. Nevertheless, we performed the experiments which pulled the GaAs QDs both along [110] and [1$\bar{1}$0] directions, the results are shown in Fig. A.3 (a)-(b), (c)-(d), respectively. The spectra evolution under [110] direction uniaxial tensile stress is consistent with what we analyzed. However, sudden annihinations of the PL spectra was observed during the pulling along [1$\bar{1}$0] directions (as shown in Fig. A.3(c)), currently this is still a puzzling issue to us and more time need to be spent to explore the physics behind it.

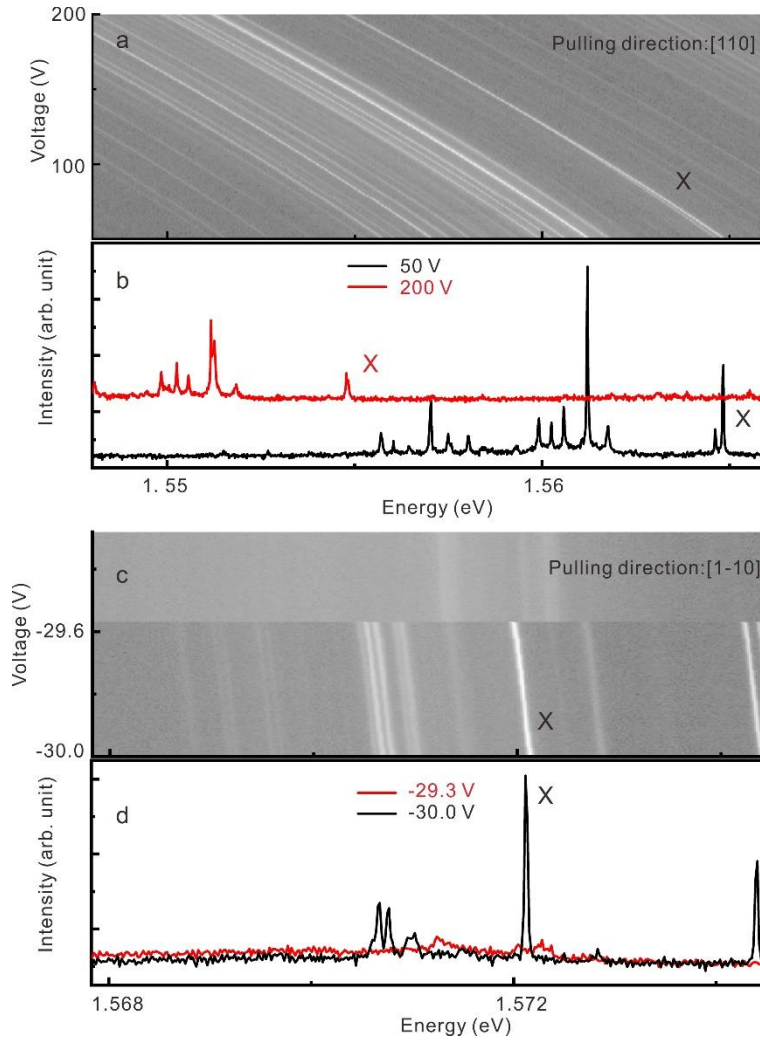**Fig. A.4**: (a) Color coded PL spectra of GaAs QDs emission as the function of the voltage applied to the PMN-PT actuator, the pulling direction is along [110] direction. (b) Two typical PL spectra of GaAs QDs under different tensile stresses (voltages) along [110] direction. (c), (d) are similar data to (a), (b), respectively, but with a different pulling direction along [1$\bar{1}$0]. The neutral excitons are marked as X.

Bibliography

1.   Gisin, N. & Thew, R. Quantum communication. *Nat. Photonics* **1,** 165–171 (2007).

2.   Dowling, J. P. & Milburn, G. J. Quantum technology: the second quantum revolution. *Philos. Trans. R. Soc. A Math. Phys. Eng. Sci.* **361,** 1655–1674 (2003).

3.   Senellart, P., Solomon, G. & White, A. High-performance semiconductor quantum-dot single-photon sources. *Nat. Nanotechnol.* **12,** 1026–1039 (2017).

4.   Lounis, B. & Orrit, M. Single-photon sources. *Reports Prog. Phys.* **68,** 1129–1179 (2005).

5.   Muller, A. *et al.* 'Plug and play' systems for quantum cryptography. *Appl. Phys. Lett.* **70,** 793–795 (1997).

6.   Kuhn, A., Hennrich, M. & Rempe, G. Deterministic single-photon source for distributed quantum networking. *Phys. Rev. Lett.* **89,** 067901 (2002).

7.   Lounis, B. & Moerner, W. E. Single photons on demand from a single molecule at room temperature. *Nature* **407,** 491–493 (2000).

8.   Kurtsiefer, C., Mayer, S., Zarda, P. & Weinfurter, H. Stable solid-state source of single photons. *Phys. Rev. Lett.* **85,** 290–293 (2000).

9.   Gérard, J. M. & Gayral, B. InAs quantum dots: Artificial atoms for solid-state cavity-quantum electrodynamics. *Phys. E Low-Dimensional Syst. Nanostructures* **9,** 131–139 (2001).

10. Badolato, A. *et al.* Deterministic coupling of single quantum dots to single nanocavity modes. *Science.* **308,** 1158–1161 (2005).

11. He, Y. M. *et al.* On-demand semiconductor single-photon source with near-unity indistinguishability. *Nat. Nanotechnol.* **8,** 213–217 (2013).

12. Ding, X. *et al.* On-Demand Single Photons with High Extraction Efficiency and Near-Unity Indistinguishability from a Resonantly Driven Quantum Dot in a Micropillar. *Phys. Rev. Lett.* **116,** 020401 (2016).

13. Huber, D. *et al.* Strain-Tunable GaAs Quantum Dot: A Nearly Dephasing-Free Source of Entangled Photon Pairs on Demand. *Phys. Rev. Lett.* **121,** 033902 (2018).

14. Michler, P. *et al.* A quantum dot single-photon turnstile device. *Science.* **290,** 2282–5 (2000).

15. Hong, C. K., Ou, Z. Y. & Mandel, L. Measurement of subpicosecond time intervals between two photons by interference. *Phys. Rev. Lett.* **59,** 2044 (1987).

16. Fearn, H. & Loudon, R. Theory of two-photon interference. *J. Opt. Soc. Am. B* **6,** 917–927 (1989).

17. Beugnon, J. *et al.* Quantum interference between two single photons emitted by independently trapped atoms. *Nature* **440,** 779–782 (2006).

18. Maunz, P. *et al.* Quantum interference of photon pairs from two remote trapped atomic ions. *Nat. Phys.* **3,** 538–541 (2007).

19. Kiraz, A. *et al.* Indistinguishable photons from a single molecule. *Phys. Rev. Lett.* **94,** 223602 (2005).

20. Patel, R. B. *et al.* Two-photon interference of the emission from electrically tunable remote quantum dots. *Nat. Photonics* **4,** 632–635 (2010).

21. Flagg, E. B. *et al.* Interference of single photons from two separate semiconductor quantum

dots. *Phys. Rev. Lett.* **104,** 147301 (2010).

22. Reindl, M. *et al.* Phonon-Assisted Two-Photon Interference from Remote Quantum Emitters. *Nano Lett.* **17,** 4090–4095 (2017).

23. Benson, O., Santori, C., Pelton, M. & Yamamoto, Y. Regulated and Entangled Photons from a Single Quantum Dot. *Phys. Rev. Lett.* **84,** 2513–2516 (2000).

24. Akopian, N. *et al.* Entangled photon pairs from semiconductor quantum dots. *Phys. Rev. Lett.* **96,** 130501 (2006).

25. Stevenson, R. M. *et al.* A semiconductor source of triggered entangled photon pairs. *Nature* **439,** 179–182 (2006).

26. Hudson, A. J. *et al.* Coherence of an entangled exciton-photon state. *Phys. Rev. Lett.* **99,** 266802 (2007).

27. Singh, R. & Bester, G. Nanowire quantum dots as an ideal source of entangled photon pairs. *Phys. Rev. Lett.* **103,** 063601 (2009).

28. Schliwa, A., Winkelnkemper, M., Lochmann, A., Stock, E. & Bimberg, D. In(Ga)As/GaAs quantum dots grown on a (111) surface as ideal sources of entangled photon pairs. *Phys. Rev. B - Condens. Matter Mater. Phys.* **80,** 161306(R) (2009).

29. Huo, Y. H., Rastelli, A. & Schmidt, O. G. Ultra-small excitonic fine structure splitting in highly symmetric quantum dots on GaAs (001) substrate. *Appl. Phys. Lett.* **102,** 152105 (2013).

30. Gong, M. *et al.* Statistical properties of exciton fine structure splitting and polarization angles in quantum dot ensembles. *Phys. Rev. B - Condens. Matter Mater. Phys.* **89,** 205312 (2014).

31. Pan, J. W., Bouwmeester, D., Weinfurter, H. & Zeilinger, A. Experimental entanglement swapping: Entangling photons that never interacted. *Phys. Rev. Lett.* **80,** 3891 (1998).

32. Langbein, W. *et al.* Control of fine-structure splitting and biexciton binding in InxGa1-xAs quantum dots by annealing. *Phys. Rev. B - Condens. Matter Mater. Phys.* **69,** 161301(R) (2004).

33. Tartakovskii, A. I. *et al.* Effect of thermal annealing and strain engineering on the fine structure of quantum dot excitons. *Phys. Rev. B - Condens. Matter Mater. Phys.* **70,** 193303 (2004).

34. Ellis, D. J. P. *et al.* Control of fine-structure splitting of individual InAs quantum dots by rapid thermal annealing. *Appl. Phys. Lett.* **90,** 011907 (2007).

35. Mrowiński, P. *et al.* Magnetic field control of the neutral and charged exciton fine structure in single quantum dashes emitting at 1.55 μ m. *Appl. Phys. Lett.* **106,** 053114 (2015).

36. Gerardot, B. D. *et al.* Manipulating exciton fine structure in quantum dots with a lateral electric field. *Appl. Phys. Lett.* **90,** 041101 (2007).

37. Vogel, M. M. *et al.* Influence of lateral electric fields on multiexcitonic transitions and fine structure of single quantum dots. *Appl. Phys. Lett.* **91,** 2005–2008 (2007).

38. Bennett, A. J. *et al.* Electric-field-induced coherent coupling of the exciton states in a single quantum dot. *Nat. Phys.* **6,** 947–950 (2010).

39. Ghali, M., Ohtani, K., Ohno, Y. & Ohno, H. Generation and control of polarization-entangled photons from GaAs island quantum dots by an electric field. *Nat. Commun.* **3,** 661 (2012).

40. Mar, J. D., Baumberg, J. J., Xu, X. L., Irvine, A. C. & Williams, D. A. Electrical control of quantum-dot fine-structure splitting for high-fidelity hole spin initialization. *Phys. Rev. B - Condens. Matter Mater. Phys.* **93,** 045316 (2016).

41. Ding, F. *et al.* Tuning the Exciton Binding Energies in Single Self-Assembled InGaAs /GaAs Quantum Dots by Piezoelectric-Induced Biaxial Stress. *Phys. Rev. Lett.* **104,** 067405 (2010).

42.   Seidl, S. *et al.* Effect of uniaxial stress on excitons in a self-assembled quantum dot. *Appl. Phys. Lett.* **88,** 203113 (2006).

43.   Zander, T. *et al.* Epitaxial quantum dots in stretchable optical microcavities. *Opt. Express* **17,** 22452–22461 (2009).

44.   Gong, M., Zhang, W., Guo, G. C. & He, L. Exciton polarization, Fine-structure splitting, and the asymmetry of quantum dots under uniaxial stress. *Phys. Rev. Lett.* **106,** 227401 (2011).

45.   Wang, J., Gong, M., Guo, G. C. & He, L. Eliminating the fine structure splitting of excitons in self-assembled InAs/GaAs quantum dots via combined stresses. *Appl. Phys. Lett.* **101,** 063114 (2012).

46.   Plumhof, J. D. *et al.* Strain-induced anticrossing of bright exciton levels in single self-assembled GaAs/AlxGa1-xAs and InxGa 1-xAs/GaAs quantum dots. *Phys. Rev. B - Condens. Matter Mater. Phys.* **83,** 121302(R) (2011).

47.   Trotta, R. *et al.* Universal recovery of the energy-level degeneracy of bright excitons in ingaas quantum dots without a structure symmetry. *Phys. Rev. Lett.* **109,** 147401 (2012).

48.   Trotta, R., Martín-Sánchez, J., Daruka, I., Ortix, C. & Rastelli, A. Energy-Tunable Sources of Entangled Photons: A Viable Concept for Solid-State-Based Quantum Relays. *Phys. Rev. Lett.* **114,** 150502 (2015).

49.   Wang, J., Gong, M., Guo, G.-C. & He, L. Towards Scalable Entangled Photon Sources with Self-Assembled InAs/GaAs Quantum Dots. *Phys. Rev. Lett.* **115,** 067401 (2015).

50.   Trotta, R. *et al.* Wavelength-tunable sources of entangled photons interfaced with atomic vapours. *Nat. Commun.* **7,** 10375 (2016).

51.   Chen, Y. *et al.* Wavelength-tunable entangled photons from silicon-integrated III–V quantum dots. *Nat. Commun.* **7,** 10387 (2016).

52.   Li, J., Shan, Z. & Ma, E. Elastic strain engineering for unprecedented materials properties. *MRS Bull.* **39,** 108–114 (2014).

53.   Yoffe, A. D. Low-dimensional systems: quantum size effects and electronic properties of semiconductor microcrystallites (zero-dimensional systems) and some quasi-two-dimensional systems. *Adv. Phys.* **42,** 173–262 (1993).

54.   Davies, J. H. The Physics of Low-Dimensional Semiconductors. (Cambridge University Press, 1997).

55.   Williamson, A. J., Wang, L. W. & Zunger, A. Theoretical interpretation of the experimental electronic structure of lens-shaped self-assembled InAs/GaAs quantum dots. *Phys. Rev. B - Condens. Matter Mater. Phys.* **62,** 12963–12977 (2000).

56.   Muller, A. *et al.* Resonance fluorescence from a coherently driven semiconductor quantum dot in a cavity. *Phys. Rev. Lett.* **99,** 187402 (2007).

57.   Xu, X. *et al.* Coherent optical spectroscopy of a strongly driven quantum dot. *Science.* **317,** 929–932 (2007).

58.   Somaschi, N. *et al.* Near-optimal single-photon sources in the solid state. *Nat. Photonics* **10,** 340–345 (2016).

59.   Müller, M., Bounouar, S., Jöns, K. D., Glässl, M. & Michler, P. On-demand generation of indistinguishable polarization-entangled photon pairs. *Nat. Photonics* **8,** 224–228 (2014).

60.   Hanschke, L. *et al.* Quantum dot single photon sources with ultra-low multi-photon probability. *Arxiv* **1801.01672,** 1–6 (2018).

61.   Moreau, E. *et al.* Quantum Cascade of Photons in Semiconductor Quantum Dots. *Phys. Rev.*

Lett. **87,** 183601 (2001).

62. Bester, G., Nair, S. & Zunger, A. Pseudopotential calculation of the excitonic fine structure of million-atom self-assembled In1-xGaxAs/GaAs quantum dots. *Phys. Rev. B - Condens. Matter Mater. Phys.* **67,** 161306(R) (2003).

63. Plumhof, J. D., Trotta, R., Rastelli, A. & Schmidt, O. G. Experimental methods of post-growth tuning of the excitonic fine structure splitting in semiconductor quantum dots. *Nanoscale Res. Lett.* **7,** 336 (2012).

64. Luo, J. W. & Zunger, A. Geometry of epitaxial GaAs/(Al,Ga)As quantum dots as seen by excitonic spectroscopy. *Phys. Rev. B - Condens. Matter Mater. Phys.* **84,** 235317 (2011).

65. Muller, A., Fang, W., Lawall, J. & Solomon, G. S. Creating polarization-entangled photon pairs from a semiconductor quantum dot using the optical stark effect. *Phys. Rev. Lett.* **103,** 217402 (2009).

66. Bayer, M. *et al.* Fine structure of neutral and charged excitons in self-assembled In(Ga)As/(Al)GaAs quantum dots. *Phys. Rev. B - Condens. Matter Mater. Phys.* **65,** 195315 (2002).

67. Wang, Z. M., Liang, B. L., Sablon, K. A. & Salamo, G. J. Nanoholes fabricated by self-assembled gallium nanodrill on GaAs(100). *Appl. Phys. Lett.* **90,** 113120 (2007).

68. Atkinson, P., Zallo, E. & Schmidt, O. G. Independent wavelength and density control of uniform GaAs/AlGaAs quantum dots grown by infilling self-assembled nanoholes. *J. Appl. Phys.* **112,** 054303 (2012).

69. Graf, A. *et al.* Excitonic states in GaAs quantum dots fabricated by local droplet etching. *Phys. Rev. B - Condens. Matter Mater. Phys.* **89,** 115314 (2014).

70. Huber, D. *et al.* Highly indistinguishable and strongly entangled photons from symmetric GaAs quantum dots. *Nat. Commun.* **8,** 15506 (2017).

71. Keil, R. *et al.* Solid-state ensemble of highly entangled photon sources at rubidium atomic transitions. *Nat. Commun.* **8,** 15501 (2017).

72. Sun, Y. *et al.* Physics of strain effects in semiconductors and metal-oxide-semiconductor field-effect transistors. *J. Appl. Phys.* **101,** 104503 (2008).

73. Chuang, S. L. *Physics of Optoelectronic Devices*. (Wiley, 1995).

74. https://en.wikipedia.org/wiki/Gallium_arsenide.

75. Sun, Y., Thompson, S. E. & Nishida, T. *Strain effect in semiconductors: Theory and device applications*. (Springer Science & Business Media, 2010).

76. Rayleigh, Lord. On waves propagated along the plane surface of an elastic solid. *Proc. London Math. Soc.* **s1-17,** 4–11 (1885).

77. Barnes, C. H. W., Shilton, J. M. & Robinson, A. M. Quantum computation using electrons trapped by surface acoustic waves. *Phys. Rev. B - Condens. Matter Mater. Phys.* **62,** 8410 (2000).

78. Shi, X., Zhang, M. & Wei, L. F. Quantum computation with moving quantum dots generated by surface acoustic waves. *Phys. Rev. A - At. Mol. Opt. Phys.* **84,** 062310 (2011).

79. Bertrand, B. *et al.* Injection of a single electron from static to moving quantum dots. *Nanotechnology* **27,** 214001 (2016).

80. Fuhrmann, D. A. High Frequency Dynamic Tuning of Photonic Crystal Nanocavities by Means of Acoustic Phonons (PhD thesis). (Universität Augsburg, 2014).

81. Schülein, F. J. R. Dynamische Kontrolle optisch aktiver Halbleiter-Quantenpunkte mittels

akustischer Oberflächenwellen (PhD thesis). (Universität Augsburg, 2014).

82. White, R. M. Surface Elastic Waves. *Proc. IEEE* **58,** 1238–1276 (1970).

83. Achenbach, J. D. *Wave propagation in elastic solids. Applied mathematics and Mechanics* **16,** (Elsevier Science Publishing Co Inc, 1973).

84. Campbell, J. J. & Jones, W. R. Propagation of piezoelectric surface waves on cubic and hexagonal crystals. *J. Appl. Phys.* **41,** 2796–2801 (1970).

85. White, R. M. & Voltmer, F. W. Direct piezoelectric coupling to surface elastic waves. *Appl. Phys. Lett.* **7,** 314–316 (1965).

86. Royer, D. & Dieulesaint, E. *Elastic waves in solids. Springer* (2000).

87. Zinoviy Nazarchuk，Valentyn Skalskyi，Oleh Serhiyenko. *Acoustic Emission: Methodology and Application*. (Springer International Publishing, 2017).

88. Lamb, H. On Waves in an Elastic Plate. *Proc. R. Soc. A Math. Phys. Eng. Sci.* **93,** 114–128 (1917).

89. Worden, K. Rayleigh and Lamb waves - Basic principles. *Strain* **37,** 167–172 (2001).

90. Su, Z. & Ye, L. Fundamentals and Analysis of Lamb Waves. *Lect. Notes Appl. Comput. Mech.* **48,** 15–58 (2009).

91. Rose, J. L. & Nagy, P. B. Ultrasonic Waves in Solid Media. *J. Acoust. Soc. Am.* **107,** 1807 (2000).

92. https://en.wikipedia.org/wiki/Lamb_waves.

93. Bouwes Bavinck, M. *et al.* Controlling a nanowire quantum dot band gap using a straining dielectric envelope. *Nano Lett.* **12,** 6206–6211 (2012).

94. Stepanov, P. *et al.* Large and Uniform Optical Emission Shifts in Quantum Dots Strained along Their Growth Axis. *Nano Lett.* **16,** 3215–3220 (2016).

95. Bryant, G. W. *et al.* Effect of mechanical strain on the optical properties of quantum dots: Controlling exciton shape, orientation, and phase with a mechanical strain. *Phys. Rev. Lett.* **105,** 067404 (2010).

96. Tumanov, D. *et al.* Static strain tuning of quantum dots embedded in a photonic wire. *Appl. Phys. Lett.* **112,** 123102 (2018).

97. Park, S. E. & Shrout, T. R. Ultrahigh strain and piezoelectric behavior in relaxor based ferroelectric single crystals. *J. Appl. Phys.* **82,** 1804–1811 (1997).

98. Biegalski, M. D., Dörr, K., Kim, D. H. & Christen, H. M. Applying uniform reversible strain to epitaxial oxide films. *Appl. Phys. Lett.* **96,** 151905 (2010).

99. Chen, Y. *et al.* Temperature-Dependent Coercive Field Measured by a Quantum Dot Strain Gauge. *Nano Lett.* **17,** 7864–7868 (2017).

100. Herklotz, A. *et al.* Electrical characterization of PMN-28%PT(001) crystals used as thin-film substrates. *J. Appl. Phys.* **108,** 094101 (2010).

101. Ziss, D. *et al.* Comparison of different bonding techniques for efficient strain transfer using piezoelectric actuators. *J. Appl. Phys.* **121,** 135303 (2017).

102. Avron, J. E. *et al.* Entanglement on demand through time reordering. *Phys. Rev. Lett.* **100,** 120501 (2008).

103. Martín-Sánchez, J. *et al.* Strain-tuning of the optical properties of semiconductor nanomaterials by integration onto piezoelectric actuators. *Semiconductor Science and Technology* **33,** 013001 (2018).

104. Trotta, R. *et al.* Nanomembrane quantum-light-emitting diodes integrated onto piezoelectric

actuators. *Adv. Mater.* **24,** 2668–2672 (2012).

105. Singh, R. & Bester, G. Lower bound for the excitonic fine structure splitting in self-assembled quantum dots. *Phys. Rev. Lett.* **104,** 196803 (2010).

106. Plumhof, J. D. *et al.* Strain-induced anticrossing of bright exciton levels in single self-assembled GaAs/AlxGa1−xAs and InxGa1−xAs/GaAs quantum dots. *Phys. Rev. B - Condens. Matter Mater. Phys.* **83,** 121302(R) (2011).

107. Trotta, R., Wildmann, J. S., Zallo, E., Schmidt, O. G. & Rastelli, A. Highly entangled photons from hybrid piezoelectric-semiconductor quantum dot devices. *Nano Lett.* **14,** 3439–3444 (2014).

108. Zhang, J. *et al.* High yield and ultrafast sources of electrically triggered entangled-photon pairs based on strain-tunable quantum dots. *Nat. Commun.* **6,** 10067 (2015).

109. Huang, H. *et al.* Electrically-Pumped Wavelength-Tunable GaAs Quantum Dots Interfaced with Rubidium Atoms. *ACS Photonics* **4,** 868–872 (2017).

110. Martín-Sánchez, J. *et al.* Reversible Control of In-Plane Elastic Stress Tensor in Nanomembranes. *Adv. Opt. Mater.* **4,** 682–687 (2016).

111. Wagesreither, S., Bertagnolli, E., Kawase, S., Isono, Y. & Lugstein, A. Electrostatic actuated strain engineering in monolithically integrated VLS grown silicon nanowires. *Nanotechnology* **25,** 455705 (2014).

112. Signorello, G., Karg, S., Bjo, M. T., Gotsmann, B. & Riel, H. Tuning the Light Emission from GaAs Nanowires over 290 meV with Uniaxial Strain. *Nano Lett.* **13,** 917–924 (2013).

113. Wu, W. *et al.* Piezoelectricity of single-atomic-layer MoS2 for energy conversion and piezotronics. *Nature* **514,** 470–474 (2014).

114. Mori, Y. & Watanabe, N. A New Etching Solution System, H3PO4,-H2O2 -H2O, for GaAs and Its Kinetics. *J. Electrochem. Soc* **125,** 1510–1514 (1978).

115. McNeil, R. P. G. *et al.* On-demand single-electron transfer between distant quantum dots. *Nature* **477,** 439–442 (2011).

116. Metcalfe, M., Carr, S. M., Muller, A., Solomon, G. S. & Lawall, J. Resolved sideband emission of InAs/GaAs quantum dots strained by surface acoustic waves. *Phys. Rev. Lett.* **105,** 037401 (2010).

117. Völk, S. *et al.* Surface acoustic wave mediated carrier injection into individual quantum post nano emitters. *Nanotechnology* **23,** 285201 (2012).

118. Völk, S. *et al.* Enhanced sequential carrier capture into individual quantum dots and quantum posts controlled by surface acoustic waves. *Nano Lett.* **10,** 3399–3407 (2010).

119. Schülein, F. J. R. *et al.* Fourier synthesis of radiofrequency nanomechanical pulses with different shapes. *Nat. Nanotechnol.* **10,** 1–8 (2015).

120. Schuetz, M. J. A. *et al.* Universal quantum transducers based on surface acoustic waves. *Phys. Rev. X.* **5,** 031031 (2015).

121. Wilson-Rae, I. Nanomechanics: Rocking at the nanoscale. *Nat. Nanotechnol.* **10,** 489–490 (2015).

122. COMSOL. Introduction to COMSOL Multiphysics 5.3. *Manual* 168 (2017).

123. Michler, P. *Quantum Dots for Quantum Information Technologies*. (Springer International Publishing, 2017).

124. Lodahl, P., Mahmoodian, S. & Stobbe, S. Interfacing single photons and single quantum dots with photonic nanostructures. *Reviews of Modern Physics* **87,** 347–400 (2015).

125. Warburton, R. J. Single spins in self-assembled quantum dots. *Nat. Mater.* **12,** 483–493 (2013).

126. Claudon, J. *et al.* A highly efficient single-photon source based on a quantum dot in a photonic nanowire. *Nat. Photonics* **4,** 174–177 (2010).

127. Shields, A. J. Semiconductor quantum light sources. *Nat. Photonics* **1,** 215–223 (2007).

128. Gschrey, M. *et al.* Highly indistinguishable photons from deterministic quantum-dot microlenses utilizing three-dimensional in situ electron-beam lithography. *Nat. Commun.* **6,** 7662 (2015).

129. Santori, C., Fattal, D., Vucković, J., Solomon, G. S. & Yamamoto, Y. Indistinguishable photons from a single-photon device. *Nature* **419,** 594–597 (2002).

130. Esmaeilzadeh, I. *et al.* Deterministic integration of single photon sources in silicon based photonic circuits. *Nano Lett.* **16,** 2289–2294 (2016).

131. Heyn, C. *et al.* Highly uniform and strain-free GaAs quantum dots fabricated by filling of self-assembled nanoholes. *Appl. Phys. Lett.* **94,** 183113 (2009).

132. Tonin, C. *et al.* Polarization properties of excitonic qubits in single self-assembled quantum dots. *Phys. Rev. B - Condens. Matter Mater. Phys.* **85,** 155303 (2012).

133. Plumhof, J. D. *et al.* Tuning of the valence band mixing of excitons confined in GaAs/AlGaAs quantum dots via piezoelectric-induced anisotropic strain. *Phys. Rev. B - Condens. Matter Mater. Phys.* **87,** 075311 (2013).

134. Süess, M. J. *et al.* Analysis of enhanced light emission from highly strained germanium microbridges. *Nat. Photonics* **7,** 466–472 (2013).

135. Keplinger, M. *et al.* Strain distribution in single, suspended germanium nanowires studied using nanofocused x-rays. *Nanotechnology* **27,** 055705 (2016).

136. Trotta, R. & Rastelli, A. in *Engineering the Atom-Photon Interaction: Controlling Fundamental Processes with Photons, Atoms and Solids* (eds. Predojević, A. & Mitchell, M. W.) 405 (Springer, 2015).

137. Cottam, R. I. & Saunders, G. a. The elastic constants of GaAs from 2 K to 320 K. *J. Phys. C Solid State Phys.* **6,** 2105–2118 (2001).

138. Akopian, N., Wang, L., Rastelli, A., Schmidt, O. G. & Zwiller, V. Hybrid semiconductor-atomic interface: slowing down single photons from a quantum dot. *Nat. Photonics* **5,** 230–233 (2011).

139. Specht, H. P. *et al.* A single-atom quantum memory. *Nature* **473,** 190–193 (2011).

140. Briegel, H. J., Dür, W., Cirac, J. I. & Zoller, P. Quantum repeaters: The role of imperfect local operations in quantum communication. *Phys. Rev. Lett.* **81,** 5932–5935 (1998).

141. Kumar, S. *et al.* Strain-induced tuning of the emission wavelength of high quality GaAs/AlGaAs quantum dots in the spectral range of the 87Rb D2 lines. *Appl. Phys. Lett.* **99,** 161118 (2011).

142. Shimizu, F. Laser cooling and trapping of neutral atoms. *Hyperfine Interact.* **74,** 259–267 (1992).

143. Siddons, P., Adams, C. S., Ge, C. & Hughes, I. G. Absolute absorption on the rubidium D lines: comparison between theory and experiment. *J. Phys. B At. Mol. Opt. Phys.* **41,** 155004 (2008).

144. Wolters, J. *et al.* Simple Atomic Quantum Memory Suitable for Semiconductor Quantum Dot Single Photons. *Phys. Rev. Lett.* **119,** 060502 (2017).

145. Huo, Y. H. *et al.* A light-hole exciton in a quantum dot. *Nat. Phys.* **10,** 46–51 (2014).

146. Makhonin, M. N. *et al.* Waveguide coupled resonance fluorescence from on-chip quantum emitter. *Nano Lett.* **14,** 6997–7002 (2014).

147. Seidl, S. *et al.* Statistics of quantum dot exciton fine structure splittings and their polarization orientations. *Phys. E Low-dimensional Syst. Nanostructures* **40,** 2153–2155 (2008).

148. Chuang, S. L. *Physics of photonic devices*. (John Wiley & Sons, 2009).

149. Vurgaftman, I., Meyer, J. R. & Ram-Mohan, L. R. Band parameters for III–V compound semiconductors and their alloys. *J. Appl. Phys.* **89,** 5815–5875 (2001).

150. Dietrich, C. P., Fiore, A., Thompson, M. G., Kamp, M. & Höfling, S. GaAs integrated quantum photonics: Towards compact and multi-functional quantum photonic integrated circuits. *Laser Photon. Rev.* **10,** 870–894 (2016).

151. Kaganskiy, A. *et al.* Advanced in-situ electron-beam lithography for deterministic nanophotonic device processing. *Rev. Sci. Instrum.* **86,** 073903 (2015).

152. Liu, J. *et al.* Cryogenic photoluminescence imaging system for nanoscale positioning of single quantum emitters. *Rev. Sci. Instrum.* **88,** 023116 (2017).

153. Grange, T. *et al.* Reducing Phonon-Induced Decoherence in Solid-State Single-Photon Sources with Cavity Quantum Electrodynamics. *Phys. Rev. Lett.* **118,** 253602 (2017).

154. Iles-Smith, J., McCutcheon, D. P. S., Nazir, A. & Mørk, J. Phonon scattering inhibits simultaneous near-unity efficiency and indistinguishability in semiconductor single-photon sources. *Nat. Photonics* **11,** 521–526 (2017).

155. Treutlein, P., Genes, C., Hammerer, K., Poggio, M. & Rabl, P. in *Cavity Optomechanics, Quantum Science and Technology* 327–351 (Springer Berlin Heidelberg, 2014).

156. Macquarrie, E. R., Gosavi, T. A., Jungwirth, N. R., Bhave, S. A. & Fuchs, G. D. Mechanical spin control of nitrogen-vacancy centers in diamond. *Phys. Rev. Lett.* **111,** 227602 (2013).

157. Ruskov, R., Schwab, K. & Korotkov, A. N. Squeezing of a nanomechanical resonator by quantum nondemolition measurement and feedback. *Phys. Rev. B - Condens. Matter Mater. Phys.* **71,** 235407 (2005).

158. McGee, S. A., Meiser, D., Regal, C. A., Lehnert, K. W. & Holland, M. J. Mechanical resonators for storage and transfer of electrical and optical quantum states. *Phys. Rev. A - At. Mol. Opt. Phys.* **87,** 053818 (2013).

159. Vostrosablin, N., Rakhubovsky, A. A. & Filip, R. Pulsed quantum interaction between two distant mechanical oscillators. *Phys. Rev. A - At. Mol. Opt. Phys.* **94,** 063801 (2016).

160. Yeo, I. *et al.* Strain-mediated coupling in a quantum dot-mechanical oscillator hybrid system. *Nat. Nanotechnol.* **9,** 106–110 (2013).

161. Montinaro, M. *et al.* Quantum dot opto-mechanics in a fully self-assembled nanowire. *Nano Lett.* **14,** 4454–4460 (2014).

162. Carter, S. G. *et al.* Spin-Mechanical Coupling of an InAs Quantum Dot Embedded in a Mechanical Resonator. *Phys. Rev. Lett.* **121,** 246801 (2018).

163. Kato, Y. *et al.* Gigahertz electron spin manipulation using voltage-controlled g-tensor modulation. *Science.* **299,** 1201–1204 (2003).

164. Houel, J. *et al.* High resolution coherent population trapping on a single hole spin in a semiconductor quantum dot. *Phys. Rev. Lett.* **112,** 107401 (2014).

165. William Weaver, J., Timosbenko, S. P. & Young, D. H. *Vibration Problems in Engineering*. (John Wiley & Sons, 1990).

166. Cleland, A. N. & Krim, J. *Foundations of Nanomechanics: From Solid-State Theory to Device*

Applications. (Springer-Verlag Berlin Heidelberg, 2004).

167. Han, S. M., Benaroya, H. & Wei, T. Dynamics of transversely vibrating beams using four engineering theories. *J. Sound Vib.* **225,** 935–988 (1999).

168. Bokaian, A. Natural frequencies of beams under tensile axial loads. *J. Sound Vib.* **142,** 481–498 (1990).

169. Nysten, E. D. S. *et al.* Multi-harmonic quantum dot optomechanics in fused LiNbO3-(Al)GaAs hybrids. *J. Phys. D. Appl. Phys.* **50,** 43LT01 (2017).

170. Weiß, M. & Krenner, H. J. Interfacing quantum emitters with propagating surface acoustic waves. *J. Phys. D. Appl. Phys.* **51,** 373001 (2018).

171. Braakman, F. R. *et al.* Nonlinear motion and mechanical mixing in as-grown GaAs nanowires. *Appl. Phys. Lett.* **105,** 173111 (2014).

172. Malla, R. K. & Raikh, M. E. Landau-Zener transition in a two-level system coupled to a single highly excited oscillator. *Phys. Rev. B - Condens. Matter Mater. Phys.* **97,** 035428 (2018).

173. Blattmann, R., Krenner, H. J., Kohler, S. & Hänggi, P. Entanglement creation in a quantum-dot-nanocavity system by Fourier-synthesized acoustic pulses. *Phys. Rev. A - At. Mol. Opt. Phys.* **89,** 012327 (2014).

174. Gell, J. R. *et al.* Modulation of single quantum dot energy levels by a surface-acoustic-wave. *Appl. Phys. Lett.* **93,** 081115 (2008).

175. Liu, J. *et al.* High-Q optomechanical GaAs nanomembranes. *Appl. Phys. Lett.* **99,** 243102 (2011).

176. Verhagen, E., Deléglise, S., Weis, S., Schliesser, A. & Kippenberg, T. J. Quantum-coherent coupling of a mechanical oscillator to an optical cavity mode. *Nature* **482,** 63–67 (2012).

177. Ovartchaiyapong, P., Lee, K. W., Myers, B. A. & Jayich, A. C. B. Dynamic strain-mediated coupling of a single diamond spin to a mechanical resonator. *Nat. Commun.* **5,** 4429 (2014).

178. De Bell, L. T. & Li, R. C. M. Surface-Acoustic-Wave Resonators. *Proc. IEEE* **64,** 711–721 (1976).

179. Thoma, A. *et al.* Exploring Dephasing of a Solid-State Quantum Emitter via Time- and Temperature-Dependent Hong-Ou-Mandel Experiments. *Phys. Rev. Lett.* **116,** 033601 (2016).

180. Iles-Smith, J., McCutcheon, D. P. S., Mørk, J. & Nazir, A. Limits to coherent scattering and photon coalescence from solid-state quantum emitters. *Phys. Rev. B - Condens. Matter Mater. Phys.* **95,** 201305(R) (2017).

181. Houel, J. *et al.* Probing single-charge fluctuations at a GaAs/AlAs interface using laser spectroscopy on a nearby InGaAs quantum dot. *Phys. Rev. Lett.* **108,** 107401 (2012).

182. Kuhlmann, A. V. *et al.* Charge noise and spin noise in a semiconductor quantum device. *Nat. Phys.* **9,** 570–575 (2013).

183. Ramsay, A. J. *et al.* Damping of exciton rabi rotations by acoustic phonons in optically excited InGaAs/GaAs quantum dots. *Phys. Rev. Lett.* **104,** 017402 (2010).

184. Reigue, A. *et al.* Probing Electron-Phonon Interaction through Two-Photon Interference in Resonantly Driven Semiconductor Quantum Dots. *Phys. Rev. Lett.* **118,** 233602 (2017).

185. Weiß, M. *et al.* Multiharmonic Frequency-Chirped Transducers for Surface-Acoustic-Wave Optomechanics. *Phys. Rev. Appl.* **9,** 014004 (2018).

186. Heigl, M. B. Das Verhalten akustischer Oberflächenwellen in Halbleitermembranen (Master thesis). (Universität Augsburg, 2016).

187. Vogele, A. Quantenpunkt-Optomechanik in nanophononischen Schaltkreisen (Master Thesis).

(Universität Augsburg, 2019).

188. Brendel, C., Peano, V., Painter, O. & Marquardt, F. Snowflake phononic topological insulator at the nanoscale. *Phys. Rev. B - Condens. Matter Mater. Phys.* **97,** 020102(R) (2018).

189. Kapfinger, S. *et al.* Dynamic acousto-optic control of a strongly coupled photonic molecule. *Nat. Commun.* **6,** 8540 (2015).

190. Pooley, M. A. *et al.* Controlled-NOT gate operating with single photons. *Appl. Phys. Lett.* **100,** 211103 (2012).

191. Gurudev Dutt, M. V. *et al.* Ultrafast optical control of electron spin coherence in charged GaAs quantum dots. *Phys. Rev. B - Condens. Matter Mater. Phys.* **74,** 125306 (2006).

192. Béguin, L. *et al.* On-demand semiconductor source of 780-nm single photons with controlled temporal wave packets. *Phys. Rev. B - Condens. Matter Mater. Phys.* **97,** 205304 (2018).

193. Schöll, E. *et al.* Resonance fluorescence of GaAs quantum dots with near-unity photon indistinguishability. *Arxiv* **1901.09721,** 1–17 (2019).

194. Arlt, G. & Quadflieg, P. Piezoelectricity in iii-v compounds with a phenomenological analysis of the piezoelectric effect. *Phys. Status Solidi* **25,** 323–330 (1968).

195. Wen, G. W., Lin, J. Y., Jiang, H. X. & Chen, Z. Quantum-confined Stark effects in semiconductor quantum dots. *Phys. Rev. B - Condens. Matter Mater. Phys.* **52,** 5913–5922 (1995).

196. Miller, D. A. B. *et al.* Band-edge electroabsorption in quantum well structures: The quantum-confined stark effect. *Phys. Rev. Lett.* **53,** 2173 (1984).

197. Oulton, R. *et al.* Manipulation of the homogeneous linewidth of an individual in(Ga)As quantum dot. *Phys. Rev. B - Condens. Matter Mater. Phys.* **66,** 045313 (2002).

198. Bennett, A. J. *et al.* Giant Stark effect in the emission of single semiconductor quantum dots. *Appl. Phys. Lett.* **97,** 031104 (2010).

Acknowledgment

Now it is time to draw an end to my PhD study, an amazing period which seems not very smooth but really fruitful. Even now I can think back the day when I took the flight to Europe to pursue my PhD degree, felt confident but a little uneasy about the future, now I nearly managed it!

Special words of thanks go to my supervisor in Augsburg, Prof. Dr. Hubert J. Krenner. I acknowledge the opportunity that he can accept me as a PhD student at the Lehrstuhl für Experimentalphysik I, University Augsburg. It is really a rare opportunity that I can enter this amazing field to play with the SAWs, which broadened my horizons. Most importantly, his work style and attitude to research make me clear why Germany can always take an advanced position in science. I hope I can learn from the spirit and eventually take it when I go back to China. Lastly, his enthusiasm towards science also inspires me a lot.

I would express my deep gratitude to my supervisor in Linz, Prof. Dr. Armando Rastelli. It is my honor that I can enter his group and under the supervision of him during my PhD period. During the past four years in Linz, Armando not only plays a role being my supervisor academically but more to inspire all of us to behave as a real researcher with his personal charm. Thanks Armando to introduce me to the field of "quantum dots", I appreciate so much for his excellent ideas and support during my PhD study.

I would like to thank Prof. Dr. Manfred Albrecht, who accept being the "Zweitgutachter" of this thesis. Thank you very much for taking time to review my thesis and give valuable comments and advices.

The financial support from China Scholar Council (CSC, No 201306090010) is gratefully acknowledged. Without the CSC scholarship, definitely it will be more difficult for me to go abroad to choose such an interesting topic for my PhD study. I will also give my thanks to the responsible people in the embassy of China in Berlin and Chinese consulate in München for the continuous support.

Thanks need to go to Dr. Yongheng Huo (now a full professor at University of Science and Technology of China). It is him who introduced me to the field of semiconductor quantum dots, and at the beginning of my PhD study, so much effort he spent to teach me the MBE growth and optical characterization. Most importantly, I am deeply grateful that he introduced me to Armando's group, which may be the best decision during the past five years. Lastly, his philosophy of life is also so helpful to me, although part of them is still arcane to me.

I am grateful to Dr. Javier Martín-Sánchez (now at University of Oviedo, Spain) for his contributions and help. When I arrived in Linz, he gave me all the introductions and training on the sample process. I am so appreciated his attitude to transfer his knowledge unreservedly. Even now, I still miss the time when we stayed in the cleanroom to improve the processing.

I would like to also express my gratitude to Dr. Rinaldo Trotta (now professor at

Sapienza University of Rome, Italy). Not only some excellent ideas on QDs but also I am inspired by his attitude and sensitive grasp to the scientific topics.

Acknowledgement should go to our theoretical collaborators, Prof. Dr. Gabriel Bester, Fritz Weyhausen-Brinkmann (Universität Hamburg), Dr. Vlastimil Křápek (Brno University of Technology) and Dr. Petr Klenovsky (Masaryk University). Their contributions make the experimental observations and physics more clear.

Next I am so thankful to the members in our group in Linz. Thanks to our grower: Dr. Saimon Filipe Covre da Silva. He can always discuss and help with the scientific issues. Moreover, excellent samples can be always provided from him in a short time. My Chinese colleagues, Huiying Huang and Santanu Manna, also helped me a lot. Then I would also thank the "two-photon brothers" (Marcus Reindl and Daniel Huber) and Christian Schimpf for help and convey their optical experience to me.

Of course thanks should also go to other colleagues in the Institute of Semiconductor and Solid state physics. I can not figure out how many times our secretary Susanne Schwind helped me during my stay in Linz. She is so friendly, enthusiastic and efficient. Then I should thank our cleanroom team members, they are Alma Halilovic, Ursula Kainz, Albin Schwarz, Stephan Bräuer, Ernst Vorhauer and Friedrich Binder. It's their hard work make my research efficient and smooth.

The stay in Augsburg is one of the best exciting experience during my PhD study, special thanks go to the colleagues there, they are Matthias Weiß, Maximilian Sonner, Anja Vogele, Emeline Nysten, Sebastian Hammer, Lisa Janker and Tobias Petzak. Especially Matthias Weiß and Maximilian Sonner, who not only contribute to the whole the processing but also always be patient to explain and teach me the related knowledge. Many thanks go to Anja Vogele for her contributions and helping with the SAWs modulation experiments at Augsburg. It is a great time that we can sit together to chat, and I am so happy to learn the attractive German culture. It is my fortune that I can have the chance to work in the lab in Augsburg, some other members in Lehrstuhl für Experimentalphysik I, University Augsburg are acknowledged.

The one and half years stay in Dresden is also precious experience for me, I will express my thanks to Prof. Dr. Oliver G. Schmidt, Dr. Fei Ding (now a full professor in Universität Hannover), Yan Chen and Yin Yin. Thanks for all the support and help.

Last but not least, the special acknowledgment should give to my parents (Mr. Jie Yuan and Mrs. Cuifang Hu) in China. I need to cherish their love and repay their upbring: For the past years, they always supported my decision. During the time of my PhD study, they are always happy to hear all my experience in Europe. They drive me to work hard and with passion, and I hope this thesis would be a nice dedication to them.

Curriculum vitae

Personal Information:

Name	Yuan, Xueyong (袁学勇)
Date of birth	01 May, 1989
Place of birth	Yancheng, Jiangsu, China
Nationality	Chinese

Education

Universität Augsburg, Augsburg, Germany　　　　　**May. 2017 – present**

Ph. D. candidate, Lehrstuhl für Experimentalphysik I

Supervisor: Prof. Dr. Hubert J. Krenner

Johannes Kepler University, Linz, Austria　　　　　**Mar. 2015 – present**

Ph. D. candidate, Institute of Semiconductor and Solid State Physics

Supervisor: Prof. Dr. Armando Rastelli

IFW, Dresden, Germany　　　　　**Oct. 2013 – Mar. 2015**

Ph. D. candidate, Institute of Integrative Nanosciences

Supervisor: Prof. Dr. Oliver G. Schmidt

Southeast University, Nanjing, China　　　　　**Oct. 2010 – Jun. 2013**

M. Sc degree, Physics Department

Thesis: Preparation and Magnetoelectric Effect of Multiferroic $BiFeO_3$ Thin Films

Supervisor: Prof. Dr. Qingyu Xu

Southeast University, Nanjing, China　　　　　**Oct. 2006 – Jun. 2010**

B. Sc degree, Optical Information Science and Technology, Physics Department